

Experimental measurement and a physical interpretation of quantum shadow enumerators

Daniel Miller,^{1,2,*} Kyano Levi,¹ Lukas Postler,³ Alex Steiner,³ Lennart Bittel,¹ Gregory A. L. White,¹ Yifan Tang,¹ Eric J. Kuehnke,¹ Antonio A. Mele,¹ Sumeet Khatri,^{1,4,5} Lorenzo Leone,¹ Jose Carrasco,¹ Christian D. Marciniak,³ Ivan Pogorelov,³ Milena Guevara-Bertsch,³ Robert Freund,³ Rainer Blatt,^{3,6} Philipp Schindler,³ Thomas Monz,^{3,7} Martin Ringbauer,³ and Jens Eisert¹

¹*Dahlem Center for Complex Quantum Systems, Freie Universität Berlin, 14195 Berlin, Germany*

²*Institute for Theoretical Nanoelectronics (PGI-2), Forschungszentrum Jülich, 52428 Jülich, Germany*

³*Universität Innsbruck, Institut für Experimentalphysik, Technikerstrasse 25, 6020 Innsbruck, Austria*

⁴*Department of Computer Science, Virginia Tech, Blacksburg, Virginia 24061, USA*

⁵*Virginia Tech Center for Quantum Information Science and Engineering, Blacksburg, Virginia 24061, USA*

⁶*Institut für Quantenoptik und Quanteninformation, Österreichische Akademie der Wissenschaften, Otto-Hittmair-Platz 1, 6020 Innsbruck, Austria*

⁷*Alpine Quantum Technologies GmbH, 6020 Innsbruck, Austria*

Throughout its history, the theory of quantum error correction has heavily benefited from translating classical concepts into the quantum setting. In particular, classical notions of weight enumerators, which relate to the performance of an error-correcting code, and MacWilliams’ identity, which helps to compute enumerators, have been generalized to the quantum case. In this work, we establish a distinct relationship between the theoretical machinery of quantum weight enumerators and a seemingly unrelated physics experiment: we prove that Rains’ quantum shadow enumerators—a powerful mathematical tool—arise as probabilities of observing fixed numbers of triplets in a Bell sampling experiment. This insight allows us to develop here a rigorous framework for the direct measurement of quantum weight enumerators, thus enabling experimental and theoretical studies of the entanglement structure of any quantum error-correcting code or state under investigation. On top of that, we derive concrete sample complexity bounds and physically-motivated robustness guarantees against unavoidable experimental imperfections. Finally, we experimentally demonstrate the feasibility of directly measuring weight enumerators on a trapped-ion quantum computer. Our experimental findings are in good agreement with theoretical predictions and illuminate how entanglement theory and quantum error correction cross-fertilize each other once Bell sampling experiments are combined with the theoretical machinery of quantum weight enumerators.

I. INTRODUCTION

The ultimate goal in quantum technology is to see high-fidelity quantum devices both actualized and justified. This will require us to solve two major challenges that—each individually—have received a great deal of attention. The first challenge (actualization) poses the question “*how can we protect fragile quantum information against noise?*” and indeed, the theory of *quantum error correction* (QEC) allows for the detection and correction of errors that arise over the course of a quantum computation [1–3]. Such ability is remarkable in light of the unavoidable backaction that parity check measurements inflict while hunting down errors. It is widely accepted that QEC will be essential to the realization of full-scale quantum computers, and so substantial efforts are being made to overcome the noise bottleneck. These efforts have led to remarkable recent progress on hardware development [4–11]. Of equal fundamental importance to the development of use cases for quantum computers and, thus, to the second challenge (justification) is the question “*how can we efficiently extract properties of a carefully constructed quantum state?*”. On the one hand, knowing what is efficiently measurable informs characterization and benchmarking techniques [12–15], such as measuring the ability to generate large-scale entanglement [16–19], a prerequisite for quantum advantage [20]. On

the other hand, and more provocatively, answers to this second question should also foster our understanding of genuine quantum phenomena, which could unlock entirely new applications. As quantum devices are moving closer and closer towards fault tolerance, the above questions are becoming increasingly pertinent. At the same time, these questions are seldom considered in tandem, leaving exciting opportunity to do so.

The relationship between each challenge is not obvious from the outset. Concepts from state characterization have found their way into QEC, but not often vice versa. For linear properties—such as fidelities and parity check violations—the issue of efficient measurements has been largely resolved in the context of classical shadows [21–25]. But not all quantities relevant for QEC are linear. In the regime beyond linear, leveraging parallel *multi-copy measurements* will become important [26–31]. The sample complexity of estimating nonlinear properties typically features an exponential separation between the two memory access models where multiple copies of a quantum state are measured either (i) individually or (ii) jointly in an entangled basis. Most prominently, *two-copy Bell sampling* enables efficient measurements of purities and squared Pauli expectation values [10] with wide-ranging applications in quantum machine learning [28, 32] and topological data analysis [33]. Which other quadratic properties can be efficiently learned via Bell sampling is subject of active research [34]. In the contexts of error correction and mitigation, simultaneous access to multiple copies is essential for benchmarking so-called resources of *magic* [34–38] and for *virtual*

* d.miller@fu-berlin.de

distillation [39–42]. Having said this, multi-copy measurements are challenging to implement and experiments have just reached the stage of Bell sampling [10, 11, 28, 43–45].

Ever since its first steps were taken [46–56], QEC has been deeply intertwined with concepts of classical error correction [57–61]. On the algebraic side, *quantum weight enumerators* (QWE) polynomials [51–54] have generalized corresponding classical notions carrying results such as the *MacWilliams identity* (see below) into the quantum setting. The trifecta of QWEs comprises *Shor-Laflamme* [51], *Rains’ unitary* [53], and *Rains’ shadow QWEs* [54], which can each be inter-converted using the so-called *Krawtchouk polynomials* [62]. The Shor-Laflamme QWE distribution (SLD) is best understood for stabilizer *quantum error-correcting codes* (QECCs), where it coincides with the Pauli weight distribution of the code’s stabilizer group [52]. Strikingly, the SLD can be converted—via MacWilliams’ transform—into what we call dual SLD, which is the weight distribution of the logical Pauli group. Hence, from the SLD, one can infer the code distance d , i.e., the smallest weight of a logical Pauli operator. From a complexity-theoretic point of view, this is interesting because the problem of computing the distance of a linear code is NP-hard [63]. In turn, computing SLDs is NP-hard as well [64]. Nevertheless, recent advances involving tensor network methods are pushing the boundaries of how SLDs can be computed in practice [64–66].

QWEs are also quite powerful from alternate perspectives. From the very beginning [51, 54], QWEs were leveraged to rule out the existence of QECCs with certain code parameters $[[n, k, d]]$, where n and k denote the numbers of physical and logical qubits, respectively. More recently, a set of criteria has been found from QWEs to bootstrap codes that correct errors from codes that merely detect them [67]. For modern efforts in designing *quantum low-density parity-check* (qLDPC) codes [68–72], Rains’ shadow enumerators can provide bounds on parameters of asymptotically good qLDPC code families, i.e., those for which the distance d scales like cn for a non-zero constant $c > 0$ [70, 71]. In this context, it is shown that the constant is bounded as $c \leq 1/3$ [54]. Despite these applications, however, the physical interpretation of Rains’ shadow enumerators—the topic of this work—has remained a mystery for almost three decades.

The physics behind Shor-Laflamme enumerators, on the other hand, is well understood. Originally introduced for the purpose of capturing the relationship between the entanglement fidelity and average fidelity of codewords sent through the local depolarizing channel [51], they have since then found numerous other interpretations. In the literature on the geometry of quantum states and entanglement, SLDs are often called correlation tensor norms [73–76], but they have also recently appeared under the name *sector length distribution* [77–79], which decomposes the purity $\text{Tr}[\rho^2]$ of an n -qubit state ρ into $n+1$ Pauli-weight sectors and conveniently shares its acronym with the term Shor-Laflamme distribution. Moreover, SLDs in disguise have been employed in the study of random quantum circuits [66, 80] and of quantum chaos [81]. But despite their physical connection to quantum entanglement, it is not clear under what circumstances SLDs can be measured efficiently.

Suspecting a two-copy protocol for SLDs is not far-fetched. A first clue is that SLDs decompose purities, which can be efficiently measured using two copies [27]. The same is true for all (exponentially many) squared Pauli expectation values, which enter the definition of SLDs [Eq. (10)]. In this work, we develop a method to circumvent the need of evaluating sums over exponentially many terms by establishing a direct connection between Rains’ quantum shadow enumerators and two-copy Bell sampling experiments. The latter give rise to notions of singlet and triplet probabilities, i.e., to the frequencies of measuring either the single antisymmetric or one of the three symmetric Bell states, respectively. Our main theoretical result (Thm. 3) is that these triplet probability distributions are the same as Rains’ quantum shadow enumerators. This discovery has several notable implications: (i) it provides a physical interpretation for the theoretical machinery of QWEs; (ii) it enables exponential speedups in classical post-processing compared to brute-force approaches for computing QWEs from Bell samples; and (iii) it identifies the conditions under which some enumerators can be efficiently estimated, while others cannot.

The core aim of this work is twofold: first, we provide a comprehensive and unified view of weight enumerators, thereby strengthening the connection between entanglement theory and quantum error correction. Second, we endow these key quantities with operational and empirical meaning. More precisely, we develop a rigorous framework for measuring QWEs that also takes into account many practical considerations. The methods developed are then demonstrated in the form of entanglement characterization experiments on a state-of-the-art sixteen-qubit trapped-ion quantum processor.

In a first two-copy Bell sampling experiment, we investigate a suite of six-qubit states and showcase how the QWE machinery can be leveraged to reveal detailed information about the multi-faceted entanglement structure that differentiates these states. Specifically, from the measured triplet probability distributions, we compute the *total i -body correlations* [Eq. (10)], *averaged purities* [Eq. (28)], and a lower bound on the *concurrence* [Ineq. (82)]. Of high practical value is that all of this is possible without expensive postprocessing or the need for updating readout circuits. In principle, triplet probabilities would further allow us to certify *m -uniform states* [Eq. (33)] and to measure the *n -tangle* [Eq. (85)], however, these applications face practical limitations that are also discussed here. Finally, to remove errors from the Bell samples, we propose and implement a heuristic error mitigation strategy that heavily relies on the QWE machinery.

In a second experiment, we directly measure the QWEs of the $[[7, 1, 3]]$ color code by performing transversal Bell measurements on two copies of the maximally mixed logical state. Our experiment simultaneously constitutes a Bell measurement on the logical level of this code. Therefore, we can detect and correct errors on the Bell samples. After discarding all outcomes with violated parity checks (ca. 57% of the data), we can correctly (within error bars) infer the number of weight- i stabilizers and logical Pauli operators for all $i \in \{0, \dots, 7\}$. This observation can be regarded as an experimental signature confirming that the probed QECC has distance $d = 3$.

Besides the rich information one gains about entanglement and QEC-related properties, our protocol has yet another useful application: when the QWEs of a target state are known in advance, directly measuring QWEs constitutes an extremely sample-efficient one-sided test—with the additional practical benefit of being single-setting—for bugfixing quantum circuits and spotting implementation errors early on. In this context, it is important to note that QWEs are local-unitary invariants [53], hence, incorrect QWEs cannot stem from incorrectly implemented single-qubit gates in the final layer of a preparation circuit. This informs where to look for mistakes.

Our work is organized as follows. In Sec. II, we introduce QWEs and discuss their relationship to the MacWilliams transform. This section aims to be pedagogical, introducing the essential terminology needed to report our experimental results. In Sec. III, we develop the theory underlying single-setting measurements of QWEs via two-copy Bell sampling experiments. All our experimental demonstrations are then reported in Sec. IV. We prove performance guarantees concerning the scalability of our protocol in Sec. V. Lastly, in Sec. VI, we leverage QWEs to theoretically analyze the noise resilience of entanglement for certain quantum states on up to $n = 1000$ qubits.

II. QUANTUM WEIGHT ENUMERATORS

In 1962, MacWilliams discovered that the Hamming weight distribution of a classical linear code uniquely determines that of its dual, and vice versa [57]. Her discovery sparked a research program about error-correcting codes [58–61] that quickly found its way into the quantum realm [51–56] after the first *quantum error-correcting code* (QECC) had been constructed [46]. At the core of the quantum weight enumerator machinery lies the quantum MacWilliams transform, a linear involution, which is traditionally formulated in terms of polynomial identities.

In this section, we review this enumerator machinery from a fresh perspective that is intended to improve the clarity of our experimental demonstrations in Sec. IV. First, we avoid the abstract language of polynomial rings and instead place the linear algebra behind the quantum MacWilliams transform into the center of the discussion. Second, following the literature about sector lengths, we define all enumerators in terms of quantum states ρ rather than code space projectors Π . The latter concept is recovered (after appropriate renormalization) as a special case of the former when specializing to the state

$$\rho_{\text{QECC}} = \frac{\Pi}{\text{Tr}[\Pi]}, \quad (1)$$

which carries the physical interpretation of the maximally mixed state inside the code space of the QECC.

A. High-level overview of enumerators and examples

Before we delve into the various applications and interpretations of *quantum weight enumerators* (QWEs), let us first

explain the general theory using a simple example: consider the state vectors $|0, 0\rangle$ and $|\Phi^+\rangle = \frac{1}{\sqrt{2}}(|0, 0\rangle + |1, 1\rangle)$. An important difference between them is that $|0, 0\rangle$ is only correlated in the Z -basis while $|\Phi^+\rangle$ is perfectly (anti-)correlated in three different bases, namely $\langle 0, 0 | (Z \otimes Z) | 0, 0 \rangle = 1$, $\langle \Phi^+ | (X \otimes X) | \Phi^+ \rangle = \langle \Phi^+ | (Z \otimes Z) | \Phi^+ \rangle = 1$, and $\langle \Phi^+ | (Y \otimes Y) | \Phi^+ \rangle = -1$. The term “weight” in QWEs refers to the weight of multi-qubit Pauli operators. The expressions above are examples of weight-2 Pauli correlations. It turns out that the only other non-vanishing correlations are given by $\langle 0, 0 | (I \otimes I) | 0, 0 \rangle = \langle \Phi^+ | (I \otimes I) | \Phi^+ \rangle = 1$ (weight 0) and $\langle 0, 0 | (Z \otimes I) | 0, 0 \rangle = \langle 0, 0 | (I \otimes Z) | 0, 0 \rangle = 1$ (weight 1). The Shor-Laflamme QWE distribution (SLD) allows us to distinguish the two states by summarizing the information above into normalized vectors of the form $\mathbf{a} = (a_0, a_1, a_2)$ that are defined in full generality in Eq. (10) below. Here, we have

$$\mathbf{a} [|0, 0\rangle \langle 0, 0|] = (0.25, 0.5, 0.25) \quad \text{and} \quad (2)$$

$$\mathbf{a} [|\Phi^+\rangle \langle \Phi^+|] = (0.25, 0.0, 0.75). \quad (3)$$

Note that $a_2[|\Phi^+\rangle \langle \Phi^+|] = 0.75$ is three times as large as $a_2[|0, 0\rangle \langle 0, 0|] = 0.25$ reflecting the fact that $|\Phi^+\rangle$ is perfectly correlated in three times as many bases as $|0, 0\rangle$. This also proves that $|\Phi^+\rangle$ is entangled (see Eq. (14) below).

Another way to demonstrate that $|\Phi^+\rangle$ is entangled is by examining the purities of its subsystems. The set $\{1, 2\}$, which labels the qubits has four subsets: \emptyset , $\{1\}$, $\{2\}$, and $\{1, 2\}$. Thus, any two-qubit state ρ has four marginals: the (trivial) (zero-qubit state $\rho_{\emptyset} = 1$, the one-qubit states $\rho_{\{1\}}$ and $\rho_{\{2\}}$, and the global state $\rho_{\{1,2\}} = \rho$. For $|0, 0\rangle$ and $|\Phi^+\rangle$, the single-qubit marginals are $|0\rangle\langle 0|$ (pure) and $\mathbb{1}/2$ (maximally mixed), respectively. Thus, the single-qubit subsystem purities are given by $\text{Tr}[|0\rangle\langle 0|^2] = 1$ and $\text{Tr}[(\mathbb{1}/2)^2] = 0.5$, respectively. This information is captured by Rains’ unitary QWEs, which are vectors of the form $\mathbf{a}' = (a'_0, a'_1, a'_2)$ that are defined in full generality in Eq. (28) below. The entries of \mathbf{a}' are (averaged) subsystem purities, where the subscripts refer to subsystem sizes. In our example, we have

$$\mathbf{a}' [|0, 0\rangle \langle 0, 0|] = (1.0, 1.0, 1.0) \quad \text{and} \quad (4)$$

$$\mathbf{a}' [|\Phi^+\rangle \langle \Phi^+|] = (1.0, 0.5, 1.0). \quad (5)$$

Since the entries of $\mathbf{a}' [|\Phi^+\rangle \langle \Phi^+|]$ obey $a'_2 > a'_1$, we can conclude that $|\Phi^+\rangle$ is entangled (see Eq. (32) below).

These two features, Pauli correlations and subsystem purities, are in fact two sides of the same medal: one can always convert the SLD into the vector of Rains’ unitary QWEs, and vice versa [53]. This relationship can be elegantly illuminated through the linear algebra underlying the *quantum MacWilliams identity* [51], see Fig. 1. This identity can be phrased as the linear equation (top row in Fig. 1)

$$M\mathbf{a}[\rho] = \mathbf{b}[\rho], \quad (6)$$

where ρ is an arbitrary n -qubit states, $\mathbf{a}[\rho]$ and $\mathbf{b}[\rho]$ are its SLD and dual SLD (defined below), and $M = (M_{i,j})_{i,j=0}^n$ is the *MacWilliams transform* for additive codes over the field \mathbb{F}_4 [52]. The latter can be identified with the set $\{I, X, Y, Z\}$

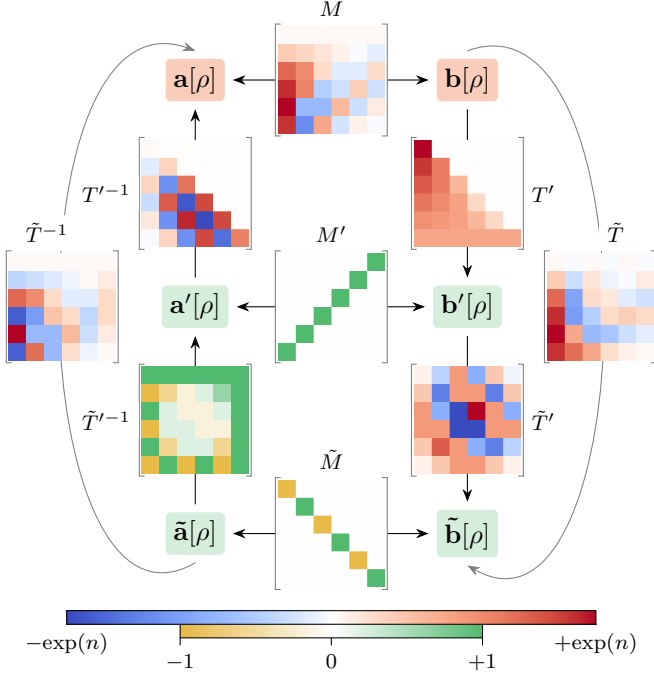


FIG. 1. The self-inverse MacWilliams transforms M , M' , and \tilde{M} convert QWEs (left) into dual QWEs (right). They represent the same linear map in three different bases of \mathbb{R}^{n+1} that correspond to Shor-Laflamme QWEs (top), Rains' unitary QWEs (center), and Rains' shadow QWEs (bottom). The three transforms are related via basis change matrices T' , \tilde{T} , and \tilde{T}^{-1} , e.g., $M' = T' M T'^{-1}$. Plotted are the matrix entries in the special case of $n = 5$ qubits, where red and blue (green and yellow) colors show which matrices have entries that are exponentially diverging (bounded by ± 1) in the general case of n qubits.^a In Thm. 3, we show that Rains' shadow QWEs $\tilde{\mathbf{a}}[\rho]$ are the same as the triplet probability distribution obtained in a Bell sampling experiment on $\rho \otimes \rho$, where ρ is any n -qubit state. Thus, one can efficiently measure $\tilde{\mathbf{a}}[\rho]$ in experiments, which we demonstrate in Sec. IV. Note that statistical errors on $\tilde{\mathbf{a}}[\rho]$ never uncontrollably spread onto Rains' unitary QWEs $\mathbf{a}'[\rho]$ as the entries of \tilde{T}^{-1} are bounded by ± 1 , see Thm. 8. For some states ρ , however, errors can unfavorably amplify during the transform to the SLD $\mathbf{a}[\rho]$ because some matrix entries of \tilde{T}^{-1} are exponentially large. This hints to profound complexity-theoretic origins that we discuss in Sec. V. For a concise overview of the matrix definitions, see App. A.

^a Digital feature: interactive version of this figure for arbitrary $n < 500$.

of single-qubit Pauli operators. The entries of MacWilliams' transform are given by

$$M_{i,j} = \frac{1}{2^n} \sum_{l=0}^n \binom{n-j}{i-l} \binom{j}{l} (-1)^l 3^{i-l}, \quad (7)$$

which are just the coefficients in front of x^i in the polynomial $f_j(x) = 2^{-n}(1+3x)^{n-j}(1-x)^j$ [59]. These matrix entries are explicitly shown at the top of Fig. 1 with positive values in red and negative values in blue, where stronger haze indicates larger magnitude. The normalization factor in Eq. (7) ensures that M is self-inverse.

Another self-inverse matrix is $M' = (M'_{i,j})_{i,j=0}^n$, the anti-diagonal matrix (middle of Fig. 1) with entries

$$M'_{i,j} = \delta_{i,n-j}. \quad (8)$$

For M' and the other matrices in Fig. 1 whose entries are bounded by ± 1 , we use green and yellow colors to highlight the fact these transformations are better conditioned compared to those in red and blue. As it turns out [53], M and M' are the same up to a basis change matrix T' (defined in Eq. (29) below), which relates the two via $M' = T' M T'^{-1}$. Strikingly, the same basis change matrix also transforms (dual) SLDs into (dual) Rains unitary QWEs. In other words, we have $\mathbf{a}'[\rho] = T' \mathbf{a}[\rho]$ and $\mathbf{b}'[\rho] = T' \mathbf{b}[\rho]$ (top right in Fig. 1) for all n -qubit states ρ , where the dual Rains' unitary enumerators are defined as $\mathbf{b}'[\rho] = M' \mathbf{a}'[\rho]$ (central row in Fig. 1).

In the basis of Rains' unitary enumerators, it is obvious that $\text{Tr}[M] = \text{Tr}[M'] = \delta_{n,\text{even}}$. Hence, the $(+1)$ -eigenspace of M has dimension $\lceil \frac{n+1}{2} \rceil$, whereas its (-1) -eigenspace is $\lfloor \frac{n+1}{2} \rfloor$ -fold degenerate. This implies the existence of a matrix \tilde{T} (right of Fig. 1) that diagonalizes $M = \tilde{T}^{-1} \tilde{M} \tilde{T}$ into

$$\tilde{M} = \text{diag}((-1)^n, \dots, -1, 1, -1, 1) \quad (9)$$

(bottom in Fig. 1). Here we point out, for the first time to our knowledge, that one can choose \tilde{T} (defined in Eq. (39) below) to be the matrix which converts SLDs into a third notion of QWEs: Rains' shadow enumerators $\tilde{\mathbf{a}}[\rho]$ (bottom left in Fig. 1). This insight clarifies the role of Rains' shadow enumerators in the linear algebra underlying the MacWilliams transform M .

For more details about these transformations and basis change matrices, see App. A–B. Below, we provide an overview by listing the three notions of QWEs and linking them to their definitions.

- (i) Shor-Laflamme's QWEs, defined in Eq. (10): $\mathbf{a}[\rho]$.
- (ii) Rains' unitary QWEs, defined in Eq. (28): $\mathbf{a}'[\rho]$.
- (iii) Rains' shadow QWEs, defined in Eq. (37): $\tilde{\mathbf{a}}[\rho]$.

B. Shor and Laflamme's QWEs

The first notion of QWEs reviewed here is that coined by Shor and Laflamme [51]. For an n -qubit state ρ , we define the *Shor-Laflamme QWE distribution* (SLD) as $\mathbf{a}[\rho] = (a_i[\rho])_{i=0}^n$, where

$$a_i[\rho] = \frac{1}{2^n} \sum_{\substack{P \in \{I, X, Y, Z\}^{\otimes n} \\ \text{wt}(P)=i}} \text{Tr}[\rho P]^2. \quad (10)$$

Here, $\text{wt}(P)$ is the *weight* of an n -qubit Pauli operator P , i.e., its number of non-identity tensor factors. Similarly, the dual SLD is defined as $\mathbf{b}[\rho] = (b_i[\rho])_{i=0}^n$, where

$$b_i[\rho] = \frac{1}{2^n} \sum_{\substack{P \in \{I, X, Y, Z\}^{\otimes n} \\ \text{wt}(P)=i}} \text{Tr}[\rho P \rho P]. \quad (11)$$

Note that our normalization differs from that of Ref. [51]. This has the advantage that the purity of ρ decomposes into

$$\text{Tr}[\rho^2] = \sum_{i=0}^n a_i[\rho] \quad (12)$$

and MacWilliams' identity [57] simplifies to $\mathbf{b}[\rho] = M\mathbf{a}[\rho]$. The state ρ is pure if and only if (iff) $\mathbf{a}[\rho] = \mathbf{b}[\rho]$ lies in the $+1$ -eigenspace of M because $\mathbf{b}[\rho]$ is always a normalized probability distribution.

SLDs have the following useful properties: (i) for every n -qubit state ρ and $i \in \{0, \dots, n\}$, the so-called *i -body sector length*, $a_i[\rho]$, is invariant under local unitaries [53],

$$a_i[\Psi_1 \otimes \dots \otimes \Psi_n] = a_i[|0\rangle\langle 0|^{\otimes n}] = \frac{1}{2^n} \binom{n}{i}, \quad (13)$$

where $\Psi_1 \otimes \dots \otimes \Psi_n$ is any pure product state; (ii) due to the triangle inequality, $a_i[\rho]$ is convex in ρ . In other words, SLDs can only decrease under incoherent mixtures. In combination, these two properties show

$$a_n[\rho] > \frac{1}{2^n} \implies \rho \text{ entangled}, \quad (14)$$

which we refer to as *n -body sector length criterion* [73]. Note that the criterion in Eq. (14) is a vast generalization of the well-known entanglement criterion for noisy n -qubit states ρ , “ $\text{Tr}[\rho(X^{\otimes n})]^2 + \text{Tr}[\rho(Z^{\otimes n})]^2 > 1 \implies \rho$ entangled”, which connects back to our introductory example of $|\Phi^+\rangle$ being perfectly correlated in more than one basis.

Under the physically well-motivated local depolarizing noise channel, SLDs decay as [56],

$$a_i[\mathcal{E}_p^{\otimes n}[\rho]] = (1-p)^{2i} a_i[\rho], \quad (15)$$

where $\mathcal{E}_p[\cdot] = (1-p)[\cdot] + p\frac{1}{2}$ denotes the single-qubit depolarizing channel with error strength $p \in [0, 1]$. Inserting Eq. (15) into Eq. (12) shows that purities decay as

$$\text{Tr}[(\mathcal{E}_p^{\otimes n}[\rho])^2] = \sum_{i=0}^n a_i[\rho](1-p)^{2i} \quad (16)$$

under local depolarizing noise. Our first technical contribution is an analog of Eq. (16) for fidelities rather than purities:

Lemma 1 (Decay of overlap under local depolarizing noise) *Let ρ be an n -qubit state, $\mathbf{a}[\rho] = (a_i[\rho])_{i=0}^n \in \mathbb{R}^{n+1}$ its SLD, and $p \in [0, 1]$ a noise parameter. Then, it holds*

$$\text{Tr}[\rho \mathcal{E}_p^{\otimes n}[\rho]] = \sum_{i=0}^n a_i[\rho](1-p)^i. \quad (17)$$

Proof: See App. C. \square

Lemma 1 is especially useful for pure states $\Psi = |\psi\rangle\langle\psi|$, for which the overlap $\text{Tr}[\Psi\sigma]$ with any other state σ is the same as the fidelity $\langle\psi|\sigma|\psi\rangle$. Furthermore, if Ψ is a *genuinely multipartite entangled* (GME) stabilizer state—which implies

that the operator $\frac{1}{2} - \Psi$ is a GME witness [82–85]—it follows that the noisy state $\sigma = \mathcal{E}_p^{\otimes n}[\Psi]$ remains GME as long as

$$\sum_{i=0}^n a_i[\Psi](1-p)^i > 0.5. \quad (18)$$

We refer to this as the *fidelity criterion for stabilizer states*. This and other entanglement criteria [Eqs. (14), (32), (82)] that can be tested via SLDs motivates computing them, which has been achieved for *Greenberger-Horne-Zeilinger* (GHZ) [86] and for 1-dimensional periodic *cluster states* [87] by counting their weight- i stabilizer operators. Indeed, even in the more general case where

$$\rho_{\text{QECC}}^{\text{stab}} = \frac{1}{2^n} \sum_{S \in \mathcal{S}} S \quad (19)$$

is the maximally mixed state [Eq. (1)] within the code space of an $[[n, k, d]]$ QECC with stabilizer group \mathcal{S} [1], one can find the i -body sector length

$$a_i[\rho_{\text{QECC}}^{\text{stab}}] = \frac{1}{2^n} |\{S \in \mathcal{S} \mid \text{wt}(S) = i\}|, \quad (20)$$

by counting weight- i stabilizer operators.

Let us derive a well-known expression, similar to Eq. (20), for the dual SLD $\mathbf{b}[\rho]$. Leveraging the SWAP trick [88], we can rewrite Eq. (11) as

$$b_i[\rho] = \frac{1}{4^n} \sum_{\substack{P, Q \in \{I, X, Y, Z\}^{\otimes n} \\ \text{wt}(P)=i}} \text{Tr}[\rho Q]^2 (-1)^{\delta_{PQ, QP}}. \quad (21)$$

If $\rho = \rho_{\text{QECC}}^{\text{stab}}$, then the map $\{I, X, Y, Z\}^{\otimes n} \rightarrow \mathbb{R}$,

$$Q \mapsto \text{Tr}[\rho_{\text{QECC}}^{\text{stab}} Q]^2 = \begin{cases} 1 & \text{if } Q \in \mathcal{S}, \\ 0 & \text{if } Q \notin \mathcal{S}, \end{cases} \quad (22)$$

is the indicator function on \mathcal{S} [89] and Eq. (21) simplifies to

$$b_i[\rho_{\text{QECC}}^{\text{stab}}] = \frac{1}{4^n} \sum_{\substack{P \in \{I, X, Y, Z\}^{\otimes n} \\ \text{wt}(P)=i}} \sum_{S \in \mathcal{S}} (-1)^{\delta_{PS, SP}}. \quad (23)$$

Clearly, the inner sum in Eq. (23) equates to $|\mathcal{S}| = 2^{n-k}$ whenever P is contained in the normalizer of \mathcal{S} ,

$$\mathcal{S}^\perp = \{P \in \{I, X, Y, Z\}^{\otimes n} \mid \forall S \in \mathcal{S} : SP = PS\}, \quad (24)$$

which is also known as the logical Pauli group of the QECC—both modulo global phases [1]. Conversely, if $P \notin \mathcal{S}^\perp$, the inner sum in Eq. (23) is equal to zero. In other words, the map $\{I, X, Y, Z\}^{\otimes n} \rightarrow \mathbb{R}$,

$$P \mapsto \frac{1}{|\mathcal{S}|} \sum_{S \in \mathcal{S}} (-1)^{\delta_{PS, SP}} \quad (25)$$

is the indicator function on \mathcal{S}^\perp . Therefore,

$$b_i[\rho_{\text{QECC}}^{\text{stab}}] = \frac{1}{2^{n+k}} |\{P \in \mathcal{S}^\perp \mid \text{wt}(P) = i\}| \quad (26)$$

is precisely equal to the probability that a logical Pauli operator $P \in \mathcal{S}^\perp$ (drawn uniformly at random) fulfills $\text{wt}(P) = i$. Since \mathcal{S}^\perp is just the dual of \mathcal{S} considered as an additive code over \mathbb{F}_4 [61], the name “*dual SLD*” for $\mathbf{b}[\rho]$ is justified.

Finally, note that—for arbitrary $[[n, k, d]]$ codes [Eq. (1)]—the discrepancy between $\mathbf{a}[\rho_{\text{QECC}}]$ and $\mathbf{b}[\rho_{\text{QECC}}]$ reveals the code’s distance

$$d = \min \{i > 0 \mid a_i[\rho_{\text{QECC}}] < 2^k b_i[\rho_{\text{QECC}}]\}. \quad (27)$$

This is clear for stabilizer QECCs, where $2^n a_i[\rho_{\text{QECC}}^{\text{stab}}]$ and $2^{n+k} b_i[\rho_{\text{QECC}}^{\text{stab}}]$ are equal to the number of weight- i stabilizers [Eq. (20)] and logicals [Eq. (26)], respectively, and remains true for non-stabilizer QECCs [51].

C. Rains’ unitary QWEs

The second notion of QWEs reviewed here is most easily explained in terms of subsystem purities. The reduced state $\rho_S = \text{Tr}_{S^c}[\rho]$ on a subset of qubits $S \subseteq \{1, \dots, n\}$ is obtained from ρ by tracing out the qubits in the complement $S^c = \{1, \dots, n\} \setminus S$. We denote the average of the subsystem purity $\text{Tr}[\rho_S^2]$ over all marginals of a fixed size $i \in \{0, \dots, n\}$ by

$$a'_i[\rho] = \frac{1}{\binom{n}{i}} \sum_{\substack{S \subseteq \{1, \dots, n\} \\ |S|=i}} \text{Tr}[\rho_S^2], \quad (28)$$

which is the definition of Rains’ unitary QWEs with a more physically-motivated normalization [53]. Here, we will often refer to the vector $\mathbf{a}'[\rho] = (a'_i[\rho])_{i=0}^n$ of Rains’ unitary QWEs as *averaged purity distribution* (APD).

In the exact case without statistical errors, APDs and SLDs carry exactly the same information about ρ since they can be linearly converted into each other via $\mathbf{a}'[\rho] = T' \mathbf{a}[\rho]$ and $\mathbf{a}[\rho] = T'^{-1} \mathbf{a}'[\rho]$, where

$$T'_{i,j} = 2^{n-i} \binom{n}{i}^{-1} \binom{n-j}{n-i} \quad (29)$$

$$\text{and } T'^{-1}_{i,j} = 2^{j-n} \binom{n}{j} \binom{n-j}{n-i} (-1)^{i+j}. \quad (30)$$

The fact that T' and T'^{-1} are lower-triangular matrices can be seen in Fig. 1. Following Rains, we dually define $\mathbf{b}'[\rho] = M' \mathbf{a}'[\rho]$, where M' from Eq. (8) is the MacWilliams matrix in the basis of the APD [53]. Since $M' = T' M T'^{-1}$ is the antidiagonal matrix, $\mathbf{b}'[\rho] = (a'_{n-j}[\rho])_{j=0}^n$ is just the reversed APD. In the APD picture, it is clear (via subsystem symmetry of the Schmidt decomposition) that ρ is pure iff $\mathbf{a}'[\rho] = \mathbf{b}'[\rho]$. Moreover, $a'_i[\rho] < a'_n[\rho] = \text{Tr}[\rho^2]$ means that some marginals are more mixed than the global state. This implies that ρ must be entangled [90, 91]. Empirically [87], the most noise-robust version of these entanglement criteria is attained for $i = n-1$, where Rains’ unitary QWE takes the simple form

$$a'_{n-1}[\rho] = \frac{1}{n} \sum_{i=1}^n \text{Tr}[(\text{Tr}_{\{i\}}[\rho])^2]. \quad (31)$$

Unless specified otherwise, we will thus refer to

$$a'_{n-1}[\rho] < a'_n[\rho] \implies \rho \text{ entangled} \quad (32)$$

as the *purity criterion* in the present work.

A related concept in the theory of entanglement that is also captured by QWEs is that of *m-uniform* states and *absolutely maximally entangled* (AME) states. A pure state $\Psi = |\psi\rangle\langle\psi|$ is called *m-uniform* iff all of its *m*-body marginals are maximally mixed, i.e., iff $a'_m[\Psi] = 2^{-m}$. It is a simple and insightful exercise [using Eq. (29)] to show that—on the level of SLDs—the *m-uniformity* condition $a'_m[\Psi] = 2^{-m}$ can be equivalently expressed as

$$a_1[\Psi] = \dots = a_m[\Psi] = 0. \quad (33)$$

By the Schmidt decomposition, the largest value of *m* for which there is any hope for Eq. (33) to hold is $m = \lfloor \frac{n}{2} \rfloor$. In this case, Ψ is called an AME state. For qubits, such AME states only exist for $n \in \{2, 3, 5, 6\}$ parties [92].

Finally, note that—in the APD picture—Eq. (27) translates into $a'_{d-1}[\rho_{\text{QECC}}] = 2^k b'_{d-1}[\rho_{\text{QECC}}]$ [53].

D. Rains’ shadow QWEs

When Rains introduced the notion of quantum shadow enumerators [54], he took inspiration from the classical coding literature [93]. Here, however, we find it more constructive to provide a physical introduction to this concept. Let ρ be an *n*-qubit state, ρ^\top its transpose in the computational basis, and $\rho \mapsto \tilde{\rho}$ the *state inversion map*, where

$$\tilde{\rho} = Y^{\otimes n} \rho^\top Y^{\otimes n} \quad (34)$$

is the *spin-flipped* state [94–97]. The name of $\tilde{\rho}$ stems from the fact that in the case of a single qubit $\rho = \frac{1+\mathbf{r}\cdot\boldsymbol{\sigma}}{2}$ with Bloch sphere vector $\mathbf{r} \in \mathbb{R}^3$ (aka spin), the state inversion map is flipping the spin $\mathbf{r} \mapsto -\mathbf{r}$, i.e., $\tilde{\rho} = \frac{1-\mathbf{r}\cdot\boldsymbol{\sigma}}{2}$. This map should not be confused with the “bitflip” channel $\rho \mapsto X\rho X$, where the spin is in fact rotated (not flipped) around the *x*-axis of the Bloch sphere. The spin flip operation is not a rotation and hence is impossible [98] to physically implement for an unknown quantum state ρ . In more technical terms, the state inversion map $\rho \mapsto \tilde{\rho}$ is positive but not completely positive. This already hints to the fact that this concept can capture certain aspects of entanglement. Other useful expressions of the spin-flipped state include [97, 99]

$$\tilde{\rho} = \frac{1}{2^n} \sum_{P \in \{I, X, Y, Z\}^{\otimes n}} (-1)^{\text{wt}(P)} \text{Tr}[\rho P] P \quad (35)$$

$$\text{and } \tilde{\rho} = \frac{1}{2^n} \sum_{S \subseteq \{1, \dots, n\}} (-1)^{|S|} \rho_S \otimes \mathbb{1}_{S^c}. \quad (36)$$

Now we are in the position to state the definition of *Rains’ shadow QWEs* [54], namely

$$\tilde{a}_i[\rho] = \frac{1}{2^n} \sum_{\substack{P \in \{I, X, Y, Z\}^{\otimes n} \\ \text{wt}(P)=i}} \text{Tr}[\rho P \tilde{\rho} P]. \quad (37)$$

Our normalization convention, which differs from the original one in Ref. [54], ensures that $\sum_{i=0}^n \tilde{a}_i[\rho] = 1$. Together with Rains' shadow inequalities [54],

$$\tilde{a}_i[\rho] \geq 0, \quad (38)$$

this implies that $\tilde{\mathbf{a}}[\rho] = (\tilde{a}_i[\rho])_{i=0}^n$ (like $\mathbf{b}[\rho]$ but unlike $\mathbf{a}[\rho]$) is always a probability distribution; see Thm. 3 below for its physical interpretation. Also Rains' shadow enumerators $\tilde{\mathbf{a}}[\rho] = \tilde{T}\mathbf{a}[\rho]$ can be obtained from the SLD by applying the matrix \tilde{T} that arises from MacWilliams' transform [Eq. (7)] after alternating the sign of its columns, i.e.,

$$\tilde{T}_{i,j} = (-1)^j M_{i,j}. \quad (39)$$

The fact that $\mathbf{a}[\rho]$, $\mathbf{b}[\rho]$, and $\tilde{\mathbf{a}}[\rho]$ have non-negative entries and are in linear relationship with each other—applied to ρ_{QECC} from Eq. (1)—is what Rains exploited in his landmark work [54] to prove that arbitrary $[[n, k, d]]$ QECCs have a distance [Eq. (27)] of $d \leq \frac{n}{3} + 2$. Later, similar strategies were employed to rule out the existence of AME and, more generally, m -uniform states with certain parameters [100].

Let us explain why Rains called $\tilde{\mathbf{a}}[\rho]$ quantum shadow enumerators. As in Eq. (21), we can always write

$$\text{Tr}[\rho P \tilde{\rho} P] = \frac{1}{2^n} \sum_Q \text{Tr}[\rho Q] \text{Tr}[\tilde{\rho} Q] (-1)^{\delta_{PQ, QP}} \quad (40)$$

where the sum runs over all $Q \in \{I, X, Y, Z\}^{\otimes n}$. Further exploiting $\text{Tr}[\rho^T Q] = (-1)^{\delta_{Q, Q^T}} \text{Tr}[\rho Q]$ and accounting for a potential minus sign (if Q and $\mathbf{Y} = Y^{\otimes n}$ anticommute) yields

$$\text{Tr}[\rho P \tilde{\rho} P] = \frac{1}{2^n} \sum_Q \text{Tr}[\rho Q]^2 (-1)^{\delta_{Q, Q^T} + \delta_{Q\mathbf{Y}, \mathbf{Y}Q} + \delta_{PQ, QP}}. \quad (41)$$

Since $Q = Q^T$ iff the number of Y -operators in Q is even and $Q\mathbf{Y} = \mathbf{Y}Q$ iff the combined number of X - and Z -operators in Q is even, we obtain

$$(-1)^{\delta_{Q, Q^T} + \delta_{Q\mathbf{Y}, \mathbf{Y}Q}} = (-1)^{\text{wt}(Q)}. \quad (42)$$

As in Sec. II B above, we now consider the special case of an $[[n, k, d]]$ stabilizer QECC with stabilizer group \mathcal{S} . Combining Eqs. (19), (34), (37), (41), and (42) we find

$$\tilde{a}_i[\rho_{\text{QECC}}^{\text{stab}}] = \frac{1}{4^n} \sum_{\substack{P \in \{I, X, Y, Z\}^{\otimes n} \\ \text{wt}(P)=i}} \sum_{S \in \mathcal{S}} (-1)^{\text{wt}(S) + \delta_{PS, SP}} \quad (43)$$

in direct analogy to Eq. (23). Clearly, the inner sum in Eq. (43) equates to $|\mathcal{S}| = 2^{n-k}$ if $P \in \{I, X, Y, Z\}^{\otimes n}$ is contained in

$$\tilde{\mathcal{S}} = \{P \mid \forall S \in \mathcal{S} : PS = (-1)^{\text{wt}(S)} SP\}. \quad (44)$$

The subset $\tilde{\mathcal{S}} \subseteq \{I, X, Y, Z\}^{\otimes n}$ is what Rains called the *shadow* of \mathcal{S} in Ref. [54], building on older notions of shadows of classical error-correcting codes pioneered by Conway and Sloane in 1990 [93]. Note that this concept has nothing to

do with modern notions of classical shadows [21–25]. If, on the other hand, P is not contained in $\tilde{\mathcal{S}}$, then the inner sum in Eq. (43) vanishes. Hence, the map $\{I, X, Y, Z\}^{\otimes n} \rightarrow \mathbb{R}$,

$$P \mapsto \frac{1}{|\mathcal{S}|} \sum_{S \in \mathcal{S}} (-1)^{\text{wt}(S) + \delta_{PS, SP}} \quad (45)$$

is the indicator function on Rains' shadow $\tilde{\mathcal{S}}$. Therefore,

$$\tilde{a}_i[\rho_{\text{QECC}}^{\text{stab}}] = \frac{1}{2^{n+k}} |\{P \in \tilde{\mathcal{S}} \mid \text{wt}(P) = i\}| \quad (46)$$

is precisely equal to the probability of an element in Rains' shadow $\tilde{\mathcal{S}}$ (drawn uniformly at random) having Pauli weight equal to i . In the special case of stabilizer QECCs, the fact that Rains' QWEs are a normalized probability distribution, i.e., $|\tilde{\mathcal{S}}| = 2^{n+k}$ thus follows from the following characterization:

Lemma 2 (Rains' shadow is a coset of the normalizer group) *Let \mathcal{S} be the stabilizer group of an $[[n, k, d]]$ QECC and $\tilde{\mathcal{S}}$ Rains' shadow of \mathcal{S} . For every $P \in \tilde{\mathcal{S}}$, it holds*

$$\tilde{\mathcal{S}} = PS^\perp. \quad (47)$$

Moreover, we can choose $P = I$ in Eq. (47) iff \mathcal{S} admits a set of generators S_1, \dots, S_{n-k} such that $\text{wt}(S_i)$ is even for all $i \in \{1, \dots, n-k\}$.

Proof: First, let $Q \in \tilde{\mathcal{S}}$ be an arbitrary element in the shadow and consider the operator $L = PQ$. For all stabilizers $S \in \mathcal{S}$ we thus have $PS = SP(-1)^{\text{wt}(S)}$, $QS = SQ(-1)^{\text{wt}(S)}$, and therefore $LS = SL$, i.e., $L \in \mathcal{S}^\perp$ is a logical Pauli operator. We have thus shown the first inclusion $\tilde{\mathcal{S}} \subseteq PS^\perp$. For the other inclusion, consider $Q \in PS^\perp$, i.e., $Q = PL$ for some $L \in \mathcal{S}$. Then, we have $SQ = SPL = PSL(-1)^{\text{wt}(S)} = PLS(-1)^{\text{wt}(S)} = QS(-1)^{\text{wt}(S)}$, which proves $\tilde{\mathcal{S}} \supseteq PS^\perp$.

Concerning the addendum, if we can choose $P = I$, then $\tilde{\mathcal{S}} = \mathcal{S}^\perp$. Comparing their definitions, Eqs. (24) and (44), it is clear that \mathcal{S} cannot contain elements whose weight is odd. Conversely, if \mathcal{S} is generated by some even-weight stabilizers, then all elements in the Abelian group \mathcal{S} have an even weight and the anticommutativity condition in Eq. (44) is vacuous. This then shows $\tilde{\mathcal{S}} = \mathcal{S}^\perp$ and completes the proof. \square

III. MEASURING QWES VIA BELL SAMPLING

Now that we have reviewed the existing notions of QWEs, let us turn to our first main result: a comprehensive theoretical framework for measuring QWEs in practice, by exploiting a new connection to Bell sampling. Two-copy Bell sampling is a technique for certifying and quantifying entanglement in many-body quantum systems that is well established both in theory [34, 101–104] and experiment [10, 28, 43–45]. It relies on the so-called SWAP trick [105, 106], which allows us to write the purity of a single-qubit state ρ as

$$\text{Tr}[\rho^2] = \text{Tr}[(\rho \otimes \rho)\text{SWAP}]. \quad (48)$$

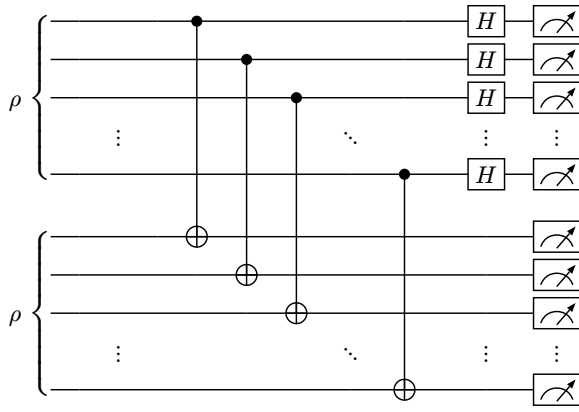


FIG. 2. Quantum circuit for a Bell sampling experiment with two copies of an n -qubit state ρ . As discussed in the main text, this single-setting experiment allows us to measure the QWEs of ρ . In the special case of $\rho = \rho_{\text{QECC}}$ [Eq. (1)], this enables access to the QWEs of any QECC under investigation. If the measurement outcomes of a qubit pair (connected via a CNOT) are both equal to 1, the qubits are effectively projected into a singlet; otherwise into a triplet. By Thm. 3, the resulting triplet probability distribution [Eq. (77)] is the same as Rains’ shadow QWEs [Eq. (37)]. From this, one can compute the other QWEs by applying appropriate transforms from Fig. 1.

$\text{SWAP} = |0, 0\rangle\langle 0, 0| + |0, 1\rangle\langle 1, 0| + |1, 0\rangle\langle 0, 1| + |1, 1\rangle\langle 1, 1|$ is the operator that decomposes the two-qubit Hilbert space $\mathbb{C}^2 \otimes \mathbb{C}^2$ into a direct sum of its symmetric and antisymmetric subspace [107]. The former is three-dimensional and spanned by the *triplet* state vectors

$$|\Phi^+\rangle = \frac{1}{\sqrt{2}}(|0, 0\rangle + |1, 1\rangle), \quad (49)$$

$$|\Psi^+\rangle = \frac{1}{\sqrt{2}}(|0, 1\rangle + |1, 0\rangle), \quad (50)$$

$$\text{and } |\Phi^-\rangle = \frac{1}{\sqrt{2}}(|0, 0\rangle - |1, 1\rangle), \quad (51)$$

while the latter is one-dimensional and spanned by the *singlet* state vector

$$|\Psi^-\rangle = \frac{1}{\sqrt{2}}(|0, 1\rangle - |1, 0\rangle). \quad (52)$$

The four vectors in Eqs. (49)–(52) are well known under the name *Bell basis*. The projection-valued measure that distinguishes them is commonly referred to as *Bell measurement*. In practice, Bell measurements are usually realized by applying a two-qubit CNOT gate and reading out control and target qubits in the X - and Z -basis, respectively, see Fig. 2. For our purposes, it suffices to differentiate triplets from singlets (without fine-graining triplets), which amounts to estimating the probability $\langle \Psi^- | (\rho \otimes \rho) | \Psi^- \rangle$ of projecting $\rho \otimes \rho$ into a singlet. Indeed, inserting the expression $\text{SWAP} = \mathbb{1} - 2 |\Psi^-\rangle\langle \Psi^-|$ into Eq. (48), we can write

$$\text{Tr}[\rho^2] = 1 - 2 \langle \Psi^- | (\rho \otimes \rho) | \Psi^- \rangle. \quad (53)$$

In the more general case where we have access to two copies of an n -qubit state ρ , the situation is similar: perform a Bell measurement on qubit pair $(s, n + s)$ for all $s \in \{1, \dots, n\}$

and denote the outcome by $\alpha_s \in \{\Phi^\pm, \Psi^\pm\}$. Then, the overall outcome of the two-copy Bell sampling experiment is the $2n$ -qubit state vector

$$|\alpha\rangle = \bigotimes_{s=1}^n |\alpha_s\rangle_{s, n+s}. \quad (54)$$

We denote the number of singlets in $|\alpha\rangle$ by

$$\text{sing}(\alpha) = |\{s \in \{1, \dots, n\} \mid |\alpha_s\rangle = |\Psi^-\rangle\}|. \quad (55)$$

The purity of ρ can then be estimated as the difference between probabilities of finding an even and odd number of singlets, respectively [45]. That is,

$$\text{Tr}[\rho^2] = 1 - 2 \sum_{\substack{\alpha \in \{\Phi^\pm, \Psi^\pm\}^n \\ \text{sing}(\alpha) \equiv 1 \pmod{2}}} \langle \alpha | (\rho \otimes \rho) | \alpha \rangle. \quad (56)$$

Estimating purities through two-copy Bell measurements is remarkably efficient: only $O(\epsilon^{-2})$ samples are required for estimating $\text{Tr}[\rho^2]$ up to additive error $\epsilon > 0$. For a similar result about QWEs, see Thm. 8 below. On the other hand, all single-copy protocols for measuring purities unavoidably suffer from an exponential (in n) sample complexity [27]. This example clearly illustrates the power of the paradigm of so-called *quantum memories* where part of the postprocessing (after preparing copies of ρ) is performed quantumly *before* the measurement [27–31]. Here we extend the power of quantum memories into the realm of QWEs. As we show next, two-copy Bell sampling lends itself to unbiased single-shot and single-setting measurements with extremely efficient classical postprocessing for all six types of QWEs.

A. How to measure sector length distributions aka Shor-Lafamme QWEs

Recall from Eq. (10) that the i -body sector length $a_i[\rho]$ of an n -qubit state ρ is defined as the normalized sum of $\text{Tr}[\rho P]^2$ over all $3^i \binom{n}{i}$ Pauli operators P with $\text{wt}(P) = i$. Thus, a brute-force approach for measuring the entire SLD $\mathbf{a}[\rho]$ is to first measure all Pauli expectation values (or just their squares) and then to compute the corresponding sums. Clearly, such an approach suffers from an exponential postprocessing cost. But even if we had infinite classical computational power, how can we obtain all $\text{Tr}[\rho P]^2$ in the first place? A naive strategy uses *classical shadows* [21–25] (unrelated to Rains’ shadow), where individual copies of ρ are measured after applying a random unitary U drawn from a suitable ensemble of readout circuits. While each such measurement enables for all $\mathbf{r} \in \mathbb{F}_2^n$ access to $\text{Tr}[\rho U^\dagger Z^{\mathbf{r}} U]$, which is a Pauli operator if U is a Clifford circuit, the classical shadows approach has several drawbacks: (i) measuring all $\text{Tr}[\rho P]^2$ to constant additive precision provably requires exponentially many samples in n [30], (ii) the readout circuits are often—but not always [108, 109]—challenging to implement reliably, and (iii) for many experimental setups, the randomized nature of classical shadows is highly undesirable in practice as updating the

readout circuit on a shot-by-shot basis can slow down experimental data acquisition by several orders of magnitude. In some regards—it circumvents issue (ii) and (iii)—a better alternative is based on single-setting informationally complete measurements. These can be realized by embedding each qubit into a ququart at the readout stage [110, 111] and enable access to $\text{Tr}[\rho P]$ for all $P \in \{I, X, Y, Z\}^{\otimes n}$ simultaneously without the need of ever altering the readout circuit. However, just as classical shadows, also single-setting informationally complete measurements fall into the paradigm of *single-copy access protocols*, which all suffer from problem (i). Two-copy Bell sampling, on the other hand, allows us to measure $\text{Tr}[\rho P]^2$ for all P up to constant error with a number of shots that is constant in n [32]. However, it was hitherto unclear if and how one can also avoid the classical postprocessing cost and under what circumstances errors on the individual $\text{Tr}[\rho P]^2$ may or may not conspire when they are added up in the SLD. As we show now, the exponential postprocessing cost can always be avoided. Later in Sec. VB, we will turn back to the more subtle issue about sample complexity.

Consider the $2n$ -qubit observable

$$W_i = \frac{1}{2^n} \sum_{\substack{P \in \{I, X, Y, Z\}^{\otimes n} \\ \text{wt}(P)=i}} P \otimes P. \quad (57)$$

Since $\text{Tr}[(\rho \otimes \rho)(P \otimes P)] = \text{Tr}[\rho P]^2$, we can reinterpret the entries in the SLD $\mathbf{a}[\rho] = (a_i[\rho])_{i=0}^n$ from Eq. (10) as two-copy expectation values

$$a_i[\rho] = \text{Tr}[(\rho \otimes \rho)W_i]. \quad (58)$$

Inserting two identity operators, $\mathbb{1} = \sum_{\alpha} |\alpha\rangle\langle\alpha|$, in the basis of Bell pairs $|\alpha\rangle$ from Eq. (54) yields

$$a_i[\rho] = \sum_{\alpha, \alpha' \in \{\Phi^\pm, \Psi^\pm\}^n} \langle\alpha|W_i|\alpha'\rangle \langle\alpha'|(\rho \otimes \rho)|\alpha\rangle. \quad (59)$$

To compute the matrix entries $\langle\alpha|W_i|\alpha'\rangle$, we exploit that the SWAP operator has the Pauli decomposition

$$\text{SWAP} = \frac{1}{2} (I \otimes I + X \otimes X + Y \otimes Y + Z \otimes Z). \quad (60)$$

After a little algebra, we find

$$W_i = \frac{1}{2^{n-i}} \sum_{\substack{S \subseteq \{1, \dots, n\} \\ |S|=i}} \prod_{s \in S} \left(\text{SWAP}_{s, n+s} - \frac{1}{2} \right). \quad (61)$$

Since all expressions of the form $\langle\alpha| \text{SWAP}_{s, n+s} |\alpha'\rangle$ and $\langle\alpha| - \frac{1}{2} |\alpha'\rangle$ with $\alpha \neq \alpha'$ vanish, the operator W_i is diagonal in the basis of Bell pairs. This already shows that it must be possible to infer the expectation value $a_i[\rho] = \text{Tr}[(\rho \otimes \rho)W_i]$ via two-copy Bell sampling [34]. To see how this can be efficiently achieved in practice, we make use of elementary combinatorics: since we have i factors in each of the $\binom{n}{i}$ terms in Eq. (61), there is the possibility that exactly $l \in \{1, \dots, i\}$ of the SWAP gates hit some of the $\text{sing}(\alpha)$ singlet pairs while the

remaining ones hit exactly $i - l$ triplets. Hereby, ‘hit’ means that a singlet and a SWAP gate both have non-trivial support on a fixed subsystem S . Because

$$\langle\alpha| \text{SWAP}_{s, n+s} - \frac{1}{2} |\alpha\rangle = \begin{cases} -\frac{3}{2} & \text{if } |\alpha_s\rangle = |\Psi^-\rangle \\ +\frac{1}{2} & \text{otherwise,} \end{cases} \quad (62)$$

each such term contributes

$$\langle\alpha| \prod_{s \in S} \left(\text{SWAP}_{s, n+s} - \frac{1}{2} \right) |\alpha\rangle = \left(\frac{-3}{2} \right)^l \left(\frac{+1}{2} \right)^{i-l} \quad (63)$$

and since there are $\binom{\text{sing}(\alpha)}{l} \binom{n - \text{sing}(\alpha)}{i-l}$ possibilities for this to happen, we find the eigenvalue

$$\langle\alpha| W_i |\alpha\rangle = \sum_{l=0}^i \binom{\text{sing}(\alpha)}{l} \binom{n - \text{sing}(\alpha)}{i-l} \frac{(-3)^l}{2^n}. \quad (64)$$

This discussion shows that we can define an unbiased single-shot estimator $\hat{\mathbf{a}} = (\hat{a}_i)_{i=0}^n$ for the SLD as follows: perform a two-copy Bell measurement, record the outcome $\alpha \in \{\Phi^\pm, \Psi^\pm\}^n$, and declare $\hat{a}_i = \langle\alpha|W_i|\alpha\rangle$ for every $i \in \{0, \dots, n\}$. Further applying the transforms from Fig. 1, we obtain single-shot estimators for all six vectors of QWEs, e.g., $\hat{\mathbf{b}} = M\hat{\mathbf{a}}$ and $\hat{\mathbf{a}}' = T'\hat{\mathbf{a}}$ for the dual SLD $\mathbf{b}[\rho]$ and the APD $\mathbf{a}'[\rho]$, respectively. Since $\langle\alpha|W_i|\alpha\rangle$ only depends on the number of singlets in $|\alpha\rangle$, there are $6(n+1)$ elements of \mathbb{R}^{n+1} that the vector-valued estimators $\hat{\mathbf{a}}, \hat{\mathbf{b}}, \hat{\mathbf{a}}', \hat{\mathbf{b}}', \hat{\hat{\mathbf{a}}}', \hat{\hat{\mathbf{b}}}'$ may assume. To support future experiments, we implement open-access functionalities to compute these vectors [112]. For example, for $n = 1000$ qubits per copy, precomputing all $6(n+1)$ single-shot estimators requires less than three seconds on a standard laptop. In all six cases, our results reduce the naive classical processing cost from exponential to $O(n^2)$, see App. B.

Sample complexity, on the other hand, is an entirely different issue. Since $\langle\alpha|W_i|\alpha\rangle$ takes exponentially large positive and negative values, estimating SLDs by averaging over many realizations of $\hat{\mathbf{a}}$ sometimes suffers from cancellation effects which amplify statistical errors, see Sec. VB for details. This challenge seems to be inherent to SLDs as all known protocols for measuring them have an exponential sample complexity in the worst case (also see Sec. VC for a related discussion). Nonetheless, our protocol at least has the practical advantage of being single-setting: in contrast to randomized protocols, we do not need to update the experiment on a shot-by-shot basis. To conclude, our findings extend the experimental accessibility to SLDs from the very small to larger system sizes.

B. How to measure averaged purity distributions aka Rains’ unitary QWEs

In the previous subsection, we have identified a single-shot estimator for the APD $\mathbf{a}'[\rho]$ of an n -qubit state ρ that can be efficiently (but not yet accurately) computed. This in itself is already surprising, as averaging all subsystem purities of

a given size naively requires evaluating a sum over exponentially many terms. As we show next, for APDs the accuracy issue can also be resolved, thus paving the way for measuring them in large-scale experiments. The idea is to directly compute the single-shot estimator \hat{a}' from the two-copy Bell measurement outcome $\alpha \in \{\Phi^\pm, \Psi^\pm\}^n$ instead of detouring through the SLD, where errors could get amplified. To this end, we introduce a second $2n$ -qubit observable

$$W'_i = \frac{1}{\binom{n}{i}} \sum_{\substack{S \subseteq \{1, \dots, n\} \\ |S|=i}} \prod_{s \in S} \text{SWAP}_{s, n+s} \quad (65)$$

for all $i \in \{0, \dots, n\}$. Leveraging the SWAP trick, we find

$$\text{Tr}[\rho_S^2] = \text{Tr} \left[(\rho \otimes \rho) \prod_{s \in S} \text{SWAP}_{s, n+s} \right] \quad (66)$$

for every $S \subseteq \{1, \dots, n\}$, and averaging over all such subsystems of a given size $|S| = i$ allows us to write the APD of ρ [Eq. (28)] as

$$a'_i[\rho] = \text{Tr}[(\rho \otimes \rho) W'_i]. \quad (67)$$

As in the case of SLDs [Eq. (64)], W'_i is diagonal in the basis of Bell pairs and its eigenvalues are given by

$$\langle \alpha | W'_i | \alpha \rangle = \sum_{l=0}^i \binom{\text{sing}(\alpha)}{l} \binom{n - \text{sing}(\alpha)}{i-l} \frac{(-1)^l}{\binom{n}{i}}. \quad (68)$$

Hence, we can repeat the previous strategy and compute the already-defined single-shot estimator $\hat{a}' = T' \hat{a}$ as follows: perform a Bell measurement on $\rho \otimes \rho$ and compute $\hat{a}'_i = \langle \alpha | W'_i | \alpha \rangle$ from the $\alpha \in \{\Phi^\pm, \Psi^\pm\}^n$. By Vandermonde's identity [113], Eq. (68) only takes values in the interval $[-1, 1]$. Thus, statistical errors are no longer unfavorably amplified. We defer formal proofs on efficiency and robustness of measuring APDs to Sec. V. In particular, we will show in Thm. 8 that the sample complexity of measuring any entry of the APD is independent of n .

C. Rains' shadow QWEs are triplet probabilities

To complete the analogy between SLDs, APDs, and Rains' shadow QWEs, we should look for a third $2n$ -qubit observable \tilde{W}_i whose two-copy expectation value equals the latter. The solution is surprisingly simple and constitutes our main theoretical discovery.

Theorem 3 (Physical interpretation of Rains' shadow QWEs) *Let ρ be an n -qubit state and $\tilde{\mathbf{a}}[\rho] = (\tilde{a}_i[\rho])_{i=0}^n$ its vector of Rains' shadow QWEs from Eq. (37). For all $i \in \{0, \dots, n\}$, we have*

$$\tilde{a}_i[\rho] = \text{Tr} \left[(\rho \otimes \rho) \tilde{W}_i \right] \quad (69)$$

where we denote the projector onto the i -triplet subspace by

$$\tilde{W}_i = \sum_{\substack{\alpha \in \{\Phi^\pm, \Psi^\pm\}^n \\ \text{sing}(\alpha) = n-i}} |\alpha\rangle \langle \alpha|. \quad (70)$$

In other words, the i -th Rains' shadow QWE of ρ carries the interpretation of the probability for observing a fixed number of i triplets in a Bell sampling experiment on $\rho \otimes \rho$.

Corollary 4 (Physical origin of Rains' shadow inequalities) *For every n -qubit state ρ and all $i \in \{0, \dots, n\}$, we have*

$$\tilde{a}_i[\rho] \geq 0, \quad (71)$$

and the bound $d \leq \frac{n}{3} + 2$ for arbitrary $[[n, k, d]]$ QECCs follows from Thm. 15 in Ref. [54].

Proof: Probabilities cannot be negative. \square

Proof of Thm. 3: Denote by $\mathbf{t}[\rho] = (t_j[\rho])_{j=0}^n$ the triplet probability distribution of ρ , where

$$t_j[\rho] = \sum_{\substack{\alpha \in \{\Phi^\pm, \Psi^\pm\}^n \\ \text{sing}(\alpha) = n-j}} \langle \alpha | (\rho \otimes \rho) | \alpha \rangle. \quad (72)$$

We have to show $\tilde{\mathbf{a}}[\rho] = \mathbf{t}[\rho]$. Since $\tilde{\mathbf{a}}[\rho] = \tilde{T} \mathbf{a}[\rho]$, this is equivalent to the claim $\tilde{T}^{-1} \mathbf{t}[\rho] = \mathbf{a}[\rho]$. Recall from Eq. (39) that $\tilde{T} = M M' \tilde{M} M'$ arises from M if we alternate the signs of the columns. As $M^2 = M'^2 = \tilde{M}^2 = \mathbb{1}$, the inverse $\tilde{T}^{-1} = M' \tilde{M} M M'$ similarly arises by alternating the signs of the rows of M , i.e., the matrix entries of \tilde{T}^{-1} are given by

$$\tilde{T}_{i,j}^{-1} = \frac{1}{2^n} \sum_{l=0}^n \binom{n-j}{i-l} \binom{j}{l} (-3)^{i-l}. \quad (73)$$

To prove $\tilde{T}^{-1} \mathbf{t}[\rho] = \mathbf{a}[\rho]$, we have to express $\mathbf{a}[\rho]$ in terms of triplet probabilities. Fortunately, the term $\langle \alpha | W_i | \alpha \rangle$ in Eq. (64) only depends on the number $j = n - \text{sing}(\alpha)$ of triplets in α . This means that we can split up the sum and separate terms. Expanding Eq. (59) yields

$$\begin{aligned} a_i[\rho] &= \sum_{j=0}^n \sum_{\substack{\alpha \in \{\Phi^\pm, \Psi^\pm\}^n \\ \text{sing}(\alpha) = n-j}} \langle \alpha | W_i | \alpha \rangle \langle \alpha | (\rho \otimes \rho) | \alpha \rangle \\ &= \sum_{j,l=0}^n \binom{n-j}{l} \binom{j}{i-l} \frac{(-3)^l}{2^n} t_j[\rho]. \end{aligned} \quad (74)$$

Since the summand in Eq. (74) is zero for $l > i$, we can exchange the order and write instead $l \mapsto i-l$, obtaining

$$a_i[\rho] = \frac{1}{2^n} \sum_{j,l=0}^n \binom{n-j}{i-l} \binom{j}{l} (-3)^{i-l} t_j[\rho]. \quad (75)$$

Thus, we have $\mathbf{a}[\rho] = \tilde{T}^{-1} \mathbf{t}[\rho]$, which completes the proof. \square

Now that we have established a mathematically precise connection between the physics of two-copy Bell sampling

experiments and the powerful machinery of QWEs, we are in the convenient position to transfer valuable ideas from one paradigm to the other. For example, well-known bounds on sector lengths [77] translate into bounds on triplet probabilities, as discussed in App. D. There, we derive results of the following sort:

Corollary 5 (Lower bound on the average number of triplets) *Let ρ be an n -qubit state and $(\tilde{a}_x[\rho])_{x=0}^n$ its shadow QWEs. The average number of triplets obtained in a two-copy Bell sampling experiment can be bounded as*

$$\frac{3n}{4} \leq \sum_{x=0}^n \tilde{a}_x[\rho] x \leq n, \quad (76)$$

and these bounds are tight.

Proof: See App. D 2. \square

In light of Sec. II and Thm. 3, it now becomes clear how one can measure QWEs of QECCs in experiments: first, prepare two copies of the maximally mixed logical state ρ_{QECC} [Eq. (1)] and perform pairwise Bell measurements as in Fig. 2 above. Then, either (i) estimate the QWEs directly from the Bell samples using the single-shot estimators from Secs. III A and III B or, equivalently, (ii) estimate the TPD $\tilde{\mathbf{a}}[\rho_{\text{QECC}}]$ and then apply the transforms from Fig. 1 to obtain estimators of $\mathbf{a}[\rho_{\text{QECC}}] = \tilde{T}^{-1}\tilde{\mathbf{a}}[\rho_{\text{QECC}}]$ and $\mathbf{a}'[\rho_{\text{QECC}}] = \tilde{T}'^{-1}\tilde{\mathbf{a}}[\rho_{\text{QECC}}]$.

D. QWEs and entanglement

The idea to quantify entanglement via QWEs is not new. Already in Ref. [114], it was shown that from SLDs it is possible to compute generalized Meyer-Wallach entanglement measures (which are conceptually the same as APDs). In this section, we leverage our insights about the physical interpretation of Rains' shadow QWEs (Thm. 3) to strengthen this connection. More precisely, we discuss important entanglement measures that can be defined in terms of triplet probabilities and, hence, efficiently computed whenever the SLD is analytically available.

A direct consequence of Thm. 3 is that Rains' shadow QWEs [Eq. (37)] of an n -qubit state ρ can be written as

$$\tilde{a}_i[\rho] = \sum_{\substack{\alpha \in \{\Phi^\pm, \Psi^\pm\}^n \\ \text{sing}(\alpha) = n-i}} \langle \alpha | (\rho \otimes \rho) | \alpha \rangle. \quad (77)$$

Hence, it makes sense to refer to $\tilde{\mathbf{a}}[\rho] = (\tilde{a}_i[\rho])_{i=0}^n$ as the *triplet probability distribution* (TPD) of ρ . By applying the linear maps from Fig. 1, it is possible to extract useful properties from TPDs. For example, the final row of the vector equation $\mathbf{a}'[\rho] = \tilde{T}'^{-1}\tilde{\mathbf{a}}[\rho]$ reads

$$\text{Tr}[\rho^2] = a'_n[\rho] = \sum_{j=0}^n (-1)^j \tilde{a}_{n-j}[\rho], \quad (78)$$

which is a condensed version of Eq. (56). Conversely, the final row of $\tilde{\mathbf{a}}[\rho] = \tilde{T}'\mathbf{a}'[\rho]$ is equivalent to

$$\tilde{a}_n[\rho] = \frac{1}{2^n} \sum_{i=0}^n \binom{n}{i} a'_i[\rho] = \frac{1}{2^n} \sum_{S \subseteq \{1, \dots, n\}} \text{Tr}[\rho_S^2]. \quad (79)$$

In other words, the probability for obtaining n triplets (zero singlets) is equal to the average over all subsystem purities. Thus, $\tilde{a}_n[\rho] < 1$ implies that at least one of the marginals of ρ (including ρ itself) cannot be pure. Conversely, every pure state Ψ with

$$1 - \tilde{a}_n[\Psi] > 0 \quad (80)$$

must be entangled. Therefore, the quantity

$$C[\Psi] = 1 - \tilde{a}_n[\Psi] \quad (81)$$

is of central importance.

A few historical comments are in order. Originally, $C[\Psi]$ was studied under the name *concurrence* in the modified form $2\sqrt{C[\Psi]}$ [101–104]. Recently, concurrences have regained some attention [115–118] in the form of Eq. (81). We also prefer this version of the concurrence as it avoids superfluous notation and, thus, can be read off directly from the TPD. For these reasons, in this work, the term concurrence will henceforth always refer to Eq. (81).

Via convex roof extension, it is possible to generalize this concept to the case where ρ is an arbitrary mixed state [104]. While the resulting concurrence $C[\rho]$ is in general difficult to compute, it can always be lower bounded via [104, 117]

$$C[\rho] \geq \frac{1}{2^n} + \left(1 - \frac{1}{2^n}\right) \text{Tr}[\rho^2] - \tilde{a}_n[\rho]. \quad (82)$$

In combination with the QWE machinery, this bound is extremely powerful, as we will show later in Sec. VI. Indeed, provided we know the SLD $\mathbf{a}[\Psi]$ of a pure state Ψ , Eq. (15) yields the SLD of the locally-depolarized state $\rho = \mathcal{E}_p^{\otimes n}[\Psi]$. This, in turn, determines $\text{Tr}[\rho^2] = \sum_i a_i[\rho]$ as well as the all-triplet (zero-singlet) probability

$$\tilde{a}_n[\rho] = \frac{1}{2^n} \sum_{i=0}^n 3^{n-i} a_i[\rho], \quad (83)$$

which is all we need to evaluate the bound in Ineq. (82).

Note that Eq. (83) is the final entry of $\tilde{\mathbf{a}}[\rho] = \tilde{T}\mathbf{a}[\rho]$. The first row of the same equation allows us to compute the zero-triplet (all-singlet) probability

$$\tilde{a}_0[\rho] = \frac{1}{2^n} \sum_{i=0}^n (-1)^i a_i[\rho] \quad (84)$$

from the SLD of ρ . A different expression for this probability is obtained by inserting $i = 0$ into the original definition of Rains' shadow QWEs [Eq. (37)],

$$\tilde{a}_0[\Psi] = \frac{1}{2^n} \text{Tr}[\Psi\tilde{\Psi}]. \quad (85)$$

Note that $\text{Tr}[\Psi\tilde{\Psi}] = 2^n \tilde{a}_0[\Psi]$ is also an entanglement measure known as the n -tangle [96]. In terms of subsystem purities, it can be expressed as

$$\begin{aligned} \tilde{a}_0[\rho] &= \frac{1}{2^n} \sum_{i=0}^n (-1)^i \binom{n}{i} a'_i[\rho] \\ &= \frac{1}{2^n} \sum_{S \subseteq \{1, \dots, n\}} (-1)^{|S|} \text{Tr}[\rho_S^2]. \end{aligned} \quad (86)$$

To summarize, the two endpoints of the TPD $\tilde{\mathbf{a}}[\Psi]$ of a pure state Ψ directly correspond to two important entanglement measures: concurrence $C[\Psi]$ and n -tangle $\text{Tr}[\Psi\tilde{\Psi}]$. In particular, both of them follow from the SLD $\mathbf{a}[\Psi]$. While the concurrence lends itself to an entanglement detection protocol with an efficient sample complexity [104], the opposite is true about the n -tangle. Being an overlap between two pure states, $\text{Tr}[\Psi\tilde{\Psi}]$ is upper bounded by 1. Therefore, the zero-triplet probability $\tilde{a}_0[\Psi]$ is exponentially small by Eq. (85), which implies that exponentially many samples are required to resolve $\text{Tr}[\Psi\tilde{\Psi}]$ up to constant additive error [119]. Nevertheless, concurrence and n -tangle are useful notions as they quantify *how much* a given state is entangled, thus complementing the n -body sector length criterion [Eq. (14)] and the purity criterion [Eq. (32)], which certify *that* a given state is entangled.

Finally, let us remark that—for small qubit numbers—QWEs are strong enough to detect multipartite entanglement. For example, every 3-qubit state ρ and every 4-qubit state σ with $a_3[\rho] > 3/8$ and $a_3[\sigma] > 7/16$, respectively, must be genuinely multipartite entangled [77].

IV. EXPERIMENTAL DEMONSTRATIONS

We have now reviewed the theoretical machinery of QWEs in Sec. II and established a strong connection to Bell sampling in Sec. III by identifying collections of $2n$ -qubit observables (and showing they are diagonal in the basis of Bell pairs) for measuring QWEs. Having available these definitions is what will enable us in Sec. V to derive rigorous performance guarantees. Before that, however, we want to put the theory built so far to the ultimate test and implement experiments on a state-of-the-art quantum processor.

Two-copy Bell sampling has the following experimental requirements: (i) since we need to prepare two approximate (see Thm. 7 below) copies of the same state in two quantum registers, it is beneficial to work with an experimental platform for which physical parameters exhibit little to no variation between the qubits; (ii) considering that the two registers eventually need to be read out via pairwise Bell measurements, we also require a certain degree of connectivity. For example, if we wanted n linearly connected qubits at the preparation stage, we would overall require at least a $2 \times n$ rectangular connectivity. Both requirements are met by all-to-all connected trapped-ion quantum computers.

In this section, we report experimental demonstrations of single-setting QWE measurements carried out on our trapped-ion quantum processor, as described in Ref. [120]. We trap

sixteen $^{40}\text{Ca}^+$ ions in a macroscopic linear Paul trap, where the electronic states are controlled via laser pulses. Each ion encodes one qubit into the electronic Zeeman levels $|0\rangle = |4^2S_{1/2}, m_J = -1/2\rangle$ and $|1\rangle = |3^2D_{5/2}, m_J = -1/2\rangle$, which are connected via an optical quadrupole transition at a wavelength of 729 nm. Coulomb interaction between the ions gives rise to collective motional modes, which are used to mediate entangling operations between any desired pair of qubits. Single ion addressing with 729 nm light allows for arbitrary single- and two-qubit operations. The native gate set consists of arbitrary physical rotations around the x - and y -axis of the Bloch sphere and virtual rotations [121] around the z -axis for single-qubit operations, as well as the maximally entangling two-qubit Mølmer-Sørensen gate $\exp(i\frac{\pi}{4}X \otimes X)$ [122]. The latter is equivalent to a CNOT gate up to local rotations [123].

We begin by presenting experimental results on a variety of six-qubit states in Sec. IV A, before reporting a proof-of-principle demonstration of the direct measurement of QWEs of QECCs in Sec. IV B.

A. Direct measurement of QWEs for states

For our first experiment, we separate the sixteen ions into three groups with different purposes. On each end of the linear trap, we devote six ions to host one copy of a quantum state ρ that is our approximate experimental realization of a pure target state Ψ on $n = 6$ qubits. The remaining four ions in the center of the chain serve as a buffer zone to suppress the effect of laser fields leaking from one copy to the other. We prepare six different states that exhibit various features of entanglement, and directly measure their triplet probability distribution (TPD) in the two-copy Bell sampling experiment from Fig. 2. The measured TPDs (blue and yellow) are plotted in the bottom panel of Fig. 3. Recall from Thm. 3 that the TPD is equal to the distribution $\tilde{\mathbf{a}}[\rho]$ of Rains' shadow QWEs. Hence (recall Fig. 1), we can transform the measured TPDs into Shor-Laflamme QWEs $\mathbf{a}[\rho] = \tilde{T}^{-1}\tilde{\mathbf{a}}[\rho]$ (pink) and into Rains' unitary QWEs $\mathbf{a}'[\rho] = \tilde{T}'^{-1}\tilde{\mathbf{a}}[\rho]$ (green), which are plotted in the top and central panel of Fig. 3, respectively.

In addition to the raw experimental data (red dots), we also present in Fig. 3 error-mitigated results (green dots) obtained from the following heuristic strategy. The goal is to effectively remove errors from the Bell measurement circuit, which mainly suffers from noisy CNOT gates. For our first target state, $\Psi_1 = |0\rangle\langle 0|^{\otimes 6}$, we can neglect preparation errors. Thus, we can use its measured QWEs to calibrate those of the other states by exploiting an insight about Shor-Laflamme aka sector length distribution (SLDs): the local depolarizing noise channel acts diagonally on SLDs in the sense that all i -body sector lengths $a_i[\rho]$ are individually reduced while different-body sector lengths do not interfere with each other [Eq. (15)]. Heuristically assuming that the effective noise channel (that arises when all error channels in the Bell measurement circuit are backpropagated onto the measured states) is well-approximated by an error channel with this property (diagonal

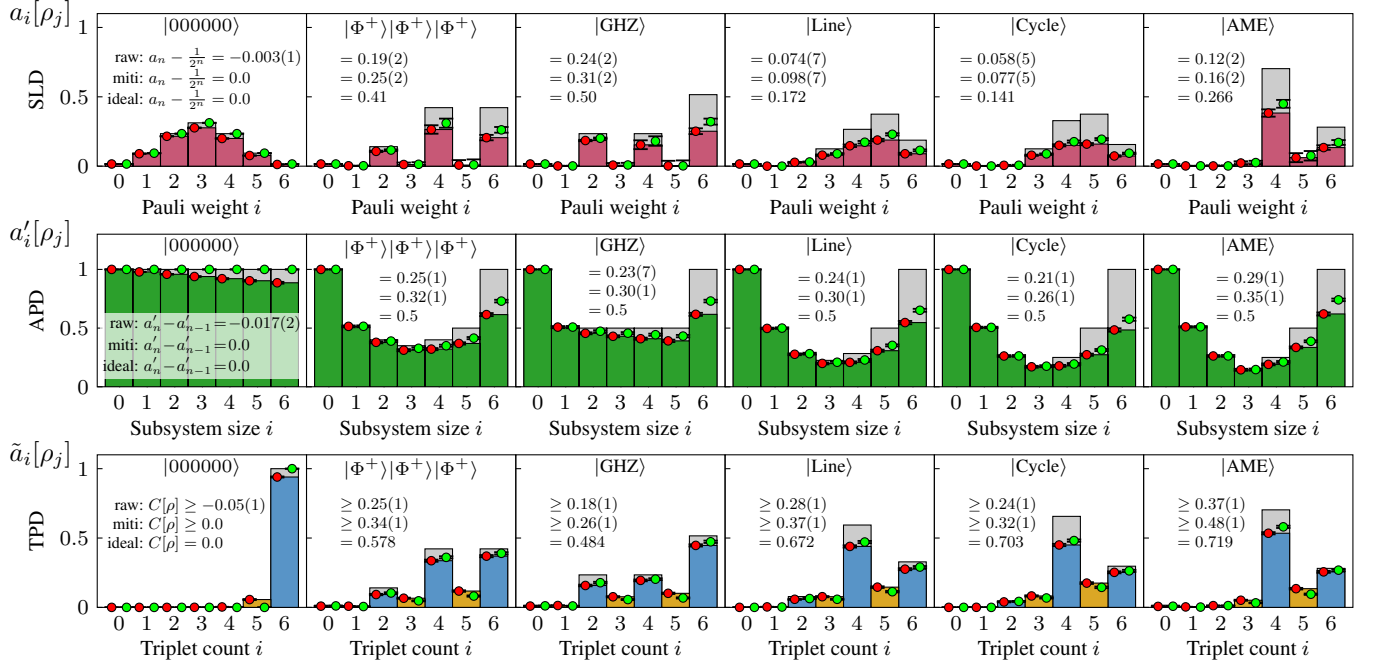


FIG. 3. Experimentally measured QWEs for six different states ρ_j on $n = 6$ trapped-ion qubits per copy. From 10,000 two-copy Bell samples per state, we simultaneously estimate the SLD (top), APD (center), and TPD (bottom). Respectively, these carry the interpretation of contribution to the purity [Eq. (12)], the averaged purity [Eq. (28)], and the observed triplet probability estimates [Eq. (77)]. In the TPD picture, we distinguish bins of even (blue) and odd (yellow) singlet numbers to highlight their positive and negative impact, respectively, on the global purity $\text{Tr}[\rho_j^2]$. Bootstrapped error bars show 95% confidence intervals. Insets show quantities whose positivity certifies entanglement by the n -body sector length criterion (top), purity criterion (center), and concurrence criterion (bottom), where “raw”, “miti”, and “ideal” refer to raw experimental (dark red dots), Bell readout error mitigated experimental (bright green dots), and ideal theoretical values (gray background), respectively. For all criteria and all states (except for the first), entanglement is experimentally verified.

SLD action), we define damping factors $\lambda_1, \dots, \lambda_n$ via [124]

$$a_i^{\text{raw}}[\rho_1] = \lambda_i a_i[\Psi_1] = \frac{\lambda_i}{2^n} \binom{n}{i}. \quad (87)$$

In our readout error mitigation strategy, we reuse the same damping factors λ_i to define the mitigated SLD via

$$a_i^{\text{miti}}[\rho_j] = \lambda_i^{-1} a_i^{\text{raw}}[\rho_j] \quad (88)$$

for all states ρ_j under investigation. By definition, we thus have $\mathbf{a}^{\text{miti}}[\rho_1] = \mathbf{a}[\Psi_1]$. For the other states, we generally observe $a_i^{\text{raw}}[\rho_j] \leq a_i^{\text{miti}}[\rho_j] \leq a_i[\Psi_j]$. Further applying the transforms T' and \tilde{T} from Fig. 1 to $\mathbf{a}^{\text{miti}}[\rho_j]$, we also obtain mitigated values for the other two sets of QWEs [125].

Let us describe the six states whose measured QWEs are displayed in Fig. 3. As a digital feature, we additionally link the definitions below to `GraphStateVis` [79], where the corresponding states and their SLDs are visualized [126]. Again, $\Psi_1 = |0\rangle\langle 0|^{\otimes 6}$ is a pure product state without any entanglement. Second, $\Psi_2 = |\Phi^+\rangle\langle \Phi^+|^{\otimes 3}$ is the state of three maximally entangled two-qubit Bell pairs without entanglement between the pairs. All other target states are *genuinely multipartite entangled* (GME). First, the projector Ψ_3 onto $|\text{GHZ}\rangle = \frac{1}{\sqrt{2}}(|0\rangle^{\otimes 6} + |1\rangle^{\otimes 6})$, followed by Ψ_4 and Ψ_5 which

project onto the *graph state* [127] vectors

$$|\text{Line}\rangle = \text{CZ}_{1,2}\text{CZ}_{2,3}\text{CZ}_{3,4}\text{CZ}_{4,5}\text{CZ}_{5,6} |+\rangle^{\otimes 6} \text{ and } \quad (89)$$

$$|\text{Cycle}\rangle = \text{CZ}_{1,2}\text{CZ}_{2,3}\text{CZ}_{3,4}\text{CZ}_{4,5}\text{CZ}_{5,6}\text{CZ}_{6,1} |+\rangle^{\otimes 6}, \quad (90)$$

respectively, where $|+\rangle = \frac{1}{\sqrt{2}}(|0\rangle + |1\rangle)$ and $\text{CZ}_{i,j}$ is the controlled-Z gate between qubit i and j . Finally, we construct a new circuit (App. E) requiring only seven CNOT gates for preparing an *absolutely maximally entangled* (AME) six-qubit state $\Psi_6 = |\text{AME}\rangle\langle \text{AME}|$ [128].

All states from above are stabilizer states. Therefore, their i -body sector length [Eq. (10)] not only is interpretable as a term contributing to the purity [Eq. (12)], but also as the (normalized) number of weight- i stabilizer operators [Eq. (20)]. For Ψ_1 , whose stabilizer group is $\{Z^{r_1} \otimes \dots \otimes Z^{r_n} \mid \mathbf{r} \in \mathbb{F}_2^n\}$, we thus expect a symmetrical binomial distribution [Eq. (13)], which is in very good agreement with raw experimental observations in Fig. 3 (top left panel). For the remaining five states, we find experimental SLDs (pink) revealing various expected entanglement features despite noticeable amounts of noise. For all measured states, the n -body sector length criterion [Eq. (14)] certifies the presence of entanglement. More precisely, the difference $a_6[\rho_j] - 2^{-6}$ (SLD insets) is strictly positive. The theoretical maximum, $a_6[\Psi_3] - 2^{-6} = 0.5$, is attained by the ideal GHZ state [78]. Also in our ex-

periment, we observe that the GHZ state has the largest n -body sector length $a_6^{\text{miti}}[\rho_3] = 0.32(2)$ among all measured states. We find it is closely followed by the three Bell pairs for which $a_6^{\text{miti}}[\rho_2] = 0.26(2)$. As Ψ_2 is clearly triseparable, care should be taken when relating $a_n[\rho]$ to multipartite entanglement [129]. A more holistic analysis of QWE features can help. For example, recall that a pure state Ψ is called m -uniform iff $a_i[\Psi] = 0$ for all $1 \leq i \leq m$. Such is impossible if Ψ has a pure marginal of size m (which would be necessarily unentangled with its complement, e.g., Ψ_2 is not 2-uniform) and negating this statement shows in which sense m -uniformity can be interpreted as an extremal form of multipartite quantum entanglement. In the design of our experiment, we have selected states of increasing levels of multipartite entanglement as measured by m -uniformity: Ψ_1 is 0-uniform, Ψ_2, Ψ_3, Ψ_4 are 1-uniform, Ψ_5 is 2-uniform, and Ψ_6 is 3-uniform. Our experimental results confirm that $a_i[\rho_j]$ almost vanishes for the predicted combinations of i, j . Therefore, we can largely rule out systematic errors that generate few-body Pauli correlations, which are expected to be absent. Moreover, we generally observe $a_i[\rho_j] \leq a_i[\Psi_j]$ in Fig. 3, also when $a_i[\Psi_j]$ is non-zero. This provides further diagnostic information about the error mechanisms in the reported experiment as coherent overrotations in the preparation circuit and purifying noise, e.g., the amplitude damping channel [98], could increase $a_i[\rho]$. Since we do not see any such effects, we attribute the noise affecting our states to entropy-increasing errors primarily.

Let us segue to a discussion about averaged purity distributions (APDs), $\mathbf{a}'[\rho]$, [Eq. (28)], by pointing out again that the global purity $\text{Tr}[\rho_j^2]$ arises in all three pictures: it is the sum [Eq. (12)] of all sector lengths (pink), the rightmost entry [Eq. (28)] of the APD (green), and the alternating sum [Eq. (78)] of triplet probabilities (blue for positive, yellow for negative). In the APD picture, the hallmark of entanglement [Eq. (32)] is an increase of $a'_i[\rho_j]$ with i , which is clearly observed at the right of the APD for all entangled states. As expected, we see in Fig. 3 that the averaged purity $a'_i[\rho_1]$ of the unentangled product state monotonically decreases with the subsystem size i . The purity criterion [Eq. (32)] can be quantified as well: in the APD inset of Fig. 3, we show the measured values of the purity difference $a'_6[\rho_j] - a'_5[\rho_j]$. As with $a_n[\rho] - 2^{-n}$ above, here a positive value of the purity difference certifies entanglement. In all cases (except for Ψ_1 of course), we would ideally expect $a'_6[\Psi_j] - a'_5[\Psi_j] = 0.5$ (which is simultaneously the theoretical maximum), however, we observe (raw) values between 0.211(6) for Ψ_5 and 0.285(5) for Ψ_6 . In other words, the purity criterion clearly detects entanglement in ρ_2, \dots, ρ_6 despite significant noise levels. Readout error mitigation further boosts these purity differences by about 22%–32% as shown in the APD inset of Fig. 3. We can also see that—on average—the marginals of the AME state are (as expected) more mixed than for lesser-entangled states such as the GHZ state, e.g., by looking at $a'_3[\rho_j]$. Note that measuring APDs (in contrast to SLDs) is always scalable, see Thm. 7 and Thm. 8 below.

Finally, consider the TPDs [Eq. (77)] that are shown in the bottom panel of Fig. 3. Among the three QWEs, TPDs can

be most straightforwardly extracted from Bell samples simply by counting triplets. By Thm. 3, TPDs are the same as Rain’s shadow QWEs [Eq. (37)] and, in accordance with Cor. 5, we observe in Fig. 3 that all measured TPDs concentrate towards larger triplet numbers. Overall, we observe fair experimental agreement with theoretical predictions (gray/yellow bars for values that are smaller/larger than expected).

Let us start our discussion of the TPDs with the all-triplet probability $\tilde{a}_n[\rho]$. For pure product states, we would never find any singlets, i.e., $\tilde{a}_6[\Psi_1] = 1$. This prediction is closely matched by our experimental observation $\tilde{a}_6^{\text{raw}}[\rho_1] = 0.94(1)$. Moreover, Fig. 3 reveals that almost all of what is missing from $\tilde{a}_6^{\text{raw}}[\rho_1]$ has leaked into $\tilde{a}_5^{\text{raw}}[\rho_1] = 0.06(1)$, where just one singlet was measured. The difference between even-singlet (blue) and odd-singlet (yellow) probabilities [Eq. (78)] equals the global purity $\text{Tr}[\rho^2] = a'_n[\rho]$. In particular, we find $a'_6^{\text{raw}}[\rho_1] = 0.89(1)$, where “raw” again refers to the fact that readout errors (mainly due to CNOTs) are mathematically included as noise on the state ρ_1 . Recall that $a_6^{\text{miti}}[\rho_1] = \tilde{a}_6^{\text{miti}}[\rho_1] = 1$ as our heuristic error mitigation strategy completely removes all noise from ρ_1 by definition.

For the other (entangled) states, we see that the all-triplet probability $\tilde{a}_6^{\text{miti}}[\rho_j]$ remains slightly below each respective value of $\tilde{a}_6[\Psi_j]$. In general, any value of $\tilde{a}_n[\rho]$ below unity is intimately linked to a loss of purity of a state ρ , its marginals, or both [Eq. (79)]. Then, the probability missing in $\tilde{a}_n[\rho]$ must reappear in some of the $\tilde{a}_i[\rho]$ ’s, which correspond to either an even or odd number of singlets. Whenever the number of singlets is even (and positive), we can conclude the existence of mixed marginals [Eq. (79)] that cannot be traced back to losses of global purity [Eq. (78)]. In other words, Bell samples with an even (non-zero) number of singlets (blue) are the hallmark of entanglement in the TPD picture. On the other hand, measurement outcomes with an odd number of singlets (yellow) always stem from mixedness [Eq. (78)]. Both effects are simultaneously captured in the lower bound [Ineq. (82)] on the concurrence $C[\rho]$, see TPD inset of Fig. 3.

Among the entangled states studied here, the GHZ state has the smallest ideal concurrence $C[\Psi_3] = 0.484(1)$. This is because, for pure states Ψ , the concurrence $C[\Psi] = 1 - \tilde{a}_n[\Psi]$ equals one minus the weighted sum over the APD [Eq. (79)] and—for the GHZ state Ψ_3 —the APD has comparatively large entries (because all nontrivial marginals are mixtures of only two states). At the other extreme, the ideal AME state Ψ_6 has maximally mixed marginals and, correspondingly, the largest possible concurrence $C[\Psi_6] = 0.719(1)$. Our experimental observations qualitatively match these theoretical predictions: among the entangled states ρ_j , the experimental GHZ (AME) state minimizes (maximizes) the lower bound on $C[\rho_j]$. In particular, this shows that also the concurrence criterion is robust enough to detect entanglement in our experiment—even without error mitigation. We stress the fact that (in contrast to $a_n[\rho] - 2^{-n}$ and $a'_n[\rho] - a'_{n-1}[\rho]$) the concurrence $C[\rho]$ is an entanglement measure. In all cases, we find that Bell readout error mitigation significantly increases the measured lower bound on the concurrence.

We also see in Fig. 3 that Bell samples with zero triplets are almost never observed. This is easily explained as the corre-

sponding probability $\tilde{a}_0[\rho]$ is exponentially suppressed in the number of qubits n , which relates to the fact that $\tilde{a}_0[\rho]$ (left-most blue bar) equals the alternating weighted sum [Eq. (86)] over the APD of ρ (green). Finally, let us point out that, if our experimental states ρ_j were pure, then $\tilde{a}_0[\rho_j]$ would be (exponentially) proportional to yet another entanglement measure known as the n -tangle [Eq. (85)].

The above discussion illustrates how various entanglement properties can be read off from the three QWE distributions. For supplementary theoretical examples on how other distinct quantum features manifest themselves in QWEs, we refer the interested reader to Apps. F–G. In App. F, we elaborate on the subtle differences between coherent superpositions and incoherent mixtures whereas App. G exemplifies characteristics of various many-body states.

B. Direct measurement of QWEs for QECCs

In the previous subsection, we have experimentally investigated QWEs of pure target states. Let us next turn our attention to QECCs. As we established in Sec. III C, the QWEs of a QECC can be directly measured via Bell sampling from $\rho_{\text{QECC}}^{\otimes 2}$, where ρ_{QECC} [Eq. (1)] is the maximally mixed state within the code space. In principle, this protocol (Fig. 2) has the desirable single-setting property discussed in Sec. III A, provided one can deterministically prepare ρ_{QECC} . Alternatively, one could update the state preparation circuit on a shot-by-shot basis as $\rho_{\text{QECC}}^{\otimes 2}$ is physically indistinguishable from a uniformly at random (and independently for each copy) prepared logical computational basis state. Fortunately, this second protocol can be derandomized when the number of qubits is small. This is best explained for an $[[n, 1, d]]$ code with logical state vectors $|0\rangle_L$ and $|1\rangle_L$. Assume that the logical bit-flip gate X_L admits a transversal implementation, which is the case for all stabilizer codes [1] and some non-stabilizer codes [130]. Then, it suffices to perform Bell sampling from just two different input states, namely $|0, 0\rangle_L$ and $|0, 1\rangle_L$. Indeed, since QWEs are invariant [53] under local unitary gates such as $X_L \otimes X_L$, the TPDs arising from $|1, 1\rangle_L$ and $|1, 0\rangle_L$, respectively, ideally coincide with those from $|0, 0\rangle_L$ and $|0, 1\rangle_L$. Hence, there is no need for taking Bell samples from $|1, 1\rangle_L$ and $|1, 0\rangle_L$ [131].

We perform the described two-setting experiment for the seven-qubit color code [49, 132, 133] and present the measured QWEs and their dual QWEs in Fig. 4. The seven-qubit color code is a $[[7, 1, 3]]$ stabilizer QECC that is well explored in experiments [6, 10, 134–144]. For our purposes, it suffices to directly prepare logical states using a circuit with eight CNOT gates per copy [142] without resorting to sophisticated fault-tolerant preparation circuits [6, 142–146]. This time, we use a buffer zone of only two ions to separate the two seven-qubit copies on our trapped-ion quantum device. In all three QWE pictures, we can see in that—in contrast to Fig. 3—the target state $\rho_{\text{QECC}}^{\text{ideal}}$ is not a pure state and that our experimental realization $\rho_{\text{QECC}}^{\text{exp}}$ is even more mixed. Indeed, for a pure state, each of the three QWE distributions would have coincided—by MacWilliams’ identity—with its respective dual. This is

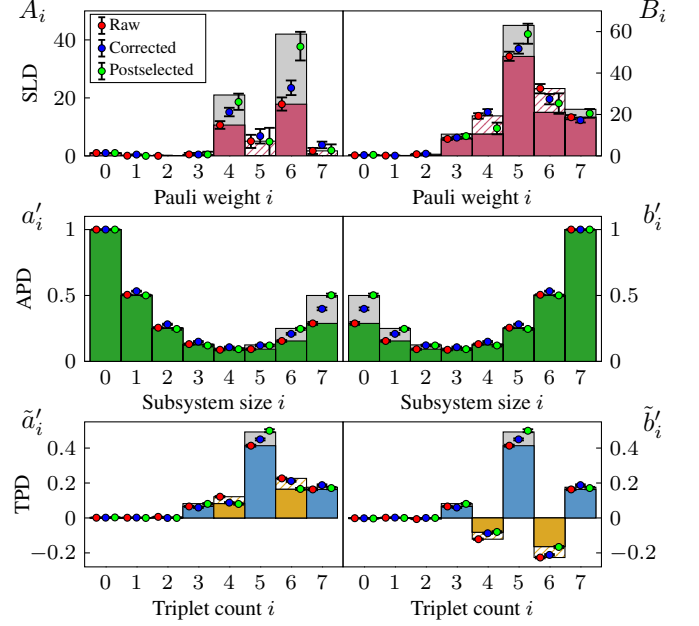


FIG. 4. Experimentally measured QWEs (left) and dual QWEs (right) of the seven-qubit color code. In total, 20,000 Bell samples are averaged over two input settings: $|0, 0\rangle_L$ and $|0, 1\rangle_L$. From this, we estimate SLD (top), APD (center), and TPD (bottom). For TPDs, we use blue (yellow) color to highlight that even (odd) singlet counts have a positive (negative) impact on the global purity. Shaded (gray) segments correspond to raw QWE values that are larger (smaller) in magnitude than in the ideal case. Besides raw data (left red dots), we also show error-corrected (centered blue dots) and postselected (right green dots) QWEs, respectively, for which Bell samples with violated parity checks are either corrected or simply discarded. Bootstrapped error bars show 95% confidence intervals. Note that, for some $[[n, k, d]]$ codes, measurements of $A_i = 2^n a_i[\rho_{\text{QECC}}]$ and $B_i = 2^{n+k} b_i[\rho_{\text{QECC}}]$ QWEs are limited to intermediate system sizes, but TPD and APD measurements are always scalable, see main text Sec. V. The organizational similarity to Fig. 1 is intentional.

clearly not the case in Fig. 4 as the distributions in the left panels do not coincide with those on the right. In quantitative terms, we can most easily read off the global purities $a'_7[\rho_{\text{QECC}}^{\text{ideal}}] = 0.5$ and $a'_7[\rho_{\text{QECC}}^{\text{exp}}] = 0.228(1)$ from the APD (green), however, the same information is contained in the SLD (pink) and TPD (blue and yellow), whose sum [Eq. (12)] and alternating sum [Eq. (78)], respectively, also yield the global purity. Since MacWilliams’ matrix M is diagonal in the TPD basis [Eq. (9)], the odd-singlet bins (yellow) are simply negated when passing to the dual TPD $\tilde{\mathbf{b}}[\rho] = M\tilde{\mathbf{a}}[\rho]$ (bottom right in Fig. 4). The fact that these bins are occupied, i.e., $\tilde{\mathbf{a}}[\rho] \neq \tilde{\mathbf{b}}[\rho]$, thus causes the aforementioned loss in $\text{Tr}[\rho^2] = \sum_{i=0}^n \tilde{b}_i[\rho]$. Similarly, since M' is the anti-diagonal matrix [Eq. (8)], the dual APD, $\mathbf{b}'[\rho] = M'\mathbf{a}'[\rho]$, is just the reversed APD. Therefore, $\mathbf{a}'[\rho] \neq \mathbf{b}'[\rho]$ implies the existence of marginals whose purity distinguishes them from their complementary marginal, which—by virtue of the Schmidt decomposition—again implies that ρ is a mixed state.

Despite being mixed (both by construction and by noise), our state $\rho = \rho_{\text{QECC}}^{\text{exp}}$ is nevertheless entangled as certified by the averaged subsystem purities $a'_3[\rho], \dots, a'_6[\rho]$, which are all clearly smaller than $a'_7[\rho]$. The maximal difference is $a'_7[\rho] - a'_4[\rho] = 0.20(2) > 0$. Also in the TPD picture, entanglement is observed as the all-triplet probability $\tilde{a}_7[\rho] = 0.163(1)$ is sufficiently small to grant a nontrivial lower bound [Ineq. (82)] on the concurrence $C[\rho] \geq 0.13(1)$ [147].

The n -body sector length criterion [Eq. (14)], however, does not reveal that ρ is entangled as $a_7[\rho] - 2^{-7} = 0.006(11)$ is not undoubtedly positive within error bars. This is to be expected as $A_i = 2^n a_i[\rho_{\text{QECC}}^{\text{ideal}}]$ (top left panel in Fig. 4) is the number of weight- i stabilizer operators—and the $[[7, 1, 3]]$ code does not have any full-weight stabilizers. In the ideal case, the Pauli weight distributions of the stabilizer group \mathcal{S} and its normalizer \mathcal{S}^\perp [Eq. (24)] are given by

$$\mathbf{A} = (1, 0, 0, 0, 21, 0, 42, 0) \quad \text{and} \quad (91)$$

$$\mathbf{B} = (1, 0, 0, 21, 21, 126, 42, 45), \quad (92)$$

respectively, from which we can read off the distance $d = 3$ of the code [Eq. (27)] as the smallest index $i > 0$ for which $A_i < B_i$. Moreover, $A_1 = A_2 = 0$ is equivalent [51] to the fact that the seven-qubit color code (in contrast to its larger cousins) is a non-degenerate QECC.

In Fig. 4, we see that the SLD results are severely impacted by errors. On the one hand, the 21 weight-4 stabilizer operators (together with all other weight-4 Pauli operators, whose expectation values ideally vanish) only actualize a total of

$$2^7 a_4[\rho_{\text{QECC}}^{\text{exp}}] = 10.6_{-1.8}^{+2.0} < 21 = 2^7 a_4[\rho_{\text{QECC}}^{\text{ideal}}] \quad (93)$$

squared Pauli expectation values. Similarly, we only find

$$2^7 a_6[\rho_{\text{QECC}}^{\text{exp}}] = 17.8_{-3.0}^{+3.4} < 42 = 2^7 a_6[\rho_{\text{QECC}}^{\text{ideal}}], \quad (94)$$

which we mainly attribute to the 42 weight-6 stabilizer operators. On the other hand, as we explain below, we observe that $2^7 a_5[\rho_{\text{QECC}}^{\text{exp}}] = 5.0_{-3.0}^{+3.4}$ and $2^7 a_7[\rho_{\text{QECC}}^{\text{exp}}] = 1.7_{-1.6}^{+1.4}$ are higher than their ideal value zero. Despite these systematic errors due to experimental imperfections—which only amplified over the transform of (dual) TPDs to (dual) SLDs—we can still correctly infer the distance $d = 3$ as well as the fact that the investigated code is non-degenerate from the raw data.

Let us point out an interesting noise characteristic that is observed in both the SLD and the dual SLD in Fig. 4: the experiment underestimates (gray background) the number of Pauli operators $P \in \mathcal{S}$ and $P \in \mathcal{S}^\perp$ when $n - \text{wt}(P)$ is even, whereas that of the opposite case is overestimated (pink shaded bars). We explain this as follows. First, we have $A_i = 0$ in Eq. (91) for all odd i , which means that \mathcal{S} only contains even-weight stabilizers. Hence, Lem. 2 implies that—for the investigated code—Rains' shadow $\tilde{\mathcal{S}}$ [Eq. (44)] coincides with the normalizer \mathcal{S}^\perp [Eq. (24)]. For enumerators, this implies that $\tilde{\mathbf{a}}[\rho_{\text{QECC}}^{\text{ideal}}] = \mathbf{b}[\rho_{\text{QECC}}^{\text{ideal}}]$ is a $(+1)$ -eigenvector of the TPD-to-dual-SLD transform $\tilde{T}'^{-1} \tilde{M}$ from Fig. 1. The impact of noise is easily understood in the TPD picture, where it manifests itself in the increased occurrence of odd-singlet events (within the constraints of Cor. 5). In our case, we see that the

largest deviation from the ideal case is that some of the probability $\tilde{a}_5[\rho]$ (blue) has leaked into $\tilde{a}_4[\rho]$ and $\tilde{a}_6[\rho]$ (yellow), which correspond to two, three, and one singlet, respectively. As the measured vector $\tilde{\mathbf{a}}[\rho]$ still has a fairly large overlap with its ideal version, it is unsurprising that $\mathbf{b}[\rho] = \tilde{T}'^{-1} \tilde{M} \tilde{\mathbf{a}}[\rho]$ is fairly close to $\tilde{\mathbf{a}}[\rho]$, which is indeed what we observe in Fig. 4.

Besides the raw data (red dots), we also show in Fig. 4 the QWEs that are obtained when error correction (blue dots) or detection (green dots) is performed before the QWEs are estimated. Here, it is important to note that—for color codes—all Clifford gates and, therefore, also Bell measurements can be implemented transversally. Thus, we can regard the here-reported experiment as *logical* Bell sampling. Leveraging a lookup table decoder for the $[[7, 1, 3]]$ code, we can effectively (in classical postprocessing) project $\rho_{\text{QECC}}^{\text{exp}}$ onto the logical code space without discarding any data. Alternatively, we can postselect for events without detected errors by discarding all Bell samples where at least one parity check is violated. Here, we can keep 4,067 and 4,458 Bell samples (from 10,000 each) for $|0, 0\rangle_L$ and $|0, 1\rangle_L$, respectively, where no errors are detected. Averaging the resulting two TPDs then results in the displayed error-detected, postselected QWEs.

We can see in Fig. 4 that the error-corrected QWEs (blue dots) are generally closer to their ideal values than in the raw case (red dots). Therefore our experiment demonstrates the hallmark of QEC: noise removal. Furthermore, Fig. 4 reveals that the postselected data (green dots) are in overwhelmingly good agreement with ideal predictions. However, this is at the expense of sacrificing Bell samples, which increases statistical uncertainty. Even when accounting for error bars, the overall error detection results surpass those of error correction, indicating that the elimination of systematic errors outweighs the introduction of statistical errors. This highlights the practical advantage of error detection over correction when the number of qubits is small.

Before wrapping up this section, we should mention that, although we limited ourselves to experiments with stabilizer states and codes, the general case can be treated analogously. An interesting testbed for studying non-stabilizer codes are the ones from Ref. [130] whose QWEs played an important role in their discovery. The logical basis states of these exotic codes are superpositions of Dicke states [Eq. (111)], which can be prepared via *entanglement carving* [148–153]. Proof-of-principle entanglement carving experiments have been reported for neutral atoms trapped in optical lattices [154, 155] and optical tweezers [156] as well as for ions in a segmented Paul trap [157]. As such, we anticipate that the outlined experiment will be within reach in the near future.

V. SCALABILITY CONSIDERATIONS

Now that we have experimentally demonstrated that QWEs can be measured via two-copy Bell sampling, we turn to the pressing question of scalability. Specifically, we analyze two potential scalability bottlenecks. For one, we assess how state preparation and measurement errors propagate into errors on the measured quantities in Sec. V A. Second, in Sec. V B, we

investigate the effect of statistical errors arising from finite sample sizes. In brief, we find that scalable measurements are always possible for TPDs and APDs but not always for SLDs. Thus, in Sec. VC, we finally speculate on the complexity-theoretic origins of the scalability bottlenecks that sometimes arise in the case of SLDs.

A. Robustness guarantees against experimental imperfections

To analyze how robust the two-copy Bell sampling protocol for measuring QWEs (recall Fig. 2) is against experimental imperfections, we continue to develop our theory from Sec. III. The first step is to revisit the two-copy observables.

Lemma 6 (Operator norms of $2n$ -qubit QWE observables) *The operator norms of the observables from Eqs. (57), (65), and (70) are given by $\|W_i\|_\infty = 3^i \binom{n}{i} / 2^n$, $\|W'_i\|_\infty = 1$, and $\|\tilde{W}_i\|_\infty = 1$.*

Proof: The upper bounds follow from an application of the triangle inequality to the respective definitions and from the fact that Pauli and SWAP operators have unit operator norm. Conversely, the matching lower bounds follow from $\langle \Psi | W_i | \Psi \rangle = 3^i \binom{n}{i} / 2^n$ and $\langle \mathbf{0} | W'_i | \mathbf{0} \rangle = \langle \mathbf{0} | \tilde{W}_i | \mathbf{0} \rangle = 1$, where $|\Psi\rangle = |\Psi^-\rangle^{\otimes n}$ and $|\mathbf{0}\rangle = |0\rangle^{\otimes 2n}$. \square

In other words, luckily, the TPD and APD observables \tilde{W}_i and W'_i , respectively, have operator norms that are constant and small. The operator norm of the SLD observable W_i , on the other hand, blows up exponentially in general but not if i is constant. In light of the next result, one can thus robustly confirm that a promised pure input state is m -uniform if m is a sufficiently small constant. Indeed, operator norms relate to the sensitivity to experimental imperfections as follows.

Theorem 7 (Robustness guarantees for estimating the QWEs) *Let ρ be an n -qubit state, $\mathbf{a}_i[\rho] \in \{a_i[\rho], a'_i[\rho], \tilde{a}_i[\rho]\}$ one of its QWEs, and $\Omega_i \in \{W_i, W'_i, \tilde{W}_i\}$ the corresponding observable from Eq. (57), (65), or (70). From Bell sampling experiments, we can estimate $\mathbf{a}_i[\rho]$ up to a systematic error of $\varepsilon > 0$ if experimental imperfections are below $\varepsilon / \|\Omega_i\|_\infty$. More precisely, $\varepsilon = \|\Omega_i\|_\infty \|\sigma - \rho \otimes \rho\|_1$, where σ denotes the effective experimental $2n$ -qubit state that incorporates all preparation and readout errors (including those from CNOT gates). Therefore, TPDs and APDs can be measured robustly while SLDs cannot—in the worst case.*

Proof: Since we have effectively implemented σ instead of $\rho \otimes \rho$, our estimator $\hat{\mathbf{a}}_i = \text{Tr}[\Omega_i \sigma]$ for $\mathbf{a}_i[\rho] = \text{Tr}[\Omega_i(\rho \otimes \rho)]$ is biased. Indeed, the systematic error is given by

$$|\hat{\mathbf{a}}_i - \mathbf{a}_i[\rho]| = \|\Omega_i(\sigma - \rho \otimes \rho)\|_1 \quad (95)$$

and Hölder's inequality yields

$$|\hat{\mathbf{a}}_i - \mathbf{a}_i[\rho]| \leq \|\Omega_i\|_\infty \|\sigma - \rho \otimes \rho\|_1 = \varepsilon, \quad (96)$$

which completes the proof. \square

How does the error $\|\sigma - \rho \otimes \rho\|_1$ relate to experiments? As σ is the imperfect experimental realization of $\rho \otimes \rho$, there must be some quantum channel \mathcal{E} such that $\sigma = \mathcal{E}[\rho \otimes \rho]$. We find the bound

$$\|\sigma - \rho \otimes \rho\|_1 \leq \|\mathcal{E} - \mathcal{I}\|_{1 \rightarrow 1}, \quad (97)$$

as an immediate consequence of the definition

$$\|\mathcal{E} - \mathcal{I}\|_{1 \rightarrow 1} = \max_{\|\omega\|_1 \leq 1} \|\mathcal{E}(\omega) - \mathcal{I}(\omega)\|_1 \quad (98)$$

of the one-to-one norm, which lower-bounds the well-known diamond norm. In the latter norm, the distance between two Pauli error channels equals twice the total variation distance of the corresponding Pauli error probability vectors [158]. Thus,

$$\|\mathcal{E} - \mathcal{I}\|_{1 \rightarrow 1} \leq 2(1 - p_0), \quad (99)$$

if \mathcal{E} is a Pauli channel with zero-error probability p_0 . For example, for the local depolarizing noise channel $\mathcal{E} = \mathcal{E}_p^{\otimes n}$, we have $p_0 = (1 - 3p/4)^n$. Thus, for every constant value $p > 0$ of noise per qubits, p_0 is exponentially suppressed in n , i.e., the QWEs of ρ and $\mathcal{E}_p^{\otimes n}[\rho]$ will unsurprisingly often show noticeable differences. Nevertheless, as the measured state $\sigma = \mathcal{E}_p^{\otimes n}[\rho] \otimes \mathcal{E}_p^{\otimes n}[\rho]$ is still a two-copy state, the Bell sampling protocol still gives rise to an unbiased measurement of QWEs, however, for the noisy state $\mathcal{E}_p^{\otimes n}[\rho]$. For examples of many-body quantum states with a noteworthy amount of noise yet interesting QWEs, see App. G.

A more serious issue is if the two copies become entangled with each other. Let us model such a scenario via a collection of m coherent overrotations

$$\mathcal{E} = \prod_{i=1}^m \mathcal{U}_i, \quad (100)$$

where each quantum channel \mathcal{U}_i implements the unitary

$$U_i = \exp(-it_i H_i) \quad (101)$$

for some small times $t_i > 0$ and error Hamiltonians H_i acting on an arbitrary number of qubits. Using standard arguments [159], we find the bound

$$\|\sigma - \rho \otimes \rho\|_1 \leq 2 \sum_{i=1}^m \min_{\phi \in [0, 2\pi)} \|U_i - \mathbb{1}e^{i\phi}\|_\infty. \quad (102)$$

For each term in Eq. (102), we can insert Eq. (101), which yields

$$\begin{aligned} \min_{\phi} \|U_i - \mathbb{1}e^{i\phi}\|_\infty &= \min_{\phi} \left\| e^{-i(t_i H_i + \phi)} - \mathbb{1} \right\|_\infty \\ &= 2 \min_{\phi} \left\| \sin\left(\frac{t_i H_i + \phi}{2}\right) \right\|_\infty \\ &\leq t_i \min_{\phi \in \mathbb{R}} \|H_i + \phi\|_\infty \\ &= t_i \frac{\lambda_{\max}[H_i] - \lambda_{\min}[H_i]}{2}, \end{aligned} \quad (103)$$

where we have used the unitary equivalence of the operator norm as well as the bound $|\sin(x)| \leq |x|$. Here, the difference

$\Delta[H_i] = \lambda_{\max}[H_i] - \lambda_{\min}[H_i]$ is the *spectral width* of the error Hamiltonian H_i . We have thus established the bound

$$\|\sigma - \rho \otimes \rho\|_1 \leq \sum_{i=1}^m t_i \Delta[H_i], \quad (104)$$

which makes the intuition “*the error on the prepared state remains small if errors in the preparation circuits are neither too frequent nor too strong*” mathematically precise.

B. Sample complexity bounds

Sample complexity bounds are essential for predicting the runtime of an experiment prior to its execution. Let us denote by N the number of Bell samples $\alpha_1, \dots, \alpha_N \in \{\Phi^\pm, \Psi^\pm\}^n$ taken from two copies of an n -qubit state ρ by repeatedly executing the experiment described in Fig. 2 above. The next result settles the question how large one has to select N in order to ensure accurate estimation of the various QWEs.

Theorem 8 (Sample complexities for estimating the QWEs) *Let ρ be an n -qubit state, $\alpha_i[\rho] \in \{a_i[\rho], a'_i[\rho], \tilde{a}_i[\rho]\}$ one of its QWEs, and $\Omega_i \in \{W_i, W'_i, \tilde{W}_i\}$ the corresponding observable from Eq. (57), (65), or (70). Let $\varepsilon, \delta > 0$ be fixed target accuracy parameters. For every $i \in \{0, \dots, n\}$, it is sufficient to gather*

$$N = \frac{\Delta[\Omega_i]^2}{2\varepsilon^2} \ln\left(\frac{2}{\delta}\right) \quad (105)$$

many Bell samples from $\rho \otimes \rho$ to ensure a statistical error of $|\hat{a}_i - \alpha_i[\rho]| < \varepsilon$ with probability at least $1 - \delta$, where $\Delta[\Omega_i] \leq 2\|\Omega_i\|_\infty$ is the spectral width of Ω_i . Moreover, if we want that $|\hat{a}_i - \alpha_i[\rho]| < \varepsilon$ holds for all $i \in \{0, \dots, n\}$ simultaneously, then

$$N = \frac{\Delta[\Omega_i]^2}{2\varepsilon^2} \ln\left(\frac{2(n+1)}{\delta}\right) \quad (106)$$

Bell samples from $\rho \otimes \rho$ are sufficient.

Proof: For every sample $\alpha \in \{\Phi^\pm, \Psi^\pm\}^n$, the single-shot estimator $\langle \alpha | \Omega_i | \alpha \rangle$ takes values in the spectrum of Ω_i . Therefore, Höfdding’s inequality establishes the first claim. The second claim follows similarly by applying a union bound argument. \square

Theorem 8 has a few immediate consequences. For one, we have $\Delta[\tilde{W}_i] = 1$ since \tilde{W}_i is a projector. Hence, we only need at most $N = \varepsilon^{-2} \ln(2/\delta)/2$ samples to estimate any triplet probability $\tilde{a}_i[\rho]$ of interest. This should not come as a surprise as two-copy Bell sampling allows us to directly sample from the TPD $\tilde{a}[\rho]$. Similarly, for every subsystem size i of interest, estimating the averaged purity $a'_i[\rho]$ requires only up to $N = 2\varepsilon^{-2} \ln(2/\delta)$ samples as $\Delta[W'_i] = 2$, by Lem. 6. For SLDs, on the other hand, the situation is more delicate because $\|W_i\|_\infty = 3^i \binom{n}{i}/2^n$ can be exponentially large. Therefore, in general, exponentially many Bell samples are required to estimate the i -body sector length $a_i[\rho]$.

For any constant value of i , however, $\|W_i\|_\infty$ is exponentially *small* in n . As such, the total amount of squared i -body Pauli correlations, i.e., $A_i[\rho] = 2^n a_i[\rho]$ can be estimated using just $N = (3^i \binom{n}{i})^2 \varepsilon^{-2} \ln(2/\delta)/2 = O(n^{2i} \varepsilon^{-2} \ln(1/\delta))$ many Bell samples. This shows that checking fixed- m uniformity of a promised pure input state is not only robust (Thm. 7) but also sample efficient (Thm. 8). A related application involves determining a lower bound for the distance of a QECC. We should point out, however, that—while this does constitute a valid strategy with the additional single-setting benefit—directly measuring all $\sum_{i=1}^m 3^i \binom{n}{i}$ low-weight Pauli operators may require fewer samples for the same task.

Let us stress the fact that Thm. 8 only concerns the worst-case sample complexity for measuring QWEs. While this suffices to guarantee sample-efficient estimation of TPDs and APDs, we need to take a closer look in the case of SLDs. To this end, we point out that the statistics arise from a multinomial distribution. As such, we can explicitly compute the variances

$$\sigma_i^2 = \frac{1}{N} \sum_{j=0}^n |\tilde{T}_{i,j}^{-1}|^2 \tilde{a}_j[\rho] - \frac{1}{N} \left(\sum_{j=0}^n \tilde{T}_{i,j}^{-1} \tilde{a}_j[\rho] \right)^2 \quad (107)$$

of the individual estimators \hat{a}_i for $a_i[\rho]$, from which the total variance of the SLD follows as

$$\sigma^2 = \mathbb{E} \left[\sum_{i=0}^n (a_i[\rho] - \hat{a}_i)^2 \right] = \sum_{i=0}^n \sigma_i^2, \quad (108)$$

where the expectation value is over different realizations of an N -sample experiment. Since $\tilde{T}_{i,j}^{-1}$ takes exponentially large values for small triplet counts $j \lesssim n/2$ [160], the variance σ^2 of the SLD highly depends on where the TPD concentrates. While Cor. 5 guarantees that the mean of the TPD is never smaller than $3n/4$, it does not prevent the existence of heavy tails of the TPD around $j \approx n/2$ triplets. Indeed, such issues occur, e.g., for Dicke states with a constant filling fraction and for GHZ states, see App. G for a visual impression.

Fixing a target variance of $\sigma^2 = 10^{-4}$ for the SLD, we solve Eq. (108) for the number N of required Bell samples and plot the result in Fig. 5 as a function of the number n of qubits. The sample requirements highly depend on the specific state, for which we insert the corresponding QWEs into Eq. (108). We investigate various Dicke state families (whose QWEs are treated in Sec. VI below), GHZ and cycle graph states (whose QWEs are taken from Ref. [87]), and average-case states. For the latter, we compute N in Fig. 5 by inserting [106]

$$\mathbb{E}_{|\psi\rangle \sim \mu_2} a_i[|\psi\rangle\langle\psi|] = \begin{cases} \frac{1}{2^n} & \text{if } i = 0, \\ \frac{3^i \binom{n}{i}}{2^n(2^n+1)} & \text{if } i > 0, \end{cases} \quad (109)$$

into Eq. (108), where μ_2 is an arbitrary 2-*design*, e.g., that of uniformly-random stabilizer or Haar-random states [14]. Also note that the output distribution of brickwork circuits is an approximate 2-*design* after linear depth [161].

We can see in Fig. 5 that the curves for GHZ (purple) and half-filled Dicke states (red), which lie almost on top of each

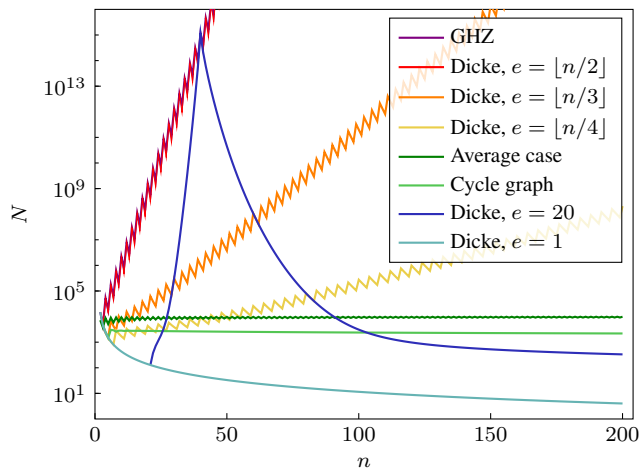


FIG. 5. Number N of Bell samples that is required for reaching a variance $\sigma^2 = 10^{-4}$ of the Shor-Laflamme quantum weight enumerator (aka sector length) distribution (SLD) for various states as a function of the number n of qubits. For some states, e.g., half-filled Dicke states [Eq. (111)], estimating SLDs up to constant additive error has exponential sample complexity. In the average case of a 2-design, however, a constant number of Bell samples suffices.

other, are quickly diverging: even for a moderate number of $n = 50$ qubits, one would need more than 10^{16} Bell samples to achieve an SLD variance of $\sigma^2 = 10^{-4}$. Also for third-filled (orange) and quarter-filled (yellow) Dicke states, the sample requirements scale exponentially in n . For a constant number e of Dicke excitations, e.g., $e = 20$ (dark blue) and $e = 1$ (bright blue), on the other hand, the sample requirements asymptotically [162] decrease with n . Indeed, for $n > 100$ qubits, less than a few thousands (tens) of Bell samples are required for $e = 20$ ($e = 1$). Finally, the sample requirements of average-case (dark green) and cycle graph states (bright green) show almost no dependence on n , namely $N \approx 10^4$ and $N \lesssim 3 \times 10^3$, respectively.

The exponential behavior of the sample requirements for GHZ and Dicke states with a constant filling factor are easily explained by the aforementioned heavy tails of the respective TPDs around $j \approx n/2$ triplets. When the number e of Dicke excitations is constant, however, N decreases in the regime $n > 2e$ because the QWEs become increasingly similar to those of a pure product state (this was formally proven for $e = 1$ in App. D of Ref. [87]). For the latter, a single Bell sample is sufficient because the TPD of $|0\rangle^{\otimes n}$ has a vanishing variance. Furthermore, we attribute the observation that average-case and cycle graph states feature the same qualitative behavior to an earlier observation [87] that cycle graph and other cluster states have SLDs that are closely matched by random states. For them, the TPD only features a single peak at $j = 3n/4$ triplets that is sufficiently concentrated to prevent an uncontrolled spread of statistical errors via Eq. (108). For a depiction of the QWEs of Dicke, cycle graph, and GHZ states on $n = 200$ qubits, see App. G.

Our discussion of Fig. 5 shows that the situation is not as concerning as it might seem based on an initial look at Thm. 8.

While some states do require exponentially many Bell samples to estimate the SLD up to constant additive error, for most states, the sample requirements are manageable. Moreover, such states include cluster states, which are highly entangled but can be easily prepared using a constant-depth circuit.

C. Complexity-theoretic comments

Why is it that TPDs and APDs always have an efficient sample complexity but SLDs only sometimes? To shed some light on this subtle question, let us highlight a few facts that are more or less well-known.

For one, computing the distance of a classical linear code is NP-hard [63], and distances can be computed from SLDs via Eq. (27) above. At first glance, this might indicate a connection to our question, however, such a conclusion would be too naive. Indeed, to compute distances from SLDs, one has to know the SLD *exactly*. By rounding $A_i[\rho] = 2^n a_i[\rho]$ to its closest integer, this is only possible if the additive error on $a_i[\rho]$ is exponentially small. Since neither SLD, APD, nor TPD can be efficiently measured up to exponential precision—otherwise one could also estimate SLDs to exponential precision (despite the exponentially-large operator norms of the involved transformations, see App. H), which would effortlessly prove $\mathbf{P} = \mathbf{NP}$ —the distance strategy appears to be a dead end to our question. After all, we are interested in understanding the *difference* in sample complexity between the three QWEs; and for computing distances, there is none.

A second strategy that also turns out to not fully resolve the issue starts with the observation that for a pure state Ψ , the SLD $\mathbf{a}[\Psi]$ is a probability distribution [Eq. (12)]. Thus, if one could directly sample from $\mathbf{a}[\Psi]$, then one could efficiently estimate $\mathbf{a}[\Psi]$ up to constant additive error—just as we can always do in the case of TPDs. So when is it possible to sample from the SLD? In Ref. [163] by partially overlapping authors, a related question was investigated in detail. More concretely, it was studied for which states Ψ one can efficiently sample Pauli operators $P \in \{I, X, Y, Z\}^{\otimes n}$ according to probability distribution

$$\Xi(P) = \frac{\text{Tr}[\Psi P]^2}{2^n}. \quad (110)$$

Clearly, the SLD arises as a marginal distribution of Ξ . Hence, if one can efficiently sample from Ξ , then also from $\mathbf{a}[\Psi]$. Although we cannot directly transfer negative results from Ref. [163], it is still interesting to point out in which scenarios one can or cannot sample from Ξ . Sampling is provably hard for states with high entanglement and high magic. Conversely, it is efficiently possible for low-rank matrix product states (low entanglement) and for states prepared via Clifford circuits doped with a small number of $\sqrt[4]{Z}$ -gates (low magic).

Finally, the situation changes completely if one has access not only to copies of Ψ but also to copies of Ψ^T . From the latter, one can prepare the spin-flipped state $\tilde{\Psi} = Y^{\otimes n} \Psi^T Y^{\otimes n}$. Since the directly-measurable triplet probability $\tilde{a}_i[\Psi]$ from Eq. (37) is a sum over terms of the form $\text{Tr}[\Psi P \tilde{\Psi} P]$, and the

i -body sector length $a_i[\Psi]$ from Eq. (10) is the same sum but over $\text{Tr}[\Psi P]^2 = \text{Tr}[\Psi P \Psi P]$, one can directly sample from the SLD by taking Bell samples from $\Psi \otimes \tilde{\Psi}$ and counting the number of triplets in the outcomes. By the same logic, one can efficiently sample from the dual SLD, which—in contrast to the SLD itself—is always a normalized probability distribution, for arbitrary mixed states that are invariant under transposition ($\rho = \rho^T = \rho^*$) or state inversion ($\rho = \tilde{\rho}$). This provides partial insights to our question raised at the beginning of this subsection. For example, if—in Fig. 5 we would have a priori known that the probed state Ψ_{GHZ} is equal to $\tilde{\Psi}_{\text{GHZ}}$ (assuming n is even), then we could have simply reused the accurately measured TPDs as an estimator for the SLD as the two distributions coincide in the ideal case.

VI. THEORETICALLY ANALYZING THE PERSISTENCE OF ENTANGLEMENT AGAINST LOCAL NOISE

In this final section, let us also showcase how the machinery of QWEs can be leveraged to theoretically predict how much noise certain entangled states are able to withstand without becoming fully separable. Specifically, we analyze Dicke states in the context of local depolarizing noise. We expand on earlier strategies [87] in two ways: first, we exploit that not only the n -body sector length and the purity criterion can be tested via SLDs but also the concurrence and the fidelity criterion—a connection that we have established in the present work. Second, we demonstrate for concrete examples that the strategy of Ref. [87] is not just limited to stabilizer states.

Denote by n and e the number of qubits and excitations, respectively, of a Dicke state vector

$$|D_e^n\rangle = \frac{1}{\sqrt{\binom{n}{e}}} \sum_{\mathbf{x} \in \mathbb{F}_2^n: |\mathbf{x}|=e} |\mathbf{x}\rangle, \quad (111)$$

where $|\mathbf{x}|$ is the Hamming weight of $\mathbf{x} \in \mathbb{F}_2^n$. Leveraging the Schmidt decomposition of $|D_e^n\rangle$ [164], we find that the purity of every subsystem S containing $|S| = i$ qubits (and therefore also their average) is given by

$$a'_i[\Psi_e] = \sum_{j=0}^e \left(\frac{\binom{i}{j} \binom{n-i}{e-j}}{\binom{n}{e}} \right)^2, \quad (112)$$

where we have introduced the notation $\Psi_e = |D_e^n\rangle\langle D_e^n|$. Applying the matrix from Eq. (30), we find $\mathbf{a}[\Psi_e] = T'^{-1} \mathbf{a}'[\Psi_e]$. Observe that in the SLD basis, local depolarizing noise acts diagonally [Eq. (15)], i.e., $\mathbf{a}[\mathcal{E}_p^{\otimes n}[\Psi_e]] = E(p) \mathbf{a}[\Psi_e]$, where

$$E(p) = \text{diag}(1, (1-p)^2, \dots, (1-p)^{2n}). \quad (113)$$

By transforming back to Rains' unitary QWEs (APD) or forth to Rains' shadow QWEs (TPD), we can easily compute

$$\mathbf{a}[\mathcal{E}_p^{\otimes n}[\Psi_e]] = E(p) T'^{-1} \mathbf{a}'[\Psi_e], \quad (114)$$

$$\mathbf{a}'[\mathcal{E}_p^{\otimes n}[\Psi_e]] = T' E(p) T'^{-1} \mathbf{a}'[\Psi_e], \quad (115)$$

$$\text{and } \tilde{\mathbf{a}}[\mathcal{E}_p^{\otimes n}[\Psi_e]] = \tilde{T} E(p) \tilde{T}'^{-1} \mathbf{a}'[\Psi_e] \quad (116)$$

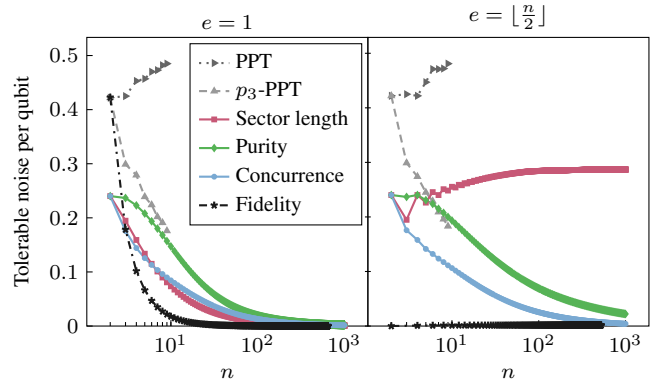


FIG. 6. Noise robustness of the presence of entanglement in W states ($e = 1$) and half-filled Dicke states ($e = \lfloor \frac{n}{2} \rfloor$) for various entanglement criteria described in the main text as a function of the number n of qubits. If the noise level p is below any of the curves, the locally-depolarized state $\mathcal{E}_p^{\otimes n}[\Psi_e]$ is necessarily entangled according to the corresponding criterion.

from Eq. (112). This, in turn, allows us to numerically find the largest noise value p for which certain criteria certify the presence of entanglement. In Fig. 6, we show the results for W states ($e = 1$) and half-filled Dicke states ($e = \lfloor \frac{n}{2} \rfloor$). The n -body sector length criterion (pink) and the fidelity criterion $\langle D_e^n | \rho | D_e^n \rangle > f_e^n$ (black) can be tested on the level of SLDs via Eq. (14) and Eq. (17), respectively, where the fidelity bounds f_1^n and $f_{n/2}^n$ are taken from Ref. [165] and Ref. [164], respectively. For $f_{n/2}^n$, we assume n to be even. The purity criterion, $a'_n[\rho] = \text{Tr}[\rho^2] > \frac{1}{n} \sum_i \text{Tr}[\text{Tr}_i[\rho]^2] = a'_{n-1}[\rho]$ (green), is testable via Eq. (115). By Thm. 3, $\tilde{a}_j[\mathcal{E}_p^{\otimes n}[\Psi_e]]$ can be interpreted as the probability to observe j triplets in a Bell sampling experiment with two noisy copies of Ψ_e . Thus, we can also find the largest value of p for which the lower bound on the concurrence $C[\mathcal{E}_p^{\otimes n}[\Psi_e]]$ from Ineq. (82) is still positive (blue).

Using brute force density matrix calculations, we also compute the largest value of p for which the *positive partial transposition* (PPT) criterion (dark gray) and its relaxation to the p_3 -PPT criterion (bright gray) certify entanglement [166–169]. We point out that the choice of bipartition is of crucial importance here. For the purity criterion, we find it to be best practice to probe entanglement across a bipartition of size $n - 1$ versus 1 while bipartitions of size $\lfloor \frac{n}{2} \rfloor$ versus $\lfloor \frac{n}{2} \rfloor$ lead to better noise thresholds for PPT and p_3 -PPT. We observe in Fig. 6 that the PPT criterion, which we can only evaluate for a small number qubits, leads to the best lower bound on the noise threshold. For very large qubit numbers, we can still apply the QWE machinery and we find that the purity criterion leads to better results than the concurrence criterion [Eq. (80)] for both W states and half-filled Dicke states. The n -body sector length criterion yields poor results for W states, however, we find that half-filled Dicke states can withstand an astonishing amount ($p \geq 0.28$ for all $n \geq 52$) of depolarizing noise per qubit before $a_n[\mathcal{E}_p^{\otimes n}[\Psi_{\lfloor n/2 \rfloor}]]$ falls below 2^{-n} .

Having said this, we stress that this noise threshold only concerns the presence of entanglement according to that cri-

terion. Detecting entanglement in the laboratory, however, remains challenging as we just saw in Fig. 5 in Sec. V.

In conclusion, entanglement criteria based on QWEs have several advantages over other criteria such as p_3 -PPT and PPT: (i) they can handle local noise as easily as global noise, (ii) they can be easily applied to very large system sizes, and (iii) they can test multiple criteria at the same time.

VII. DISCUSSION

In this work, we have established a concrete physical interpretation of the longstanding mathematical concept known as quantum shadow enumerators: they can be understood as the triplet probability distribution that arises in a two-copy Bell sampling experiment (Thm. 3). This insight led us to a fruitful connection between quantum error correction and entanglement, where shadow enumerators and Bell sampling occupy pivotal roles, respectively. Prioritizing practicality, we made strides to strengthen this new connection. For one, we have showcased—both theoretically and experimentally—how the weight enumerator machinery from quantum error correction can be repurposed as a powerful tool for entanglement characterization and, more generally, for benchmarking the performance of quantum devices. Conversely, we have explained and experimentally demonstrated how various notions of quantum weight enumerators (e.g., the numbers of fixed-Pauli-weight stabilizer and logical operators of a probed quantum error-correcting code) can be directly measured via two-copy Bell sampling. In this context, we have also clarified how error correction relates back to Bell sampling: for many codes, Bell sampling can be regarded as a *logical* protocol, which grants compatibility with the error correction capabilities of the code whose weight enumerators are being measured. In vivid terms, the experiment corrects itself. We demonstrated this possibility on our trapped-ion quantum processor using the example of the seven-qubit color code. Furthermore, to support quantum state analyses beyond the paradigm of quantum error correction, we have developed and implemented natural error mitigation strategies, which make heavy use of the quantum weight enumerator machinery themselves.

Acknowledging the impossibility of completely eliminating errors, we have proven rigorous robustness guarantees against experimental imperfections (Thm. 7). In a similar spirit, we have derived concrete sample complexity bounds (Thm. 8), thereby revealing a surprising distinction in the hardness of estimating various instances of quantum weight enumerators via Bell sampling: while triplet probabilities (aka shadow enumerators) and averaged purities (aka unitary enumerators) can always be measured in a scalable manner, estimating sector lengths (aka Shor-Laflamme enumerators) has an exponential worst-case sample complexity. By investigating the origins of this issue, we were able to show that, fortunately, the average-case sample complexity remains unaffected. In conjunction with our reduction of the computational postprocessing complexity from exponential to polynomial, these advances pave the way for blue-sky research into the fundamental structure of large-scale quantum states. This is complemented by the

fact that Bell sampling is a single-setting protocol that allows for extremely fast data acquisition in practice.

Moving past the direct applicability of our developments, we envision several future research directions. With two-copy Bell measurements, one can efficiently probe certain quadratic properties of a quantum state ρ , however, there also exist many higher-moment entanglement criteria [168–171]. In this context, one could explore existing generalizations [172–174] of the weight enumerator machinery in the $\rho^{\otimes k}$ scenario for $k \geq 3$. In a different direction, one may consider properties that are not quadratic within a single state, but rather involve multiple states. A more general notion of quantum weight enumerators pertains to $\text{Tr}[\rho\sigma]$ instead of $\text{Tr}[\rho^2]$, allowing for a straightforward translation of the purity aspects of this work into the trace overlap between different states [51, 53]. This plausibly opens up new methods and applications in state comparison and fidelity estimation. In this work, we have placed heavy emphasis on the connection between the “big three” quantum weight enumerators, but this does not mean that they constitute everything there is to be discovered about enumerators. There are conceivably other, yet undiscovered, enumerator variants where the triplet probability distribution framework may reveal interesting connections. For example, recent proposals for ‘circuit’ and ‘signed’ enumerators could potentially benefit from the TPD connection [175, 176].

Finally, we highlight a well-known connection between Bell sampling and the Hong-Ou-Mandel effect from quantum optics [44, 177–180]. An important application of this effect is to assess the indistinguishability of two photons, which can be regarded as a quantum-optical analog to estimating state overlaps on digital quantum computers. The latter can be achieved by performing transversal Bell measurements on two different input states. In this work, we have focused on the digital version of this protocol. It would be interesting to explore the implications of our developments for quantum optics and, more broadly, for analog quantum simulations.

Note added. After discovering the physical interpretation of shadow enumerators as triplet probabilities in two-copy Bell measurements, we became aware of a complementary result that interprets them as probabilities in SWAP tests [181]. We regard these two viewpoints as independent perspectives on an interesting problem.

ACKNOWLEDGMENTS

The authors express their gratitude toward Marine Demarty, Sofienne Jerbi, Ferdinand Schmidt-Kaler, David C. Spierings, and Nikolai Wyderka for their insightful discussions.

This work has been supported by the Quantum Flagship (Millenion, for this is the result of a joint-node collaboration), the BMBF (RealistiQ, QSolid, MUNIQ-Atoms), the Munich Quantum Valley (K-8), the BMWK (EniQmA), the QuantERA (HQCC), the Cluster of Excellence MATH+, the DFG (CRC183), the Einstein Foundation (Einstein Research Unit on Quantum Devices), Berlin Quantum, and the ERC (DebuQC). This research was sponsored by IARPA and the Army Research Office, under the Entangled Logical Qubits

program, and was accomplished under Cooperative Agreement Number W911NF-23-2-0212. The views and conclusions contained in this document are those of the authors and should not be interpreted as representing the official policies, either expressed or implied, of IARPA, the Army Research Office, or the U.S. Government. The U.S. Government is authorized to reproduce and distribute reprints for Government purposes notwithstanding any copyright notation herein.

The Innsbruck team acknowledges funding by the European Union under the European Research Council (ERC, QUDITS, 101080086), by the European Union's Horizon Europe research and innovation programme under grant agreement No 101114305 ("MILLENION-SGA1" EU Project), and by the Office of the Director of National Intelligence (ODNI), Intelligence Advanced Research Projects Activity (IARPA), via US Army Research Office (ARO) grant No. W911NF-21-1-0007. Views and opinions expressed are however those of the author(s) only and do not necessarily reflect those of the European Union or the European Research Council Executive Agency. Neither the European Union nor the granting authority can be held responsible for them. We also acknowledge support by the Austrian Science Fund (FWF Grant-DOI 10.55776/F71) (SFB BeyondC), the Austrian Research Promotion Agency under Contracts Number 897481 (HPQC), and the Institut für Quanteninformation GmbH.

Appendix A: Notational overview

For convenience, this appendix explicitly repeats the matrix entries for all nine transforms that are displayed in Fig. 1 of the main text. As always, let n be the number of qubits. The MacWilliams transforms are given by

$$M_{i,j} = \frac{1}{2^n} \sum_{l=0}^i \binom{n-j}{i-l} \binom{j}{l} (-1)^l 3^{i-l}, \quad (7)$$

$$M'_{i,j} = \delta_{i,n-j}, \quad (8)$$

$$\text{and } \tilde{M}_{i,j} = (-1)^{n+i} \delta_{i,j} \quad (9)$$

in the basis of SLDs, APDs, and TPDs, respectively. To transform SLDs into APDs and back again, one has to use the lower triangular matrices with entries

$$T'_{i,j} = \frac{2^{n-i}}{\binom{n}{i}} \binom{n-j}{n-i} \quad (29)$$

$$\text{and } T'^{-1}_{i,j} = \frac{\binom{n}{j}}{2^{n-j}} \binom{n-j}{n-i} (-1)^{i+j}. \quad (30)$$

To transform SLDs into TPDs (Rains' shadow QWEs) and back again, one must apply the Krawtchouk matrices whose entries are given by

$$\tilde{T}_{i,j} = \frac{1}{2^n} \sum_{l=0}^i \binom{n-j}{i-l} \binom{j}{l} (-1)^{j-l} 3^{i-l} \quad (39)$$

$$\text{and } \tilde{T}'^{-1}_{i,j} = \frac{1}{2^n} \sum_{l=0}^i \binom{n-j}{i-l} \binom{j}{l} (-3)^{i-l}. \quad (73)$$

Note that $\tilde{T} = MM'\tilde{M}M'$. Finally, one can also directly convert APDs into TPDs, and vice versa, via

$$\tilde{T}'_{i,j} = \frac{1}{2^n} \binom{n}{j} \sum_{l=0}^i \binom{n-j}{i-l} \binom{j}{l} (-1)^{j-l} \quad (A1)$$

$$\text{and } \tilde{T}'^{-1}_{i,j} = \frac{1}{\binom{n}{i}} \sum_{l=0}^i \binom{n-j}{i-l} \binom{j}{l} (-1)^{i-l}. \quad (A2)$$

As the colors in Fig. 1 of the main text illustrate, the only matrices from the above that never unfavorably amplify numerical imprecision (theory) and statistical errors (experiment) of the QWEs are M' , \tilde{M} , and \tilde{T}'^{-1} . For a related discussion, see App. H.

Appendix B: Saving costs when transforming QWEs

From a naive perspective, computing the transformation matrices M , \tilde{T} , \tilde{T}^{-1} , \tilde{T}' , and \tilde{T}'^{-1} from their definitions in App. A has a preprocessing cost of $O(n^4)$. Here we show how this complexity can be reduced to $O(n^2)$ by identifying useful recurrence relations between matrix entries.

In order to compute \tilde{T}'^{-1} for example, we start by omitting the factor $1/\binom{n}{i}$ which can be reapplied later. According to Eq. (A2), the first row then consists of all ones while the first column contains the binomial coefficients with alternating signs, i.e., $(-1)^i \binom{n}{i}$ for $i \in \{0, \dots, n\}$. The crucial insight is that in each 2×2 block of this matrix, the lower-right entry is just the sum of the other three entries. Following this prescription, the entire matrix can be build up from top-to-bottom and left-to-right in $O(n^2)$ steps. Finally, each row is divided by the absolute value of its first entry, thus completing the calculation of \tilde{T}'^{-1} .

Similar instructions are found for the remaining matrices. Specifically, M has almost the same boundary conditions as \tilde{T}'^{-1} (up to normalization), only that $(-1)^i \binom{n}{i}$ appears in the last column instead of the first one. The matrix can then be completed according to $M_{i,j} = 3M_{i-1,j+1} + M_{i-1,j} + M_{i,j+1}$. Moreover, we again stress the fact that the two matrices \tilde{T} and \tilde{T}^{-1} arise from M by changing signs of odd rows and columns, respectively. It is therefore not necessary to recompute \tilde{T} and \tilde{T}^{-1} from their definitions when M is already known.

This approach is limited by numerical precision when adding numbers of largely differing orders of magnitude, however, this issue can be avoided by using integers until the application of normalization factors. In general, storing most of the transformation matrices with exponential operator norm in standard IEEE 754 64-bit floating point format is only possible until $n = 1029$. Until then, we find that the recursive method yields an enormous speed-up compared to the naive approach.

Appendix C: Overlap decay in terms of SLDs

Let ρ be an arbitrary n -qubit state. Expanding it in the Pauli basis yields

$$\rho = \sum_{P \in \{I, X, Y, Z\}^{\otimes n}} \frac{\text{Tr}[\rho P]}{2^n} P. \quad (\text{C1})$$

By linearity of the locally depolarizing channel $\mathcal{E}_p^{\otimes n}[\cdot]$, we find $\mathcal{E}_p^{\otimes n}[\rho] = \sum_P \frac{\text{Tr}[\rho P]}{2^n} \mathcal{E}_p^{\otimes n}[P]$. Since also $\text{Tr}[\cdot]$ is linear, the overlap decay between ρ and $\mathcal{E}_p^{\otimes n}[\rho]$ follows as

$$\text{Tr}[(\mathcal{E}_p^{\otimes n}[\rho])\rho] = \sum_{P, Q} (1-p)^{\text{wt}(P)} \frac{\text{Tr}[\rho P]}{2^n} \frac{\text{Tr}[\rho Q]}{2^n} \text{Tr}[PQ]. \quad (\text{C2})$$

Further exploiting the fact $\text{Tr}[PQ] = \delta_{P, Q} 2^n$, we find

$$\text{Tr}[(\mathcal{E}_p^{\otimes n}[\rho])\rho] = \sum_{P \in \{I, X, Y, Z\}^{\otimes n}} (1-p)^{\text{wt}(P)} \frac{\text{Tr}[\rho P]^2}{2^n}, \quad (\text{C3})$$

and since $\mathcal{E}_p^{\otimes n}[P] = (1-p)^j P$ only depends on $j = \text{wt}(P)$, we can write

$$\begin{aligned} \text{Tr}[(\mathcal{E}_p^{\otimes n}[\rho])\rho] &= \sum_{j=0}^n (1-p)^j \sum_{\substack{P \in \{I, X, Y, Z\}^{\otimes n} \\ \text{wt}(P)=j}} \frac{\text{Tr}[\rho P]^2}{2^n} \\ &= \sum_{j=0}^n (1-p)^j a_j[\rho], \end{aligned} \quad (\text{C4})$$

which completes the proof of Lemma 1 in the main text.

Appendix D: On triplet probability distributions

In this appendix, we translate results from the sector length literature into the picture of triplet probabilities. First, we express moments of triplet probability distributions (TPDs) in terms of few-body Pauli correlators, in Sec. D 1. The question which probability distributions may or may not arise in Bell sampling experiments is addressed in Sec. D 2.

1. Moments of triplet probability distributions

Consider an n -qubit state ρ and denote the i -th moment of its TPD $\tilde{\mathbf{a}}[\rho] = (\tilde{a}_x[\rho])_{x=0}^n$ by

$$\langle \tilde{x}^i \rangle = \sum_{x=0}^n \tilde{a}_x[\rho] x^i. \quad (\text{D1})$$

Simplifying the i -th component of $\mathbf{a}[\rho] = \tilde{T}^{-1} \tilde{\mathbf{a}}[\rho]$ and denoting by $A_i[\rho] = 2^n a_i[\rho]$ the unnormalized version of Shor-

Laflamme QWEs, we find

$$A_1[\rho] = 4\langle \tilde{x} \rangle - 3n, \quad (\text{D2})$$

$$A_2[\rho] = 8\langle \tilde{x}^2 \rangle - (12n - 4)\langle \tilde{x} \rangle + 9\binom{n}{2}, \quad (\text{D3})$$

$$\text{and } A_3[\rho] = \frac{32}{3}\langle \tilde{x}^3 \rangle - (24n - 16)\langle \tilde{x}^2 \rangle \quad (\text{D4})$$

$$+ \frac{54n^2 - 90n + 28}{3}\langle \tilde{x} \rangle - 27\binom{n}{3}. \quad (\text{D5})$$

Rearranging Eq. (D2) yields the TPD's mean

$$\langle \tilde{x} \rangle = \frac{3n + A_1[\rho]}{4}. \quad (\text{D6})$$

Similarly, by inserting Eq. (D6) into Eq. (D3) we obtain the second moment of the TPD,

$$\langle \tilde{x}^2 \rangle = \frac{A_2[\rho] + (3n - 1)(3n + A_1[\rho]) - 9\binom{n}{2}}{8} \quad (\text{D7})$$

as well as its variance

$$\langle \tilde{x}^2 \rangle - \langle \tilde{x} \rangle^2 = \frac{2A_2[\rho] - A_1[\rho]^2 - 2A_1[\rho] + 3n}{16}. \quad (\text{D8})$$

Note that, for pure graph states [127], $A_1[\rho]$ is equal to the number of isolated vertices, while $A_2[\rho]$ counts leaves and twin pairs of the underlying graph [87].

In principle, we could go on and express the i -th moment $\langle \tilde{x}^i \rangle$ of the TPD as a linear combination of $A_0[\rho], \dots, A_i[\rho]$. When

$$\rho = \frac{1}{|\mathcal{S}|} \sum_{S \in \mathcal{S}} S \quad (\text{D9})$$

is a pure stabilizer state or, more generally, the maximally mixed state of a stabilizer QECC with stabilizer group \mathcal{S} , we can compute $A_i[\rho] = |\{S \in \mathcal{S} \mid \text{wt}(S) = i\}|$ in classical runtime $O(n^i)$, which is efficient if i is constant. Similar is true for matrix product states with a low bond dimension.

2. Bounds on triplet probability distributions

For every n -qubit state ρ , the TPD $\tilde{\mathbf{a}}[\rho]$ is a discrete probability distribution on the finite set $\{0, \dots, n\}$. However, not every mathematically well-defined probability distribution on $\{0, \dots, n\}$ can be physically realized as a TPD arising in a two-copy Bell measurement. For example, from Eq. (37), we know that the zero-triplet probability $\tilde{a}_0[\rho] = \frac{\text{Tr}[\rho \tilde{\rho}]}{2^n}$ of any state ρ is upper bounded by 2^{-n} . This bound is tight and attained iff $\rho = \tilde{\rho}$, e.g., for pure half-filled Dicke states and GHZ states, assuming n even. At the other extreme of the distribution, however, we can have probabilities as large as $\tilde{a}_n[|0\rangle\langle 0|^{\otimes n}] = 1$. These observations are manifestations of an even more general asymmetry in TPDs that we are going to unfold now.

Recall from Eq. (D6) that the mean $\langle \tilde{x} \rangle$ of any TPD can be expressed in terms of the (unnormalized) 1-body sector length

$A_1[\rho] = 2^n a_1[\rho]$. From its definition [Eq. (10)] it is clear that $A_1[\rho]$ cannot be negative. Hence, we can lower bound the mean of the TPD via

$$\langle \tilde{x} \rangle \geq \frac{3n}{4}, \quad (\text{D10})$$

which implies that one will always observe a fairly large number of triplets in two-copy Bell sampling experiments. The bound in Ineq. (D10) is tight and attained for the maximally mixed state whose triplet probabilities

$$\tilde{a}_i \left[\frac{\mathbb{1}}{2^n} \right] = \binom{n}{i} \frac{3^i}{4^n} \quad (\text{D11})$$

are binomially distributed since every Bell measurement randomly (with equal probability 25%) results in one of three triplets or in a singlet. Conversely, we recover the well-known upper bound $A_1[\rho] \leq n$ by inserting the trivial bound $\langle \tilde{x} \rangle \leq n$ into Eq. (D6). More generally, it has been shown [77] that

$$0 \leq A_i[\rho] \leq \begin{cases} \binom{n}{1} & \text{if } i = 1 \text{ and } n \geq 1, \\ \binom{n}{2} & \text{if } i = 2 \text{ and } n \geq 3, \\ \binom{n}{3} & \text{if } i = 3 \text{ and } n \geq 5, \end{cases} \quad (\text{D12})$$

which directly translates into bounds on linear combinations of mean, variance, and skewness of admissible TPDs via Eqs. (D2)–(D8). Unfortunately, there cannot exist a nontrivial lower bound on the TPD's variance as the example of any pure product state shows. Nonetheless, yet another bound on linear combinations of sector lengths (Cor. 9 in Ref. [77]) translates into

$$\sum_{i=0}^n \binom{n-i}{2} (2i+2-n) \tilde{a}_i[\rho] \geq 0 \quad (\text{D13})$$

for all n -qubit states ρ . For example, inserting $n = 3$ into Ineq. (D13) yields $\tilde{a}_1[\rho] \geq 3\tilde{a}_0[\rho]$ which is a far-from-obvious fact about two-copy Bell sampling experiments. Finally, the fact that the GHZ state maximizes n -body correlations [78, 182],

$$0 \leq A_n[\rho] \leq A_n[\Psi_{\text{GHZ}}] = 2^{n-1} + \delta_{n,\text{even}} \quad (\text{D14})$$

also translates into a bound on linear combinations of triplet probabilities.

Let us conclude this section with a discussion about the polytopes of admissible QWEs for $n = 2$ qubits, see Fig. 7. It was shown in Ref. [77] that a putative SLD $\mathbf{a} = (a_0, a_1, a_2)$ can be physically realized (i.e., $\mathbf{a} = \mathbf{a}[\rho]$ for some 2-qubit state ρ) iff $\mathbf{a} \in \mathbb{R}^3$ is contained in the convex hull of

$$\mathbf{a} [|\Phi^+\rangle\langle\Phi^+|] = \frac{1}{4}(1, 0, 3), \quad (\text{D15})$$

$$\mathbf{a} [|0,0\rangle\langle 0,0|] = \frac{1}{4}(1, 2, 1), \quad (\text{D16})$$

$$\mathbf{a} [|0\rangle\langle 0| \otimes \frac{\mathbb{1}}{2}] = \frac{1}{4}(1, 1, 0), \quad (\text{D17})$$

$$\text{and } \mathbf{a} \left[\frac{\mathbb{1}}{4} \right] = \frac{1}{4}(1, 0, 0). \quad (\text{D18})$$

In Fig. 7, we depict (without any loss of information a two-dimensional projection of) the resulting sector length polytope (pink). By applying the basis change matrices T' and

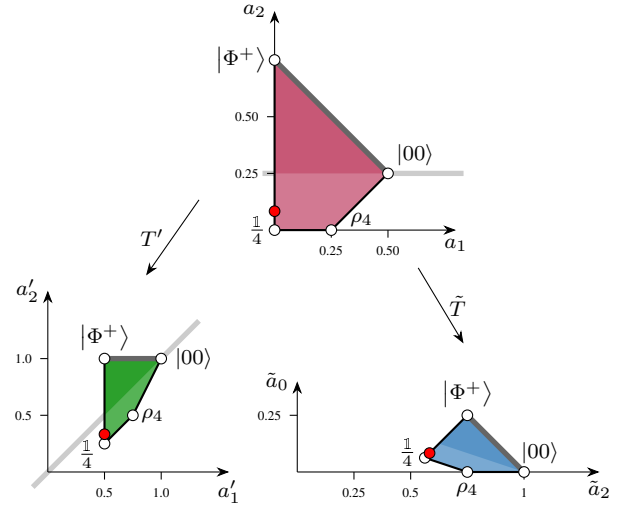


FIG. 7. 2D projection of 3D polytopes of admissible QWEs for $n = 2$ qubits. SLDs (pink) were characterized in Ref. [77] and the admissible APDs (green) and TPDs (blue) follow via the transforms T' and \tilde{T} from Fig. 1. Each polytope is the convex hull of four vectors of QWEs for the states $|\Phi^+\rangle\langle\Phi^+|$, $|0,0\rangle\langle 0,0|$, $\mathbb{1}/4$, and $\rho_4 = |0,0\rangle\langle 0,0| + |0,1\rangle\langle 0,1|$. The thickened boundary lines precisely correspond to pure states. In darker regions, all states are entangled. However, also in lighter regions, entangled states do exist, e.g., the Werner state [183] $(\frac{1}{3} + \epsilon) |\Phi^+\rangle\langle\Phi^+| + (\frac{2}{3} - \epsilon) \frac{\mathbb{1}}{4}$ (red dot $\epsilon \approx 0$) is NPT entangled for every $\epsilon > 0$ [166].

\tilde{T} from Fig. 1, we convert the SLD polytope into the corresponding polytopes of admissible 2-qubit averaged purity distributions (green) and triplet probability distributions (blue). In each basis, we have available one entanglement criterion [recall Eqs. (14), (32), and (80)], namely

- $a_2[\rho] > \frac{1}{4} \implies \rho$ entangled (n -body sector length),
- $a'_2[\rho] > a'_1[\rho] \implies \rho$ entangled (purity), and
- $\tilde{a}_2[\rho] > 1 - 3\tilde{a}_0[\rho] \implies \rho$ entangled (concurrence).

We highlight the regions of definitively-entangled states with a darker haze in Fig. 7. Coincidentally, all three criteria are equivalent in the present case of $n = 2$ qubits. For $n \geq 3$, on the other hand, Fig. 6 from the main text clearly shows that the three entanglement criteria are no longer equivalent. Finally, note that also for $n = 3$ qubits, the set of admissible QWEs is known to be a polytope (the convex hull of seven four-dimensional vectors) [77] while it is a grand open challenge to fully characterize the admissible sets of SLDs, APDs, and TPDs in the general case of $n \geq 4$ qubits.

Appendix E: 6-qubit AME state with only 7 CNOTs

In this short appendix, we present a novel quantum circuit, see Fig. 9, for preparing a six-qubit state Ψ_{AME} with the property $a_1[\Psi_{\text{AME}}] = a_2[\Psi_{\text{AME}}] = a_3[\Psi_{\text{AME}}] = 0$, i.e., Ψ_{AME} is a 3-uniform state and hence ($n = 6$) absolutely maximally entangled (AME). Other circuits for preparing such AME states

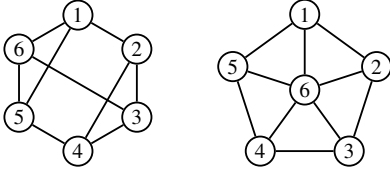


FIG. 8. Realizations of six-qubit AME states as graph states with 9 (left) and 10 (right) edges, respectively.

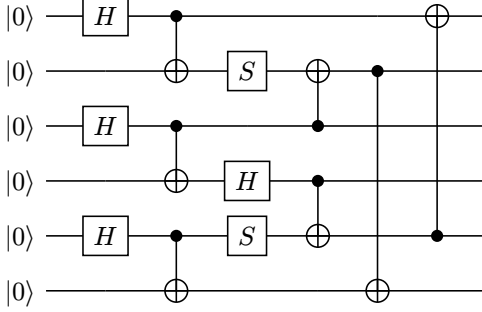


FIG. 9. Preparation circuit for a six-qubit absolutely maximally entangled state. This circuit requires fewer CNOT gates than the naive graph state preparation circuits from Fig. 8.

were known before, e.g., for the [cylinder graph state](#) and the [wheel graph state](#) on six qubits, whose graphs are displayed on the left and right of Fig. 8, respectively. However, in the graph state paradigm, the number of edges (here 9 and 10) is precisely equal to the number of two-qubit gates in the corresponding preparation circuit. We can do better by leaving the graph state paradigm. Via a randomized search over low-depth Clifford circuits, see Ref. [184] for details, we discover an AME state that can be prepared with only seven two-qubit gates, see Fig. 9. To our knowledge this reduces the CNOT cost of the best AME state preparation circuit from 9 to 7. This is also the circuit that we used in our experimental demonstration presented in Sec. IV A from the main text.

Appendix F: Superpositions versus mixtures

Here we showcase how superpositions and mixtures may differently manifest themselves in the three distributions of QWEs. For concreteness, we consider the following two families of parameterized n -qubit states. First, a superposition state $\Psi_{\text{sup}}(p) = |\psi(p)\rangle\langle\psi(p)|$ with state vector

$$|\psi(p)\rangle = \sqrt{p}|0\rangle^{\otimes n} + \sqrt{1-p}|1\rangle^{\otimes n} \quad (\text{F1})$$

and second, the corresponding incoherent mixture

$$\rho_{\text{mix}}(p) = p|0\rangle\langle 0|^{\otimes n} + (1-p)|1\rangle\langle 1|^{\otimes n}. \quad (\text{F2})$$

Note that $|\psi(1-2/n)\rangle$ recently appeared as a logical state of an $[[n, 1, 2]]$ code that was used to construct a family of $[[n, k, d]]$ QECCs (for every $k, d = \text{const}$), which have logical

states with vanishingly small geometric entanglement in the limit of large n [185]. This is surprising because, under very mild assumptions, logical states are highly entangled [185].

By symmetry (QWEs are local-unitary invariants), we can assume $0 \leq p \leq 0.5$ without loss of generality. Then, $\Psi_{\text{sup}}(p)$ is entangled for all values of $p \neq 0$ whereas $\rho_{\text{mix}}(p)$ is always fully separable. This form of entanglement is a global property as both states share exactly the same marginals and, in consequence, the same (averaged) subsystem purities

$$a'_i[\Psi_{\text{sup}}(p)] = a'_i[\rho_{\text{mix}}(p)] = 1 - 2p(1-p) \quad (\text{F3})$$

for $0 < i < n$. Note that $a'_0[\Psi_{\text{sup}}(p)] = a'_0[\rho_{\text{mix}}(p)] = 1$ by normalization. The only difference that is thus captured by the APD are the global purities $a'_n[\Psi_{\text{sup}}(p)] = 1$ and $a'_n[\rho_{\text{mix}}(p)] = 1 - 2p(1-p)$, respectively. As discussed in the main text, we can convert APDs into SLDs and TPDs. We plot all of them for both parameterized states on $n = 20$ qubits in Fig. 10. The differences are subtle but clearly visible.

Let us first discuss the sector length distributions (pink), which are displayed in the left panel of Fig. 10. They look mostly the same for $\Psi_{\text{sup}}(p)$ and $\rho_{\text{mix}}(p)$. In fact, they precisely coincide in all entries except for the last—a property inherited from their APDs [Eq. (F3)] because T'^{-1} [Eq. (30)] is a lower-triangular matrix. For $p = 0$, we still have $\Psi_{\text{sup}}(0) = \rho_{\text{mix}}(0)$ and the SLD is given by the symmetrical binomial distribution—the SLD unique to pure product states [Eq. (13)]. As we increase p , we see that $\mathbf{a}[\Psi_{\text{sup}}(p)]$ continuously changes until the SLD

$$a_i[\Psi_{\text{GHZ}}] = \frac{1}{2^n} \binom{n}{i} \delta_{i,\text{even}} + \frac{1}{2} \delta_{i,n} \quad (\text{F4})$$

of the GHZ state $\Psi_{\text{GHZ}} = \Psi_{\text{sup}}(p = 0.5)$ is reached [86]. Similarly, the odd components of $\mathbf{a}[\rho_{\text{mix}}(p)]$ converge to zero until the SLD

$$a_i[\rho_{\text{rep}}] = \frac{1}{2^n} \binom{n}{i} \delta_{i,\text{even}} \quad (\text{F5})$$

of the maximally mixed state $\rho_{\text{rep}} = \frac{1}{2}|0\rangle\langle 0|^{\otimes n} + \frac{1}{2}|1\rangle\langle 1|^{\otimes n}$ within the n -qubit repetition code space is reached. Note that $\Psi_{\text{sup}}(p)$ lies within this subspace too. We analytically find (assuming n is even)

$$a_n[\Psi_{\text{sup}}(p)] = \frac{1}{2^n} + 2p(1-p) \quad \text{and} \quad (\text{F6})$$

$$a_n[\rho_{\text{mix}}(p)] = \frac{1}{2^n}. \quad (\text{F7})$$

Therefore, the n -body sector length criterion [Eq. (14)] identifies $\Psi_{\text{sup}}(p)$ as entangled for all values of $p \in (0, 0.5]$ while $a_n[\rho_{\text{mix}}(p)]$ is as large as possible given the fact that $\rho_{\text{mix}}(p)$ is a separable state. Finally, note that the GHZ state maximizes the n -body sector length among all n -qubit states [78, 182].

Next, consider the central panel of Fig. 10, where we have plotted the averaged purity distributions (APDs). As mentioned above, the APDs (green) coincide except for $a'_n[\Psi_{\text{sup}}(p)] = 1$ and $a'_n[\rho_{\text{mix}}(p)] = 1 - 2p(1-p)$. Hence, also the purity criterion [Eq. (32)] detects entanglement in $\Psi_{\text{sup}}(p)$

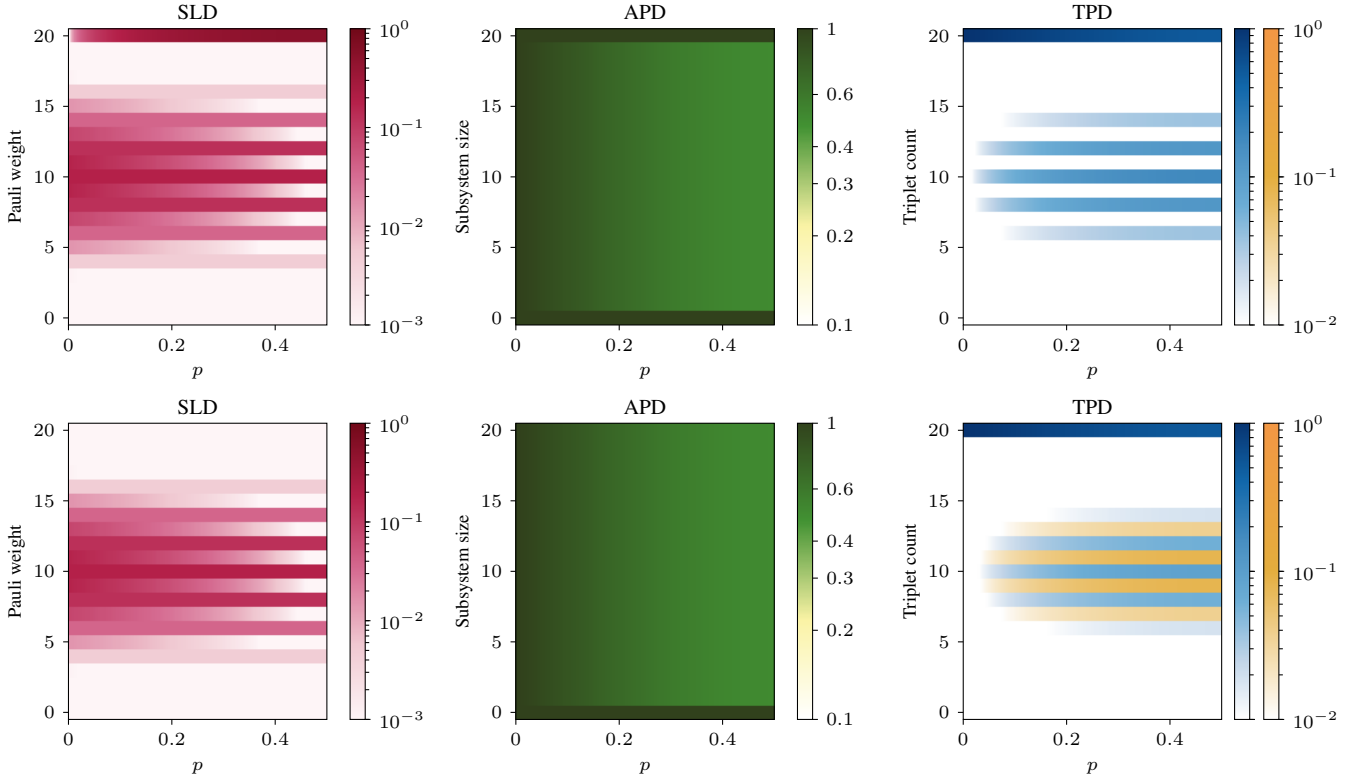


FIG. 10. QWEs for a parameterized superposition (top) and mixture (bottom) of $|0\rangle^{\otimes n}$ and $|1\rangle^{\otimes n}$ for $n = 20$ qubits. See Eqs. (F1) and (F2) for precise definitions. Vertical slices through the plots (rotated by 90° to the right) correspond to QWE distributions of a given state, similar to Fig. 3 from the main text. The three distributions show the same information in different vector space bases of \mathbb{R}^{n+1} as discussed in Fig. 1 of the main text.

for all values of $p \in (0, 0.5]$ while $\rho_{\text{mix}}(p)$ again only meets the separability bound without surpassing it.

Last but not least, the triplet probability distributions are shown in the right panel of Fig. 10. Here, we use blue and yellow colors to distinguish the cases of even and odd singlets, respectively. In other words, we are—strictly speaking—depicting the dual TPD $\tilde{\mathbf{b}}$ rather than the TPD $\tilde{\mathbf{a}}$ itself. Recall that the two are related via $\tilde{b}_i[\rho] = (-1)^{n-i}\tilde{a}_i[\rho]$ for all n -qubit states ρ , i.e., by Eq. (78) we can always write $\text{Tr}[\rho^2] = \sum_i \tilde{b}_i[\rho]$. Consistently, we only find yellow stripes emerging in the plot of $\rho_{\text{mix}}(p)$ but not for $\Psi_{\text{sup}}(p)$ as the former becomes increasingly mixed as p grows whereas the latter remains pure. Also here (in the TPD picture), the QWEs of the two parameterized states otherwise show similar features. For $p = 0$, both TPDs are completely concentrated in the all-triplet bin, i.e., $\tilde{a}_i[\Psi_{\text{sup}}(0)] = \tilde{a}_i[\rho_{\text{mix}}(0)] = \delta_{i,n}$ as the hallmark of pure product states. As p is increased, this probability is redistributed into the other bins—indicating mixedness. For $\Psi_{\text{sup}}(p)$, this mixedness is only found in the marginals, thus certifying entanglement. For $\rho_{\text{mix}}(p)$, the mixedness has nothing to do with entanglement. Indeed, we analytically find (assuming n is even)

$$\tilde{a}_n[\Psi_{\text{sup}}(p)] = 1 - 2p(1-p) \left(1 - \frac{2}{2^n}\right), \quad (\text{F8})$$

yielding the concurrence $C[\Psi_{\text{sup}}(p)] = 1 - \tilde{a}_n[\Psi_{\text{sup}}(p)]$, as

well as

$$\tilde{a}_n[\rho_{\text{mix}}(p)] = 1 - 2p(1-p) \left(1 - \frac{1}{2^n}\right). \quad (\text{F9})$$

From this follows that the concurrence $C[\Psi_{\text{sup}}(p)] > 0$ certifies entanglement for $p \in (0, 0.5]$ while the lower bound on $C[\rho_{\text{mix}}(p)]$ from Eq. (82) is identically equal to zero. Similarly, we find (if n is even)

$$\tilde{a}_0[\Psi_{\text{sup}}(p)] = \frac{4p(1-p)}{2^n}, \quad (\text{F10})$$

which yields the n -tangle $\text{Tr}[\Psi_{\text{sup}}(p)\tilde{\Psi}_{\text{sup}}(p)] = 4p(1-p)$. Unsurprisingly, the latter reaches its maximal possible value for $p = 0.5$. For completeness, we remark

$$\tilde{a}_0[\rho_{\text{mix}}(p)] = \frac{2p(1-p)}{2^n}, \quad (\text{F11})$$

however, as the state is mixed, Eq. (F11) does not carry the interpretation of the rescaled n -tangle here.

Appendix G: QWEs of many-qubit states

In this appendix, we present and discuss various illustrative examples for the three distributions of quantum weight enumerators (QWEs). These are: (i) Shor-Laflamme QWEs aka

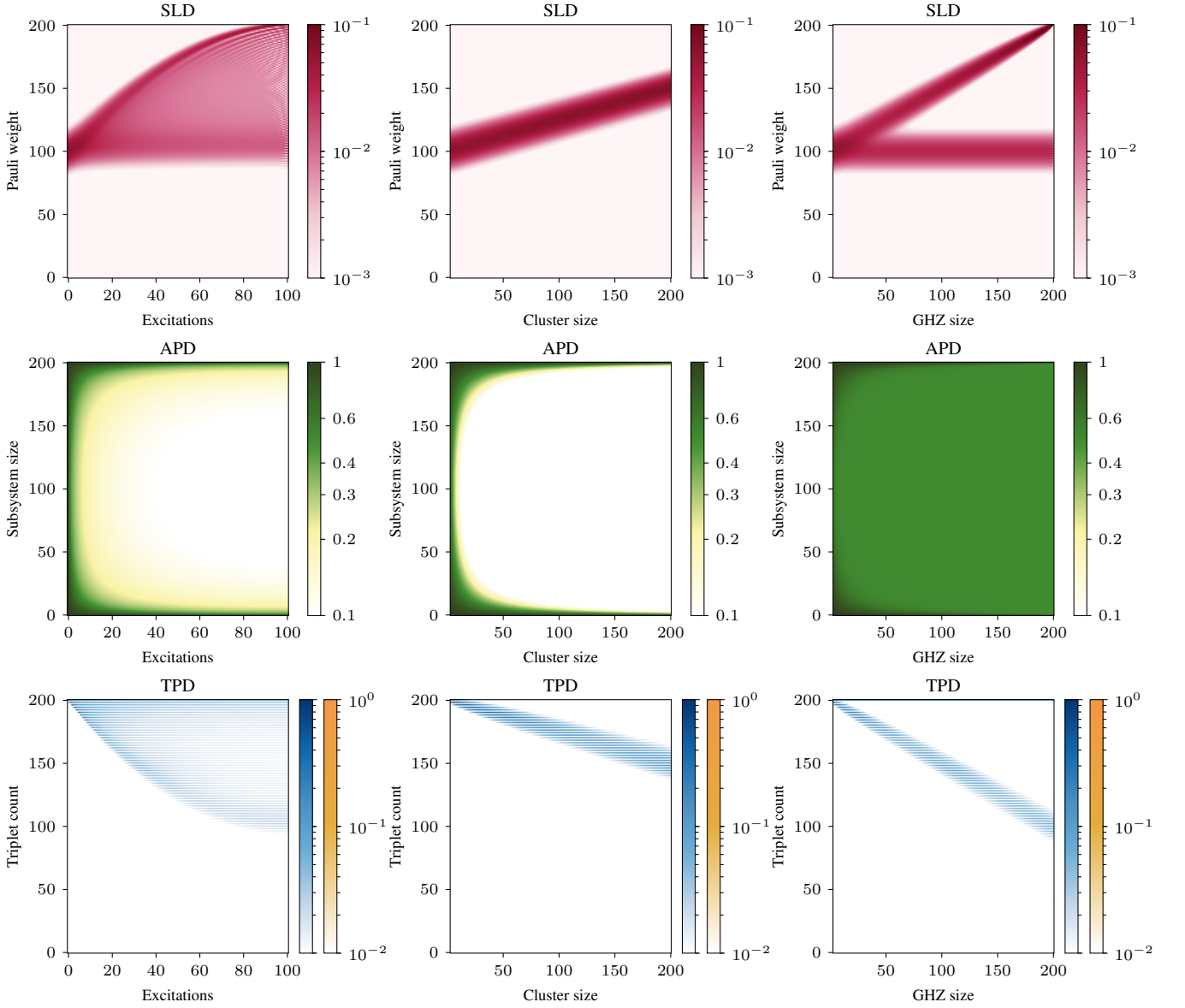


FIG. 11. Quantum weight enumerators of noiseless parameterized states defined in Eqs. (G1)—(G2) on $n = 200$ qubits. Shown are Shor-Laflamme distributions (top, pink), averaged purity distributions (center, green), and triplet probability distributions (bottom, blue). On the y -axis of each panel, the index i in the entry of the respective distributions [recall Defs. (10), (28), and (37)] is varied. On the x -axis, we vary the parameter e from Eqs. (G1)—(G3). This figure illustrates that QWEs can capture various distinct entanglement features of QWEs.

sector lengths, which stratify the purity by Pauli weight; (ii) Rains' unitary QWEs aka averaged purities; and (iii) Rains' shadow QWEs aka triplet probabilities. Specifically, we consider the following three families of quantum state vectors

$$|D_e^n\rangle = \frac{1}{\sqrt{\binom{n}{e}}} \sum_{|\mathbf{x}|=e} |\mathbf{x}\rangle, \quad (\text{G1})$$

$$|\text{GHZ}^e, \mathbf{0}^{n-e}\rangle = \left(\frac{|0\rangle^{\otimes e} + |1\rangle^{\otimes e}}{\sqrt{2}} \right) \otimes |0\rangle^{\otimes n-e}, \quad (\text{G2})$$

$$\text{and } |\text{Cycle}^e, +^{n-e}\rangle = \prod_{s=1}^e \text{CZ}_{s, s+1 \bmod e} |+\rangle^{\otimes n}. \quad (\text{G3})$$

Each state family is parameterized by an integer e . For Dicke state vectors $|D_e^n\rangle$, this integer is the number of excitations, which we vary from $e = 0$ to $e = n/2$. Further increasing e would not lead to any new QWEs as $|D_e^n\rangle$ is local unitary equivalent to $|D_{n-e}^n\rangle = X^{\otimes n} |D_e^n\rangle$. From GHZ and cycle graph states with e entangled qubits, meanwhile, we construct families of n -qubit states by simply appending $n - e$ qubits in a pure product state.

For $|D_e^n\rangle$ and $|\text{GHZ}^e\rangle$, we already know the QWEs from Eqs. (112) and (F4), respectively. Similarly, those of $|\text{Cycle}^e\rangle$ were computed in Eq. (21) of Ref. [87]. Leveraging the con-

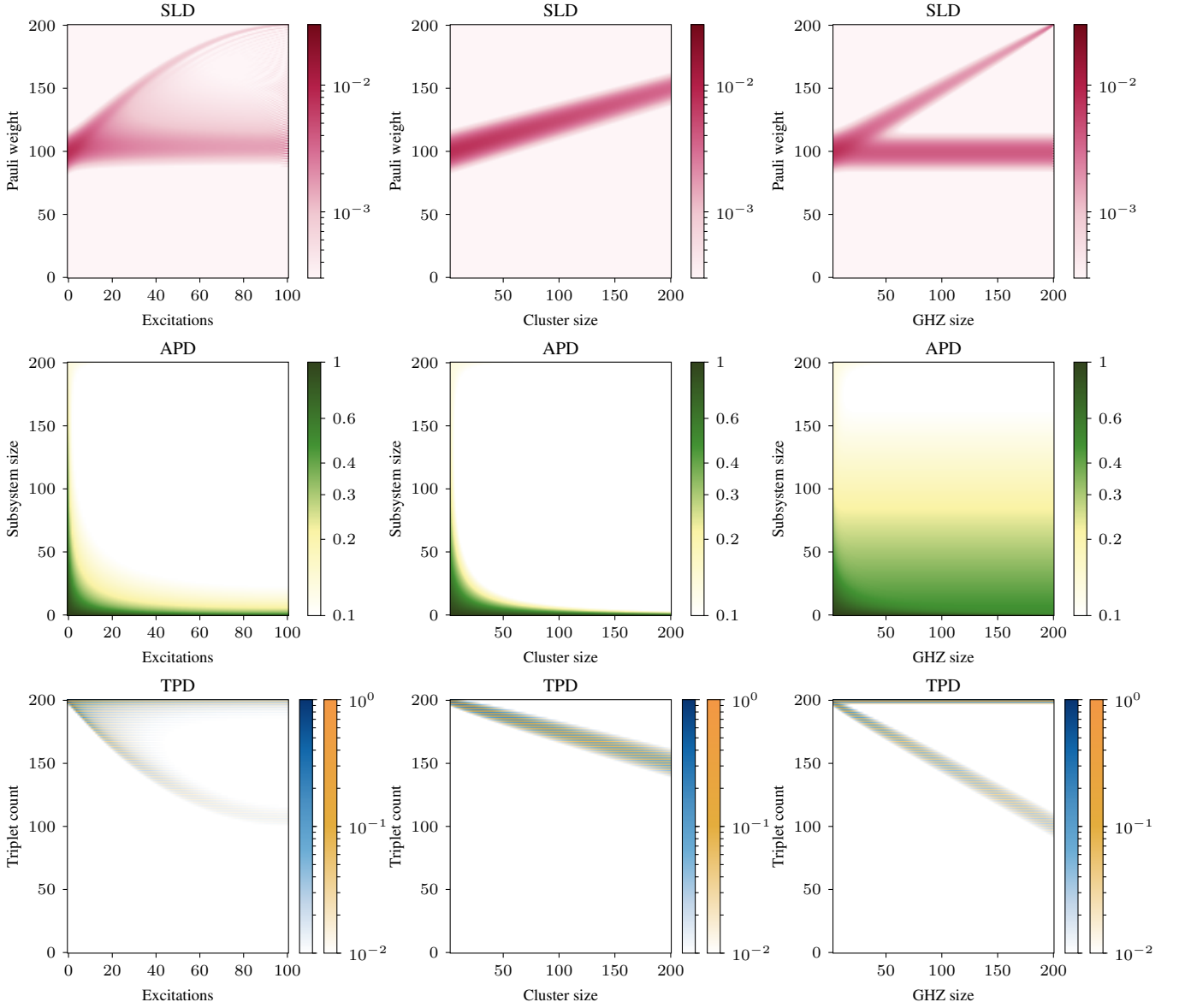


FIG. 12. Same as Fig. 11 but with local depolarizing noise of strength $p = 0.01$ on every qubit. Due to the noise, we find non-zero triplet probabilities $\tilde{a}_{n-j}[\rho] > 0$ [Eq. (77)] for odd numbers j of singlets (yellow). This figure illustrates that many QWE entanglement features observed in Fig. 11 are stable under small noise.

volution [77]

$$a_j[\rho \otimes \sigma] = \sum_{i=0}^j a_i[\rho] a_{j-i}[\sigma], \quad (\text{G4})$$

together with Eq. (13) from the main text, we can thus compute the SLDs of $|\text{GHZ}^e, \mathbf{0}^{n-e}\rangle$ and $|\text{Cycle}^e, +^{n-e}\rangle$. This then allows us to calculate the respective APDs and TPDs by applying the transforms T' and \tilde{T} from App. A.

In Fig. 11, we display all QWEs for the three discussed state families in the case of $n = 200$ qubits. In the (pink) picture of sector length distributions (SLDs), we see that increasing e causes a movement of the SLDs mean value from $n/2$ towards sectors of larger Pauli weight. Thereby, distinct fea-

tures manifest themselves, depending on the state family. This observation is consistent with the fact that, for pure states, the mean value of the SLD must lie in the range between $n/2$ and $3n/4$ [87].

For Dicke states, we see in the top left panel of Fig. 11 that a significant proportion of the SLD remains around $n/2$ for all values of e . Meanwhile, a second peak emerges. By increasing e , this peak gives rise to a curved ridge that deeply extends into the high-weight sector until full Pauli weight is reached around $e = n/2$. The region between this curved ridge and the one at Pauli weight $n/2$ is significantly occupied by the SLD. Towards larger values of e , an interference-like pattern arises in this region. Precisely at half-filling, the odd-weight sector lengths “destructively interfere” in the sense that we observe

$a_i[|D_{n/2}^n\rangle\langle D_{n/2}^n|] = 0$ for all odd values of i . We explain the latter observation as follows: the half-filled Dicke state is invariant under the state inversion map [Eq. (34)]. Therefore, TPD [Eq. (37)] and dual SLD [Eq. (11)] coincide with each other and, since the state is pure, also with the SLD. This also explains the subtle feature that, for $e = n/2$, SLD (pink) and TPD (blue) of the Dicke state are exactly the same.

The second state family, cycle graph states $|\text{Cycle}^e, +^{n-e}\rangle$, shows a different behavior in the top central panel of Fig. 11. Here, the SLD only features a single peak, whose center moves from $n/2$ for $e = 0$ entangled qubits to $3n/4$ for $e = 200$. At the same time, the width of the peak slightly decreases. This is explained as follows: for $e = 0$, we have a pure product state, whose SLD is a symmetric binomial distribution [Eq. (13)]. For $e > 0$, the SLD of $|\text{Cycle}^e\rangle$ is strikingly similar to that of a random state [87], which is very close to an asymmetric binomial distribution centered at $3e/4$ [Eq. (109)]. Note that, for graph states, mean and variance of the SLD can always be expressed in terms of the numbers of isolated vertices I , leaves L , and twin pairs T of the corresponding graph, see Cor. 3 of Ref. [87]. Here, these invariants are given by $I = n - e$, $L = 0$, and $T = \binom{n-e}{2} + 2\delta_{e,4}$, which implies that mean and variance of the SLD are given by $(2n + e)/4$ and $(4n - e + 4\delta_{e,4})/16$, respectively. This explains the position and width of the ray in the of central panel of Fig. 11 as a function of e .

Finally, consider in the top right panel of Fig. 11 the SLD for the third state family: GHZ states in a tensor product with pure product states. Here, we observe qualitatively different features compared to the already-discussed state families. Similar to the case of Dicke states, we see two ridges in the SLD: again a horizontal one at Pauli weight $n/2$, and a second one that increases from weight $n/2$ at $e = 0$ to weight n at $e = n$. This time, however, the second ridge is straight (not curved) and there are no interference pattern between the two ridges. The reason for the observed pattern is this: from Eq. (F4), we know that the SLD of $|\text{GHZ}^e\rangle$ arises from the symmetrical binomial distribution $\binom{e}{i}/2^e$ after redistributing all odd-weight sector lengths into the weight- e bin. Convoluting with the ordinary binomial distribution $\binom{n-e}{j}/2^{n-e}$ via Eq. (G4) smears out both the centered distribution as well as the peak at e , resulting in the observed pattern. We also point out that at the very right of the SLD (just as in the case of Dicke states), all odd-weight sector lengths vanish, which again causes the curious feature that that, for $e = n$, SLD (pink) and TPD (blue) of $|\text{GHZ}^n\rangle$ precisely coincide.

Let us next turn our attention to the (green) averaged purity distributions (APDs) in Fig. 11. In general, we observe the following pattern: when the size $|S|$ of the subsystems S whose purities $\text{Tr}[\rho_S^2]$ are averaged [Eq. (28)] is decreased from $|S| = n$, the value of the APD decreases from 1 until, at $|S| = n/2$, it starts to increase again, which results in a symmetric pattern with a horizontal symmetry axis. The symmetry is easily explained by the fact that—by virtue of the Schmidt decomposition or, alternatively, by MacWilliams' identity—for pure states, a marginal has the same purity as its complement. The decrease of the APD value with decreasing $|S|$ reflect that fact the global state is pure and (if $e > 0$) en-

tangled. Therefore, some of its marginals are mixed, which causes the drop in the APD. Quantitatively, however, we can easily distinguish the three state families: the GHZ state (center right) has fairly pure marginals, which are only mixtures of $|0\rangle$ and $|1\rangle$; taking the tensor product with the pure state $|0\rangle^{n-e}$ only increases the subsystem purity, which is visible as a dark green shade in the top and bottom left corner of the APD panel of the GHZ state. For Dicke states (center left), the values of the APD become significantly smaller than for the GHZ states, showcasing in which sense Dicke states can be regarded as more entangled than GHZ states. For cycle graph states (center) the APD drops to even smaller values, which is unsurprising because generic states have exponentially small subsystem purities.

Last but not least, consider the (blue) triplet probability distributions (TPDs) in bottom of Fig. 11. These are the QWEs that can be straightforwardly measured in two-copy Bell sampling experiments. For all three state families, we see that for $e = 0$ the zero-singlet probability is equal to 100%. When e is increased, the probabilities of measuring more than zero singlets increases, however, only for even singlet counts. Moreover, all TPDs concentrate in the upper half (low singlet count) of their respective panels. The fact that odd-singlet counts are never observed is easily attributed to the fact that the global state is always pure [Eq. (78)]. Moreover, the occurrence of non-zero singlet counts is due to entanglement in the states for $e > 0$. This entanglement can also be quantified in terms of the concurrence [Eq. (81)].

Looking more closely at the TPDs in the bottom of Fig. 11, we see that Dicke states have non-zero probabilities for all triplet counts above $n - e$. For large e , the TPD of Dicke states (bottom left) has a heavy tail in the center of the distribution at $n/2$ triplets. Similarly, for $|\text{GHZ}^e, \mathbf{0}^{n-e}\rangle$ (bottom right), we observe one ray that extends down to $n/2$ triplets; a second (less visible) horizontal ray (supporting half the TPD) remains in the zero-singlet bin. On the other hand, for $|\text{Cycle}^e, +^{n-e}\rangle$, the TPD panel (bottom center) only features a single ray that connects n triplets for $e = 0$ and $3n/4$ triplets for $e = n$. The observed fact that the TPDs of the Dicke and GHZ states exhibit heavy tails around $n/2$ triplets, while those of the cluster state do not, explains the sample requirements discussed in Fig. 5 of the main text.

Besides Fig. 11, where we show the QWEs of ideal states, we also show those of slightly-perturbed states in Fig. 12. This time, we apply $p = 0.01$ of local depolarizing noise per qubit. The QWEs of the noise states are computed as explained in Sec. VI of the main text. We see that many of the entanglement features that we just discussed survive in the presence of small noise. In particular, the SLD features (pink) qualitatively remain the same. This is unsurprising because local depolarizing noise acts diagonally on SLDs [Eq. (15)].

Appendix H: Operator norms of QWE transformations

In Lemma 6 of the main text, we have analytically computed the operator norms of the $2n$ -qubit observables W_i, W'_i , and \tilde{W}_i , which are all highly degenerate. Indeed, in Sec. III,

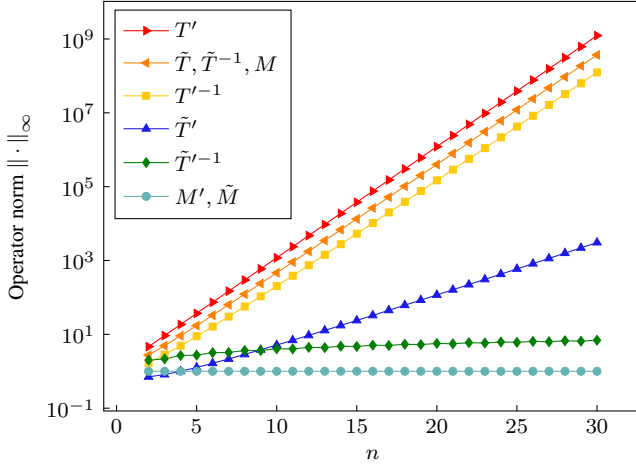


FIG. 13. Operator norms of the linear maps acting on \mathbb{R}^{n+1} from Fig. 1 as a function of the number of qubits. Except for \tilde{T}'^{-1} , M' , and \tilde{M} , all norms are growing exponentially. Hence, in general, one has to work with an increased numerical precision when transforming between QWEs.

we have shown that these operators are diagonal in the basis of Bell pairs $|\alpha\rangle$ [Eq. (54)] and that their eigenvalues only depend on the number of singlets in $|\alpha\rangle$ but not on their position within $|\alpha\rangle$. The core of the efficiency of the quantum weight enumerator machinery is to lift this degeneracy by replacing W_0, \dots, W_n and W'_0, \dots, W'_n with T^{-1} and T'^{-1} , respectively. In the process, the operator norms do not remain the same. In Fig. 13, we show the operator norms of \tilde{T}'^{-1} and \tilde{T}'^{-1} alongside those of the other transformations from Fig. 1. We see that $\|\tilde{T}'^{-1}\|_\infty$ (red) grows exponentially while $\|\tilde{T}'^{-1}\|_\infty$ (dark green) increases polynomially. This is easily explained as the behavior inherited by their corresponding $2n$ -qubit observables. Note that we have strong numerical evidence for $\|\tilde{T}'^{-1}\|_\infty \lesssim 1.25\sqrt{n}$. Concerning the other transformations, we see that the exponentially-growing operator norms of \tilde{T} , \tilde{T}^{-1} , and M all coincide (orange) as these matrices arise from each other through multiplication of \tilde{M} . The worst operator norm is that of T' (red), which transforms SLDs into APDs. Also that of \tilde{T}' (blue) grows exponentially albeit less quickly. Finally, we see $\|M'\|_\infty = \|\tilde{M}\|_\infty = 1$ (bright green) as these are the bases where it is obvious that MacWilliams' transformation is an involution of \mathbb{R}^{n+1} .

- [1] D. A. Lidar and T. A. Brun, *Quantum Error Correction* (Cambridge University Press, 2013).
- [2] B. M. Terhal, *Rev. Mod. Phys.* **87**, 307 (2015).
- [3] E. T. Campbell, B. M. Terhal, and C. Vuillot, *Nature* **549**, 172 (2017).
- [4] A. Bermudez, X. Xu, R. Nigmatullin, J. O'Gorman, V. Negnevitsky, P. Schindler, T. Monz, U. G. Poschinger, C. Hempel, J. Home, F. Schmidt-Kaler, M. Biercuk, R. Blatt, S. Benjamin, and M. Müller, *Phys. Rev. X* **7**, 041061 (2017).
- [5] L. Egan, D. M. Debroy, C. Noel, A. Risinger, D. Zhu, D. Biswas, M. Newman, M. Li, K. R. Brown, M. Cetina, and C. Monroe, *Nature* **598**, 281 (2021).
- [6] C. Ryan-Anderson, J. G. Bohnet, K. Lee, D. Gresh, A. Hankin, *et al.*, *Phys. Rev. X* **11**, 041058 (2021).
- [7] S. Krinner, N. Lacroix, A. Remm, A. D. Paolo, E. Genois, *et al.*, *Nature* **605**, 669 (2022).
- [8] Google Quantum AI, *Nature* **614**, 676 (2023).
- [9] R. S. Gupta, N. Sundaresan, T. Alexander, C. J. Wood, S. T. Merkel, *et al.*, *Nature* **625**, 259 (2024).
- [10] D. Bluvstein, S. J. Evered, A. A. Geim, S. H. Li, H. Zhou, *et al.*, *Nature* **626**, 58 (2024).
- [11] R. Acharya, L. Aghababaie-Beni, I. Aleiner, T. I. Andersen, M. Ansmann, *et al.*, "Quantum error correction below the surface code threshold," (2024), arXiv:2408.13687 [quant-ph].
- [12] J. Emerson, R. Alicki, and K. Życzkowski, *Journal of Optics B: Quantum and Semiclassical Optics* **7**, S347 (2005).
- [13] J. Eisert, D. Hangleiter, N. Walk, I. Roth, D. Markham, R. Parekh, U. Chabaud, and E. Kashefi, *Nature Reviews Physics* **2**, 382–390 (2020).
- [14] M. Kliesch and I. Roth, *PRX Quantum* **2**, 010201 (2021).
- [15] J. Helsen, I. Roth, E. Onorati, A. Werner, and J. Eisert, *PRX Quantum* **3**, 020357 (2022).
- [16] S. T. Flammia and Y.-K. Liu, *Phys. Rev. Lett.* **106**, 230501 (2011).
- [17] G. J. Mooney, G. A. L. White, C. D. Hill, and L. C. L. Hollenberg, *J. Phys. Commun.* **5**, 095004 (2021).
- [18] S. A. Moses, C. H. Baldwin, M. S. Allman, R. Ancona, L. Ascarrunz, *et al.*, *Phys. Rev. X* **13**, 041052 (2023).
- [19] J. F. Kam, H. Kang, C. D. Hill, G. J. Mooney, and L. C. L. Hollenberg, *Phys. Rev. Res.* **6**, 033155 (2024).
- [20] D. Hangleiter and J. Eisert, *Rev. Mod. Phys.* **95**, 035001 (2023).
- [21] M. Ohliger, V. Nesme, and J. Eisert, *New J. Phys.* **15**, 015024 (2013).
- [22] S. Aaronson, in *Proceedings of the 50th Annual ACM SIGACT Symposium on Theory of Computing*, STOC 2018 (Association for Computing Machinery, New York, NY, USA, 2018) p. 325–338.
- [23] H.-Y. Huang, R. Kueng, and J. Preskill, *Nature Phys.* **16**, 1050 (2020).
- [24] A. Elben, S. T. Flammia, H.-Y. Huang, R. Kueng, J. Preskill, B. Vermersch, and P. Zoller, *Nature Rev. Phys.* **5**, 9 (2023).
- [25] L. E. Fischer, T. Dao, I. Tavernelli, and F. Tacchino, *Phys. Rev. A* **109**, 062415 (2024).
- [26] A. Montanaro, "Learning stabilizer states by Bell sampling," (2017), arXiv:1707.04012.
- [27] S. Chen, J. Cotler, H.-Y. Huang, and J. Li, in *2021 IEEE 62nd Annual Symposium on Foundations of Computer Science (FOCS)* (2022) pp. 574–585.
- [28] H.-Y. Huang, M. Broughton, J. Cotler, S. Chen, J. Li, M. Mohseni, H. Neven, R. Babbush, R. Kueng, J. Preskill, and J. R. McClean, *Science* **376**, 1182 (2022).
- [29] D. Aharonov, J. Cotler, and X.-L. Qi, *Nature Comm.* **13**, 887 (2022).
- [30] S. Chen, J. Cotler, H.-Y. Huang, and J. Li, "A hierarchy for replica quantum advantage," (2021), arXiv:2111.05874.
- [31] R. King, D. Gosset, R. Kothari, and R. Babbush, "Triply efficient shadow tomography," (2024), arXiv:2404.19211.

- [32] H.-Y. Huang, R. Kueng, and J. Preskill, *Phys. Rev. Lett.* **126**, 190505 (2021).
- [33] S. Scali, C. Umeano, and O. Kyriienko, *APL Quantum* **1** (2024), 10.1063/5.0209201.
- [34] D. Hangleiter and M. J. Gullans, *Phys. Rev. Lett.* **133**, 020601 (2024).
- [35] D. Gross, S. Nezami, and M. Walter, *Commun. Math. Phys.* **385**, 1325 (2021).
- [36] T. Haug and M. Kim, *PRX Quantum* **4**, 010301 (2023).
- [37] L. Leone, S. F. E. Oliviero, and A. Hamma, *Quantum* **8**, 1361 (2024).
- [38] T. Haug, S. Lee, and M. S. Kim, *Phys. Rev. Lett.* **132**, 240602 (2024).
- [39] J. Cotler, S. Choi, A. Lukin, H. Gharibyan, T. Grover, M. E. Tai, M. Rispoli, R. Schittko, P. M. Preiss, A. M. Kaufman, M. Greiner, H. Pichler, and P. Hayden, *Phys. Rev. X* **9**, 031013 (2019).
- [40] B. Koczor, *Phys. Rev. X* **11**, 031057 (2021).
- [41] W. J. Huggins, S. McArdle, T. E. O’Brien, J. Lee, N. C. Rubin, S. Boixo, K. B. Whaley, R. Babbush, and J. R. McClean, *Phys. Rev. X* **11**, 041036 (2021).
- [42] H. Hakoshima, S. Endo, K. Yamamoto, Y. Matsuzaki, and N. Yoshioka, *Phys. Rev. Lett.* **133**, 080601 (2024).
- [43] C. Schmid et al., *Phys. Rev. Lett.* **101**, 260505 (2008).
- [44] R. Islam et al., *Nature* **528**, 77 (2015).
- [45] D. Bluvstein, H. Levine, G. Semeghini, T. T. Wang, S. Ebadi, et al., *Nature* **604**, 451 (2022).
- [46] P. W. Shor, *Phys. Rev. A* **52**, R2493 (1995).
- [47] R. Laflamme, C. Miquel, J. P. Paz, and W. H. Zurek, *Phys. Rev. Lett.* **77**, 198 (1996).
- [48] A. Steane, *Proc. R. Soc. Lond. A* **452**, 2551–2577 (1996).
- [49] A. M. Steane, *Phys. Rev. Lett.* **77**, 793 (1996).
- [50] E. Knill and R. Laflamme, *Phys. Rev. A* **55**, 900 (1997).
- [51] P. Shor and R. Laflamme, *Phys. Rev. Lett.* **78**, 1600 (1997).
- [52] A. Calderbank, E. Rains, P. Shor, and N. Sloane, *IEEE Trans. Inf. Th.* **44**, 1369 (1998).
- [53] E. Rains, *IEEE Trans. Inf. Th.* **44**, 1388 (1998).
- [54] E. Rains, *IEEE Trans. Inf. Th.* **45**, 2361 (1999).
- [55] A. Ashikhmin and S. Litsyu, *IEEE Trans. Inf. Th.* **45**, 1206 (1999).
- [56] A. Ashikhmin, A. Barg, E. Knill, and S. Litsyn, *IEEE Trans. Inf. Th.* **46**, 778 (2000).
- [57] F. J. MacWilliams, *The Bell System Tech. J.* **42**, 79 (1963).
- [58] A. M. Gleason, in *Actes du Congrès Internat. Math.*, Vol. 3 (Gauthier-Villars, Paris, 1970) pp. 211–215.
- [59] F. J. MacWilliams and N. J. A. Sloane, *The Theory of Error-Correcting Codes*, 2nd ed. (North-Holland Publishing Company, 1978).
- [60] V. S. Pless and W. C. Huffman, eds., *Handbook of coding theory* (Elsevier, Amsterdam, Netherlands, 1998).
- [61] G. Nebe, E. M. Rains, and N. J. A. Sloane, *Self-Dual Codes and Invariant Theory*, Algorithms and Computation in Mathematics, Vol. 17 (Springer, 2006).
- [62] M. Krawtchouk, *Comptes Rendus* **189**, 620 (1929).
- [63] A. Vardy, in *Proceedings of the twenty-ninth annual ACM symposium on Theory of computing* (1997) pp. 92–109.
- [64] C. Cao, M. J. Gullans, B. Lackey, and Z. Wang, *PRX Quantum* **5**, 030313 (2024).
- [65] C. Cao and B. Lackey, *IEEE Trans. Inf. Th.* **70**, 3512 (2024).
- [66] P. Braccia, P. Bermejo, L. Cincio, and M. Cerezo, “Computing exact moments of local random quantum circuits via tensor networks,” (2024), arXiv:2403.01706.
- [67] E. Kubischta, I. Teixeira, and J. M. Silvester, “Quantum weight enumerators for real codes with x and z exactly transversal,” (2024), arXiv:2306.12526.
- [68] S. Bravyi and M. B. Hastings, *Proc. of the 46th ACM Symp. Th. Comp. (STOC 2014)*, 273 (2014).
- [69] N. P. Breuckmann and J. N. Eberhardt, *PRX Quantum* **2**, 040101 (2021).
- [70] P. Panteleev and G. Kalachev, in *Proceedings of the 54th Annual ACM SIGACT Symposium on Theory of Computing*, STOC 2022 (Association for Computing Machinery, New York, NY, USA, 2022) p. 375–388.
- [71] A. Leverrier and G. Zémor, *IEEE Trans. Inf. Th.* **69**, 5100 (2023).
- [72] S. Bravyi, A. W. Cross, J. M. Gambetta, D. Maslov, P. Rall, and T. J. Yoder, *Nature* **627**, 778 (2024).
- [73] J. I. de Vicente and M. Huber, *Phys. Rev. A* **84**, 062306 (2011).
- [74] W. Laskowski, M. Markiewicz, T. Paterek, and M. Żukowski, *Phys. Rev. A* **84**, 062305 (2011).
- [75] C. Klöckl and M. Huber, *Phys. Rev. A* **91**, 042339 (2015).
- [76] S. Morelli, C. Eltschka, M. Huber, and J. Siewert, *Phys. Rev. A* **109**, 012423 (2024).
- [77] N. Wyderka and O. Gühne, *J. Phys. A* **53**, 345302 (2020).
- [78] C. Eltschka and J. Siewert, *Quantum* **4**, 229 (2020).
- [79] M. Miller and D. Miller, in *2021 IEEE International Conference on Quantum Computing and Engineering (QCE)* (2021) pp. 378–384.
- [80] Y. Quek, D. S. França, S. Khatri, J. J. Meyer, and J. Eisert, *Nature Phys.* (2022).
- [81] T. Schuster and N. Y. Yao, *Phys. Rev. Lett.* **131**, 160402 (2023).
- [82] B. M. Terhal, *Phys. Lett. A* **271**, 319 (2000).
- [83] O. Gühne, P. Hyllus, D. Bruß, A. Ekert, M. Lewenstein, C. Macchiavello, and A. Sanpera, *Phys. Rev. A* **66**, 062305 (2002).
- [84] M. Bourennane, M. Eibl, C. Kurtsiefer, S. Gaertner, H. Weinfurter, O. Gühne, P. Hyllus, D. Bruß, M. Lewenstein, and A. Sanpera, *Phys. Rev. Lett.* **92**, 087902 (2004).
- [85] O. Gühne and G. Tóth, *Phys. Rep.* **474**, 1 (2009).
- [86] H. Aschauer, J. Calsamiglia, M. Hein, and H. J. Briegel, *Quantum Inf. Comput.* **4**, 383 (2004).
- [87] D. Miller, D. Loss, I. Tavernelli, H. Kampermann, D. Bruß, and N. Wyderka, *J. Phys. A* **56**, 335303 (2023).
- [88] Both Eqs. (21) and (40) are special cases of the following fact. Let $P \in \{I, X, Y, Z\}^{\otimes n}$ while A, B are arbitrary n -qubit operators. By the SWAP trick [105], we can write $\text{Tr}[APBP] = \text{Tr}[(AP \otimes BP)\mathbb{F}] = \text{Tr}[(A \otimes B)(P \otimes P)\mathbb{F}]$, where the flip operator $\mathbb{F} = \text{SWAP}^{\otimes n} = 2^{-n} \sum_{Q \in \{I, X, Y, Z\}^{\otimes n}} Q \otimes Q$ swaps the two n -qubit registers. From this, we find the decomposition $(P \otimes P)\mathbb{F} = 2^{-n} \sum_Q (-1)^{\delta_{P,Q}} Q \otimes Q$ and, therefore, $\text{Tr}[APBP] = 2^{-n} \sum_Q (-1)^{\delta_{P,Q}} \text{Tr}[AQ] \text{Tr}[BQ]$.
- [89] We slightly abuse notation and treat stabilizer groups \mathcal{S} as subsets of $\{I, X, Y, Z\}^{\otimes n} \subseteq \mathbb{C}^{2^n \times 2^n}$ when convenient.
- [90] P. Horodecki and A. Ekert, *Phys. Rev. Lett.* **89**, 127902 (2002).
- [91] R. Horodecki, P. Horodecki, M. Horodecki, and K. Horodecki, *Rev. Mod. Phys.* **81**, 865 (2009).
- [92] F. Huber, O. Gühne, and J. Siewert, *Phys. Rev. Lett.* **118**, 200502 (2017).
- [93] J. Conway and N. Sloane, *IEEE Trans. Inf. Th.* **36**, 1319 (1990).
- [94] W. K. Wootters, *Phys. Rev. Lett.* **80**, 2245 (1998).
- [95] P. Rungta, V. Bužek, C. M. Caves, M. Hillery, and G. J. Milburn, *Phys. Rev. A* **64**, 042315 (2001).
- [96] A. Wong and N. Christensen, *Phys. Rev. A* **63**, 044301 (2001).
- [97] W. Hall, *Phys. Rev. A* **72**, 022311 (2005).

- [98] M. A. Nielsen and I. L. Chuang, *Quantum Computation and Quantum Information* (Cambridge University Press, 2000).
- [99] N. Wyderka, F. Huber, and O. Gühne, *Phys. Rev. A* **97**, 060101 (2018).
- [100] F. Huber, C. Eltschka, J. Siewert, and O. Gühne, *J. Phys. A* **51**, 175301 (2018).
- [101] A. R. R. Carvalho, F. Mintert, and A. Buchleitner, *Phys. Rev. Lett.* **93**, 230501 (2004).
- [102] F. Mintert, M. Kuś, and A. Buchleitner, *Phys. Rev. Lett.* **95**, 260502 (2005).
- [103] F. Mintert and A. Buchleitner, *Phys. Rev. Lett.* **98**, 140505 (2007).
- [104] L. Aolita, A. Buchleitner, and F. Mintert, *Phys. Rev. A* **78**, 022308 (2008).
- [105] M. B. Hastings, I. González, A. B. Kallin, and R. G. Melko, *Phys. Rev. Lett.* **104**, 157201 (2010).
- [106] A. A. Mele, *Quantum* **8**, 1340 (2024).
- [107] Note that Eq. (48) can be visually understood in the calculus of tensor network rewirings [106, 186]. This viewpoint leads to multi-copy generalizations of Bell sampling to estimate higher-order Rényi entropies [187].
- [108] D. Miller, L. E. Fischer, I. O. Sokolov, P. K. Barkoutsos, and I. Tavernelli, “Hardware-Tailored Diagonalization Circuits,” (2022), arXiv:2203.03646.
- [109] C. Bertoni, J. Haferkamp, M. Hinsche, M. Ioannou, J. Eisert, and H. Pashayan, *Phys. Rev. Lett.* **133**, 020602 (2024).
- [110] L. E. Fischer, D. Miller, F. Tacchino, P. K. Barkoutsos, D. J. Egger, and I. Tavernelli, *Phys. Rev. Res.* **4**, 033027 (2022).
- [111] R. Stricker, M. Meth, L. Postler, C. Edmunds, C. Ferrie, R. Blatt, P. Schindler, T. Monz, R. Kueng, and M. Ringbauer, *PRX Quantum* **3**, 040310 (2022).
- [112] Our package is available under <https://github.com/Mc-Zen/qsalto> and via `pip install qsalto`.
- [113] Vandermonde’s identity, $\binom{n}{i} = \sum_l \binom{n-j}{i-l} \binom{j}{l}$, is a well-known result from combinatorics.
- [114] A. J. Scott, *Phys. Rev. A* **69**, 052330 (2004).
- [115] J. Beckey, N. Gigena, P. Coles, and M. Cerezo, *Phys. Rev. Lett.* **127**, 140501 (2021).
- [116] A. R. Cullen and P. Kok, *Phys. Rev. A* **106**, 042411 (2022).
- [117] J. L. Beckey, G. Pelegrí, S. Foulds, and N. J. Pearson, *Phys. Rev. A* **107**, 062425 (2023).
- [118] L. Schatzki, G. Liu, M. Cerezo, and E. Chitambar, *Phys. Rev. Res.* **6**, 023019 (2024).
- [119] This redresses the claim made in Prop. 2 of Ref. [117]. The chief problem is that the estimator for the n -tangle assumes the value 2^n in the rare event that none of the Bell measurements results in a triplet. In all other events, the same estimator assumes the value 0. Therefore, the denominator in the exponent of Höfdding’s inequality blows up exponentially, which renders measuring $\text{Tr}[\Psi\tilde{\Psi}]$ sample inefficient.
- [120] I. Pogorelov, T. Feldker, C. D. Marciniak, L. Postler, G. Jacob, *et al.*, *PRX Quantum* **2**, 020343 (2021).
- [121] D. C. McKay, C. J. Wood, S. Sheldon, J. M. Chow, and J. M. Gambetta, *Phys. Rev. A* **96**, 022330 (2017).
- [122] A. Sørensen and K. Mølmer, *Phys. Rev. Lett.* **82**, 1971 (1999).
- [123] D. Maslov, *New J. Phys.* **19**, 023035 (2017).
- [124] The experimentally extracted vector of damping factors $\lambda = (1, 0.957, 0.919, 0.885, 0.852, 0.819, 0.785)$ from Eq. (87) is in excellent agreement with local depolarizing noise [Eq. (15)] for an effective noise rate per qubit of $p = 0.02$.
- [125] In this work, we care about measuring QWEs of noisy states. Hence, our error mitigation strategy used in the main text only aims to remove readout noise from the Bell measurements but not from state preparation. For other applications, where it is important to also mitigate noise that arises during state preparation, one could instead employ the following error mitigation strategy: heuristically assume that all noise is captured by the local depolarizing noise channel, for which we know the effect on SLDs from Eq. (15). Then, determine the effective noise parameter $p \in (0, 1)$ for which $\sum_{i=0}^n a_i^{\text{miti}}[\rho_{\text{exp}}] = \text{Tr}[\rho_{\text{targ}}^2]$ under the condition $(1-p)^{2i} a_i^{\text{miti}}[\rho_{\text{exp}}] = a_i^{\text{raw}}[\rho_{\text{exp}}]$, where ρ_{targ} and ρ_{exp} denote the target state and its experimental realization, respectively.
- [126] For clarity, we point out the two-qubit gate count N_j in our circuit for preparing Ψ_j : $N_1 = 0$, $N_2 = 3$, $N_3 = 5$, $N_4 = 5$, $N_5 = 6$, $N_6 = 7$. Except for Ψ_6 (App. E), preparation circuits are the obvious ones. Two-qubit Mølmer-Sørensen gates were applied sequentially.
- [127] M. Hein, J. Eisert, and H. J. Briegel, *Phys. Rev. A* **69**, 062311 (2004).
- [128] A. Cabello, L. E. Danielsen, A. J. López-Tarrida, and J. R. Portillo, *Phys. Rev. A* **83**, 042314 (2011).
- [129] For example, $\rho = \frac{1}{2} |D_1^n\rangle\langle D_1^n| + \frac{1}{2} |D_{n-1}^n\rangle\langle D_{n-1}^n|$ in the notation of Eq. (111) is a state that—despite being GME—has a vanishing full-body sector length $a_n[\rho]$, assuming n is odd [188].
- [130] E. Kubischta and I. Teixeira, *Phys. Rev. Lett.* **131**, 240601 (2023).
- [131] For codes where X_L is not transversal, it is sufficient to sample from $|0, 0\rangle_L$, $|0, 1\rangle_L$, and $|1, 1\rangle_L$ because Bell states are symmetric under particle exchange (up to a global phase that is irrelevant here).
- [132] H. Bombin and M. A. Martin-Delgado, *Phys. Rev. Lett.* **97**, 180501 (2006).
- [133] H. Bombin and M. A. Martin-Delgado, *Phys. Rev. A* **73**, 062303 (2006).
- [134] C. Ryan-Anderson, N. C. Brown, M. S. Allman, B. Arkin, G. Asa-Attuah, *et al.*, “Implementing fault-tolerant entangling gates on the five-qubit code and the color code,” (2022), arXiv:2208.01863.
- [135] F. Butt, S. Heußen, M. Rispler, and M. Müller, *PRX Quantum* **5**, 020345 (2024).
- [136] I. Pogorelov, F. Butt, L. Postler, C. D. Marciniak, P. Schindler, M. Müller, and T. Monz, “Experimental fault-tolerant code switching,” (2024), arXiv:2403.13732.
- [137] M. P. da Silva, C. Ryan-Anderson, J. M. Bello-Rivas, A. Chernoguzov, J. M. Dreiling, *et al.*, “Demonstration of logical qubits and repeated error correction with better-than-physical error rates,” (2024), arXiv:2404.02280.
- [138] K. Mayer, C. Ryan-Anderson, N. Brown, E. Durso-Sabina, C. H. Baldwin, *et al.*, “Benchmarking logical three-qubit quantum Fourier transform encoded in the Steane code on a trapped-ion quantum computer,” (2024), arXiv:2404.08616.
- [139] C. Ryan-Anderson, N. C. Brown, C. H. Baldwin, J. M. Dreiling, C. Foltz, *et al.*, “High-fidelity and fault-tolerant teleportation of a logical qubit using transversal gates and lattice surgery on a trapped-ion quantum computer,” (2024), arXiv:2404.16728.
- [140] M. Valentini, M. W. van Mourik, F. Butt, J. Wahl, M. Dietl, *et al.*, “Demonstration of two-dimensional connectivity for a scalable error-corrected ion-trap quantum processor architecture,” (2024), arXiv:2406.02406.
- [141] H. Zhou, C. Zhao, M. Cain, D. Bluvstein, C. Duckering, H.-Y. Hu, S.-T. Wang, A. Kubica, and M. D. Lukin, “Algorithmic fault tolerance for fast quantum computing,” (2024), arXiv:2406.17653.

- [142] L. Postler, S. Heußen, I. Pogorelov, M. Rispler, T. Feldker, M. Meth, C. D. Marciniak, R. Stricker, M. Ringbauer, R. Blatt, P. Schindler, M. Müller, and T. Monz, *Nature* **605**, 675 (2022).
- [143] S. Heußen, L. Postler, M. Rispler, I. Pogorelov, C. D. Marciniak, T. Monz, P. Schindler, and M. Müller, *Phys. Rev. A* **107**, 042422 (2023).
- [144] L. Postler, F. Butt, I. Pogorelov, C. D. Marciniak, S. Heußen, R. Blatt, P. Schindler, M. Rispler, M. Müller, and T. Monz, *PRX Quantum* **5**, 030326 (2024).
- [145] R. Zen, J. Olle, L. Colmenarez, M. Puviani, M. Müller, and F. Marquardt, “Quantum circuit discovery for fault-tolerant logical state preparation with reinforcement learning,” (2024), [arXiv:2402.17761](https://arxiv.org/abs/2402.17761).
- [146] T. Peham, L. Schmid, L. Berent, M. Müller, and R. Wille, “Automated synthesis of fault-tolerant state preparation circuits for quantum error correction codes,” (2024), [arXiv:2408.11894](https://arxiv.org/abs/2408.11894).
- [147] The respective ideal values are $\tilde{a}_7[\rho_{\text{QECC}}^{\text{ideal}}] = 0.176(1)$ and $C[\rho_{\text{QECC}}^{\text{ideal}}] \geq 0.33(1)$.
- [148] C. Skornia, J. v. Zanthier, G. S. Agarwal, E. Werner, and H. Walther, *Phys. Rev. A* **64**, 063801 (2001).
- [149] A. S. Sørensen and K. Mølmer, *Phys. Rev. Lett.* **90**, 127903 (2003).
- [150] C. Thiel, J. von Zanthier, T. Bastin, E. Solano, and G. S. Agarwal, *Phys. Rev. Lett.* **99**, 193602 (2007).
- [151] W. Chen, J. Hu, Y. Duan, B. Braverman, H. Zhang, and V. Vuletić, *Phys. Rev. Lett.* **115**, 250502 (2015).
- [152] E. J. Davis, Z. Wang, A. H. Safavi-Naeini, and M. H. Schleier-Smith, *Phys. Rev. Lett.* **121**, 123602 (2018).
- [153] J. Ramette, J. Sinclair, and V. Vuletić, (2024), [arXiv:2401.1140](https://arxiv.org/abs/2401.1140).
- [154] S. Welte, B. Hacker, S. Daiss, S. Ritter, and G. Rempe, *Phys. Rev. Lett.* **118**, 210503 (2017).
- [155] S. Welte, B. Hacker, S. Daiss, S. Ritter, and G. Rempe, *Phys. Rev. X* **8**, 011018 (2018).
- [156] T. Đorđević, P. Samutpraphoot, P. L. Ocola, H. Bernien, B. Grinkemeyer, I. Dimitrova, V. Vuletić, and M. D. Lukin, *Science* **373**, 1511 (2021).
- [157] S. Richter, S. Wolf, J. von Zanthier, and F. Schmidt-Kaler, *Phys. Rev. Res.* **5**, 013163 (2023).
- [158] E. Magesan, J. M. Gambetta, and J. Emerson, *Phys. Rev. A* **85**, 042311 (2012).
- [159] For example, for $m = 1$ and abbreviating $\omega = \rho \otimes \rho$, we find $U\omega U^\dagger - \omega = U\omega U^\dagger(\mathbb{1} - U) - (\mathbb{1} - U)\omega$, which implies $\|U\omega U^\dagger - \omega\|_1 \leq \|U\omega U^\dagger(\mathbb{1} - U)\|_1 + \|(\mathbb{1} - U)\omega\|_1$ by the triangle inequality. Next, applying Hölder’s inequality yields $\|U\omega U^\dagger(\mathbb{1} - U)\|_1 \leq \|U\|_\infty \|\omega\|_1 \|U^\dagger\|_\infty \|(\mathbb{1} - U)\|_\infty$ and $\|(\mathbb{1} - U)\omega\|_1 \leq \|\mathbb{1} - U\|_\infty \|\omega\|_1$. Since U is a unitary and ω is a state, we have $\|U\|_\infty = \|U^\dagger\|_\infty = \|\omega\|_1 = 1$. Finally, $\|U\omega U^\dagger - \omega\|_1 \leq 2 \min_\phi \|U - \mathbb{1}e^{i\phi}\|_\infty$ follows from minimizing the norm over the global phase, which completes the proof of Eq. (102) for $m = 1$. The general case of $m \geq 1$ follows similarly using telescope sums.
- [160] See <https://mc-zen.github.io/qsalto/?n=500> for an illustration of this fact in an interactive online version of Fig. 1 for $n = 500$ qubits.
- [161] A. W. Harrow and S. Mehraban, *Commun. Math. Phys.* **401**, 1531 (2023).
- [162] For the $e = 20$ curve, however, we observe an initial increase of N with n . This is due to the competing effects, e.g., for $n = 21$ ($n = 40$), the state is local-unitary equivalent to $e = 1$ ($e = n/2$). These two extreme cases have opposite behaviors as described in the main text.
- [163] M. Hinsche, M. Ioannou, S. Jerbi, L. Leone, J. Eisert, and J. Carrasco, “Efficient distributed inner product estimation via pauli sampling,” (2024), [arXiv:2405.06544](https://arxiv.org/abs/2405.06544).
- [164] M. Bergmann and O. Gühne, *J. Phys. A* **46**, 385304 (2013).
- [165] H. Häffner, W. Hänsel, C. F. Roos, J. Benhelm, D. Chekalkar, *et al.*, *Nature* **438**, 643 (2005).
- [166] A. Peres, *Phys. Rev. Lett.* **77**, 1413 (1996).
- [167] M. Horodecki, P. Horodecki, and R. Horodecki, *Phys. Lett. A* **223**, 1 (1996).
- [168] Y. Zhou, P. Zeng, and Z. Liu, *Phys. Rev. Lett.* **125**, 200502 (2020).
- [169] A. Elben, R. Kueng, H.-Y. R. Huang, R. van Bijnen, C. Kokail, M. Dalmonte, P. Calabrese, B. Kraus, J. Preskill, P. Zoller, and B. Vermersch, *Phys. Rev. Lett.* **125**, 200501 (2020).
- [170] Z. Liu, Y. Tang, H. Dai, P. Liu, S. Chen, and X. Ma, *Phys. Rev. Lett.* **129**, 260501 (2022).
- [171] A. Rico and F. Huber, *Phys. Rev. Lett.* **132**, 070202 (2024).
- [172] E. Rains, *IEEE Trans. Inf. Th.* **46**, 54 (2000).
- [173] F. Huber, *J. Math. Phys.* **62**, 022203 (2021).
- [174] G. A. Munné, A. Nemeč, and F. Huber, “SDP bounds on quantum codes,” (2024), [arXiv:2408.10323](https://arxiv.org/abs/2408.10323) [quant-ph].
- [175] A. Kukliansky and B. Lackey, “Quantum circuit tensors and enumerators with applications to quantum fault tolerance,” (2024), [arXiv:2405.19643](https://arxiv.org/abs/2405.19643).
- [176] P. Rall, “Signed quantum weight enumerators characterize qubit magic state distillation,” (2017), [arXiv:1702.06990](https://arxiv.org/abs/1702.06990).
- [177] C. K. Hong, Z. Y. Ou, and L. Mandel, *Phys. Rev. Lett.* **59**, 2044 (1987).
- [178] C. Moura Alves and D. Jaksch, *Phys. Rev. Lett.* **93**, 110501 (2004).
- [179] A. J. Daley, H. Pichler, J. Schachenmayer, and P. Zoller, *Phys. Rev. Lett.* **109**, 020505 (2012).
- [180] J. C. Garcia-Escartin and P. Chamorro-Posada, *Phys. Rev. A* **87**, 052330 (2013).
- [181] F. Shi, K. Guo, X. Zhang, and Q. Zhao, “Exploring quantum weight enumerators from the n -qubit parallelized swap test,” (2024), [arXiv:2406.18280](https://arxiv.org/abs/2406.18280).
- [182] M. C. Tran, B. Dakić, W. Laskowski, and T. Paterek, *Phys. Rev. A* **94**, 042302 (2016).
- [183] R. F. Werner, *Phys. Rev. A* **40**, 4277 (1989).
- [184] K. Levi *et al.*, (2024), work in preparation.
- [185] S. Bravyi, D. Lee, Z. Li, and B. Yoshida, “How much entanglement is needed for quantum error correction?” (2024), [arXiv:2405.01332](https://arxiv.org/abs/2405.01332) [quant-ph].
- [186] J. C. Bridgeman and C. T. Chubb, *J. Phys. A* **50**, 223001 (2017).
- [187] Y. Subaşı, L. Cincio, and P. J. Coles, *J. Phys. A* **52**, 044001 (2019).
- [188] D. Kaszlikowski, A. Sen(De), U. Sen, V. Vedral, and A. Winter, *Phys. Rev. Lett.* **101**, 070502 (2008).